nature portfolio

Peer Review File

Exceptional eruptive CO2 emissions from intra-plate alkaline magmatism in the Canary volcanic archipelago

Web links to the author's journal account have been redacted from the decision letters as indicated to maintain confidentiality

13th Jul 23

Dear Professor Burton,

Please allow me to apologise for the delay in sending a decision on your manuscript titled "Exceptional CO2 emissions from erupting alkaline mafic magma in the Canary volcanic archipelago". It has now been seen by 2 reviewers, and we include their comments at the end of this message. They find your work of interest, but some important points are raised. We are interested in the possibility of publishing your study in Communications Earth & Environment, but would like to consider your responses to these concerns and assess a revised manuscript before we make a final decision on publication.

We therefore invite you to revise and resubmit your manuscript, along with a point-by-point response that takes into account the points raised. Please highlight all changes in the manuscript text file.

In particular, please ensure that the revised manuscript meets the following editorial thresholds:

* Present robust estimations of the magmatic CO2 content of the 2021 Tajogaite eruption which take into account the contribution of CO2 exsolved from un-erupted magma and amend your conclusions where necessary.

* With respect to the extrapolation of your data from one eruption to the entirety of Canary Island volcanism, please clearly discuss and justify all assumptions and speculations involved and soften/caveat these claims accordingly.

We are committed to providing a fair and constructive peer-review process. Please don't hesitate to contact us if you wish to discuss the revision in more detail.

Please use the following link to submit your revised manuscript, point-by-point response to the referees' comments (which should be in a separate document to any cover letter) and the completed checklist:
[link redacted]
** This url links to your confidential home page and associated information about manuscripts you may have submitted or be reviewing for us. If you wish to forward this email to co-authors, please delete the link to your homepage first **

We hope to receive your revised paper within six weeks; please let us know if you aren't able to submit it within this time so that we can discuss how best to proceed. If we don't hear from you, and the revision process takes significantly longer, we may close your file. In this event, we will still be happy to reconsider your paper at a later date, as long as nothing similar has been accepted for publication at Communications Earth & Environment or published elsewhere in the meantime.

Please do not hesitate to contact us if you have any questions or would like to discuss these revisions further. We look forward to seeing the revised manuscript and thank you for the opportunity to review your work.

Best regards,

Joe Aslin

Senior Editor,
Communications Earth & Environment
https://www.nature.com/commsenv/
Twitter: @CommsEarth

EDITORIAL POLICIES AND FORMATTING

We ask that you ensure your manuscript complies with our editorial policies. Please ensure that the following formatting requirements are met, and any checklist relevant to your research is completed and uploaded as a Related Manuscript file type with the revised article.

Editorial Policy: Policy requirements (Download the link to your computer as a PDF.)

Furthermore, please align your manuscript with our format requirements, which are summarized on the following checklist:
Communications Earth & Environment formatting checklist

and also in our style and formatting guide Communications Earth & Environment formatting guide .

*** DATA: Communications Earth & Environment endorses the principles of the Enabling FAIR data project (http://www.copdess.org/enabling-fair-data-project/). We ask authors to make the data that support their conclusions available in permanent, publically accessible data repositories. (Please contact the editor if you are unable to make your data available).

All Communications Earth & Environment manuscripts must include a section titled "Data Availability" at the end of the Methods section or main text (if no Methods). More information on this policy, is available at http://www.nature.com/authors/policies/data/data-availability-statements-data-citations.pdf.

In particular, the Data availability statement should include:
- Unique identifiers (such as DOIs and hyperlinks for datasets in public repositories)
- Accession codes where appropriate
- If applicable, a statement regarding data available with restrictions
- If a dataset has a Digital Object Identifier (DOI) as its unique identifier, we strongly encourage including this in the Reference list and citing the dataset in the Data Availability Statement.

DATA SOURCES: All new data associated with the paper should be placed in a persistent repository where they can be freely and enduringly accessed. We recommend submitting the data to discipline-

specific, community-recognized repositories, where possible and a list of recommended repositories is provided at http://www.nature.com/sdata/policies/repositories.

If a community resource is unavailable, data can be submitted to generalist repositories such as figshare or Dryad Digital Repository. Please provide a unique identifier for the data (for example a DOI or a permanent URL) in the data availability statement, if possible. If the repository does not provide identifiers, we encourage authors to supply the search terms that will return the data. For data that have been obtained from publically available sources, please provide a URL and the specific data product name in the data availability statement. Data with a DOI should be further cited in the methods reference section.

Please refer to our data policies at http://www.nature.com/authors/policies/availability.html.

REVIEWER COMMENTS:

Reviewer #1 (Remarks to the Author):

Please see attached file

Reviewer #2 (Remarks to the Author):

The article presented analyzes the data obtained on the emissions of various gases (H2O, CO2, SO2, H2, SH2, etc.) in the eruption of the Tajogaite volcano on La Palma in 2021, differentiating the gaseous emissions from the various emission points that appeared during the eruption, distinguishing the emanations associated with the effusive vents (EV), from spattering vents (SV) and fountaining vents (FV), as well as the emanations associated with the interruption of the eruption of September 27, 2021 (PV). In this sense, the authors found an important difference in the CO2/SO2 ratio of these emissions, observing a high relationship in the emissions associated with explosive eruptive moments or vents (fountaining vents, FV) compared to low values for the emissions associated with effusive events (effusive vent, EV), or spattering vents (SV), as well as the emissions associated with the interruption of the eruption on September 27, 2021 (PV).

The authors relate these differences to the existence of a single feeding dyke in the eruption that is subdivided into several branches at a depth of about 400 meters. The main vertical branch would channel the intense degassing of CO2, associated with the most explosive activity (FV), in the highest vents, while the lateral branches would channel the flow of SO2 and lava to the lower-altitude vents (EV and SV vents.

On the other hand, they conclude that the initial CO2 content of the magma that produced the eruption would be around 4.5 Wt%. The authors explain these high values due to the fact that the magma was formed in a metasomatized mantle by recycling oceanic crust of certain chemical

elements under a low degree of partial melting, an aspect that had already been verified in the El Hierro eruption of 2011-2012. In this sense, and by calculating the volume of magma emitted in the formation of La Palma from its seamount stage (estimated a duration of 12 million years for this entire process, somewhat excessive, taking into account that the age of the volcanic rocks that appear on the Island (the submarine trachytic lobe-hyaloclastitic complex) of around 3.1 Ma, Casillas et al., 2019) conclude that the CO2 emitted in all these eruptions would be equivalent to 20% of that emitted in the formation of the typical Large Igneous Provinces, eruptions that are involved in periods of major environmental and climatic change in Earth's history.

These are very new data and results that help to understand the different eruptive dynamics of the different eruption vents throughout the eruption, explaining the more or less intense explosive activity of each eruptive vent and at each moment.

For all these reasons, I consider that the article deserves to be published with slight modifications that I refer to in an attached file.

Review of the manuscript

"Exceptional CO_2 emissions from erupting alkaline mafic magma in the Canary volcanic archipelago"

by Burton et al.

General comments

The manuscript addresses a fundamental problem related to the origin and evolution of oceanic intraplate magmas, namely their original volatile contents and degassing processes. It further features a re-assessment of the degassing budgets of oceanic intraplate systems. The manuscript is well written, and presents a detailed account for the preferred model of progressive magma degassing, which is further used as a basis for syn-eruptive volatile budget estimates. However, two important factors have not been properly considered:

A) In the calculations of primary volatile contents of the magmas, the assumption used seems to be that only the erupted magmas are responsible for the CO_2 mass emitted into the atmosphere. Because magmas that do not erupt also contribute to the degassing, the resulting estimates of original volatile contents are biased towards too high values.

B) Concerning the cumulative degassing budgets, only the estimated edifice volume of the island in question has been considered, and not intrusive rocks emplaced into the crust beneath the main edifice, which certainly also degas during crystallisation.

In spite of these comments, the approach used in the paper is excellent, and it should be reconsidered for publication following a revision.

Further comments

The *CO_2 budgets* presented are biassed by assuming that the total amount of volatiles released were dissolved in the erupted magmas only, which is most probably wrong. You nicely demonstrate that degassing must have commenced at upper mantle levels. As only a fraction of the magmas entering the crust actually reach the surface, but still degas to variable extents, the calculated volatile budgets for the primitive magmas are most likely overestimated. I know this is hard to quantify, but still has to be considered in such a high-profile paper.

As you mention, magmatic CO_2-dominated fluid inclusions in the Tajogaite eruption (Dayton et al. 2023) gives *CO_2 oversaturation pressures* at about 1 GPa or less, overlapping with the results for very similar Gran Canaria basanites (Hansteen et al., 1998; CMP). Taken at face value, this would correspond to CO_2 contents considerably less than those suggested in the present manuscript for the magmas involved. How does this fit with your results?

Degassing of intrusive rocks must contribute to the CO_2 budgets of ocean island volcanoes. Total degassing budgets presented in the manuscript consider only the

estimated edifice volume, and thus excludes intrusive rocks in the middle to lower crust. The CO_2 exsolved from such intrusions may be released to the hydrosphere/ atmosphere by diffuse degassing. Please comment on this problem.

Best wishes

Thor Hansteen

Exceptional CO_2 emissions from erupting alkaline mafic magma in the Canary volcanic archipelago

Mike Burton[1], Alessandro Aiuppa[2], Patrick Allard[3], María Asensio-Ramos[4], Ana Pardo Cofrades[1], Alessandro La Spina[5], Emma J. Nicholson[6], Vittorio Zanon[7], José Barrancos[4,8], Marcello Bitetto[2], Margaret Hartley[1], Jorge Romero Moyano[1], Emma Waters[1], Alex Stewart[1], Pedro A. Hernández[4,8], João Pedro Lages[2,6], Eleazar Padrón[4,8], Kieran Wood[9], Benjamin Esse[1], Catherine Hayer[1], Klaudia Cyrzan[7], Estelle F. Rose-Koga[10], Federica Schiavi[11], Luca D'Auria[4,8], and Nemesio M. Pérez[4,8]

[1]COMET, Department of Earth and Environmental Science, University of Manchester, Manchester, United Kingdom (mike.burton@manchester.ac.uk)
[2]Università degli Studi di Palermo, Departmento di Scienze della Terra e del mare, Palermo, Italy
[3] Institut de Physique du Globe de Paris, Paris, France
[4]Instituto Volcanológico de Canarias (INVOLCAN), 38320 San Cristóbal de La Laguna, Tenerife, Canary Islands, Spain
[5] Istituto Nazionale di Geofisica e Vulcanologia, Sezione di Catania, Italy
[6]University College London, Earth Sciences, London, United Kingdom
[7]Instituto de Investigação em Vulcanologia e Avaliação de Riscos (IVAR), universidade dos Açores, Ponta Delgada,Portugal
[8]Instituto Tecnológico y de Energías Renovables (ITER), 38600 Granadilla de Abona, Tenerife, Canary Islands, Spain
[9]University of Manchester, Department of Mechanical Aerospace and Civil Engineering, Manchester, United Kingdom
[10]Institut des Sciences de la Terre d'Orléans (ISTO), CNRS, Orléans, France
[11]Laboratoire Magma et Volcans (LMV), Université Clermont-Auvergne, CNRS, IRD, OPGC, Clermont Ferrand, France

Alkaline mafic magmas forming intra-plate oceanic islands are believed to be strongly enriched in CO_2 due to low-degree partial melting of enriched mantle sources. However, until now, such CO_2 enhancement has not been verified by measuring CO_2 degassing during a subaerial eruption. Here, we provide evidence of highly CO_2-rich gas emissions during the 86-days long 2021 Tajogaite eruption of the Cumbre Vieja volcanic system (La Palma Island). Our results reveal sustained high plume CO_2/SO_2 ratios, which, when combined with SO_2 fluxes, melt inclusion volatile contents and magma production rates at explosive and effusive vents, implies an initial magmatic CO_2 content of 4.5 ± 1.5 wt%. The amount of CO_2 released during the 2021 eruptive activity was 28 ± 14 Mt CO_2. Extrapolating to the volume of alkaline mafic magmas forming La Palma alone (estimated as 4000 km^3 erupted over 10 Ma), we infer a maximum CO_2 emission into the ocean and atmosphere of 10^{16} moles of CO_2, equivalent to 20% of the eruptive CO_2 emissions from a large igneous province eruption, suggesting that the formation of the Canary volcanic archipelago produced a CO_2 emission of similar magnitude as a large igneous province.

Volatile exsolution and expansion during magma ascent are the primary drivers of volcanic eruptions[1] and volcanic gas emissions have had a profound impact on volatile cycles[2] and climate[3] throughout Earth's history. Quantifying the original volatile content of magmas is

therefore a key objective in volcanological research. Among the main volatile species carried by magmas (H_2O, CO_2, SO_2, HCl, HF), CO_2 is the least soluble and therefore the first to exsolve, even at pressures consistent with the mid to lower crust. Volatile solubility behaviour is well-established for a wide range of magma compositions from experiments under various pressure and temperature conditions[4]; thermodynamics[5] and microanalysis of dissolved volatiles in melt (glassy) droplets and fluid inclusions entrapped in crystals that form during magma storage and ascent[6,7]. The low solubility of CO_2 drives exsolution prior to melt inclusion formation which, in addition to post-entrapment CO_2-loss to bubbles and bubble decrepitation upon ascent[8], means that inclusion-measured CO_2 contents are lower limits for the initial CO_2 content[6]. CO_2-rich fluid inclusions trapped at high pressures[9] evidence that a co-existing fluid phase may be present even at mantle depths if CO_2 abundances are high enough[10,11].

Trace element ratios such as CO_2/Nb and CO_2/Ba can provide an alternative approach to constrain the potential range of initial magmatic CO_2 content[12,13]. Uncertainties arise, however, from the large variability in these ratios due to mantle heterogeneity and melt mixing[14]. Syn-eruptive measurements of CO_2 emissions, while challenging to acquire, can provide robust information on pre-eruptive contents of CO_2 and other volatiles, when combined with measurements of magma eruption rate, SO_2 fluxes and the initial magma sulfur (S) content[11,12,15]. Eruptive gas compositions are measurable either remotely, using open-path Fourier Transform infra-red (OP-FTIR) spectroscopy with molten lava as the radiation source[16,17], or in-situ, using Multi-GAS analysis of dilute gas plumes[18]; see Methods. Scaling the X/SO_2 ratio, where X is the volatile of interest, to the SO_2 flux measured from the ground and space[19-21] provides the mass flux of CO_2 and other components. Normalising these mass fluxes to the mass eruption rate (MER) of magma then allows initial volatile contents in the magma to be calculated[22].

One of the most significant recent discoveries in volcanology is that magmatic CO_2 contents may be much higher than initially thought[23,24]. This observation has important implications for the contribution of volcanism to the global geological CO_2 budget[25,26] and to global climate and mass-extinction events during large igneous province eruptions[27]. In particular, alkaline mafic magmas have been highlighted as a main source of CO_2-rich volcanism[28-30], with those erupted at intra-plate oceanic islands believed to be especially enriched in CO_2 due to low-degree partial melting of enriched mantle sources[11]. In the Canary volcanic archipelago, eastern Atlantic ocean, a high CO_2 content between 2.5 and 5 wt% was estimated in basanites from El Hierro volcano[30]. However, direct measurements of CO_2 emissions during eruption of such magmas still remain sparse, and hitherto non-existent for the Canary Islands volcanic archipelago.

The 2021 Tajogaite eruption of the Cumbre Vieja volcanic system, on La Palma island, provided a remarkable opportunity to quantify volatile emissions and magma volatile contents for alkaline mafic magmatism in the Canary Islands archipelago. The Canary Islands constitute the subaerial portions of a group of voluminous intraplate volcanoes that predominantly erupt alkaline magmas derived from a heterogeneous mantle source[31]. The Cumbre Vieja volcanic system is currently the most active in the archipelago; however, no gas emission measurements were conducted during its last eruption in 1971.

The 85-days long Tajogaite eruption began on 19th September 2021 along a NNW-ESE fracture system ~930 m above sea level, just above urbanized areas (**Figure 1**). Voluminous lava flows, and dense lapilli and ash fallout from sustained lava fountaining activity, forced the evacuation of ~7000 people and caused extensive destruction until the end of the eruption on 13th December 2021[32]. The initial eruptive fissure evolved rapidly into a single main cone (Tajogaite) that hosted multiple linearly-aligned and closely-spaced vents[32-34]. Powerful lava fountaining and explosive activity were produced from central upper vents (referred to here as Fountaining Vent(s), FV), while spattering and lava flow effusion occurred at flank vents (hereafter referred to as Spattering Vent, SV, and Effusive Vent(s), EV; **Figure 1**). Initially erupted basanite ascending from 10-16 km depth were progressively replaced by a less evolved basanite/alkali-basalt ascending from 27-31 km[9,35,36]. Continuous syn-eruptive seismicity located in two event clusters at ~10-16 km and ~22-27 km [37], as well as fluid inclusions in olivines[9,36], marked the respective storage depths of these magmas.

The 2021 eruption site was relatively accessible, with established road / track infrastructure close to the vents. This access enabled repeated (~daily) quantification of the chemical composition and mass flux of magmatic gases discharged from both explosive and effusive vents. These measurements were acquired using a suite of ground-based, aerial and orbital (satellite) instruments. Specifically, we quantified emitted gas compositions using Multi-GAS, deployed as ground-based (mobile and fixed stations) and drone-mounted systems, and OP-FTIR spectrometers (see Methods). We derived SO_2 fluxes using data from the satellite-based TROPOMI sensor (see Methods). In this study, we quantify the magmatic CO_2 flux produced during the 2021 Tajogaite eruption and combine with volcanological and petrological data to determine the original CO_2 content of the parental basanitic magma.

A key observation from our field measurements is the sharp, systematic contrast in CO_2/SO_2 ratios measured in gas emissions from the explosive upper vents (FV) and the spattering/effusive (SV/EV) flank vents (**Figure 1**). This pattern is well-illustrated by Multi-GAS data obtained between 27 September and 3 October 2021, with CO_2/SO_2 molar ratios varying from 52-25 (FV) to 3-13 (SV) and down to 0.3-0.04 (EV), as well as by OP-FTIR data collected from 3 October until the end of the eruption (**Extended Data Table 1** and **Figure 1**). Such a spectacular compositional contrast, at vents only 500 m apart, demonstrates that poorly-soluble CO_2 was

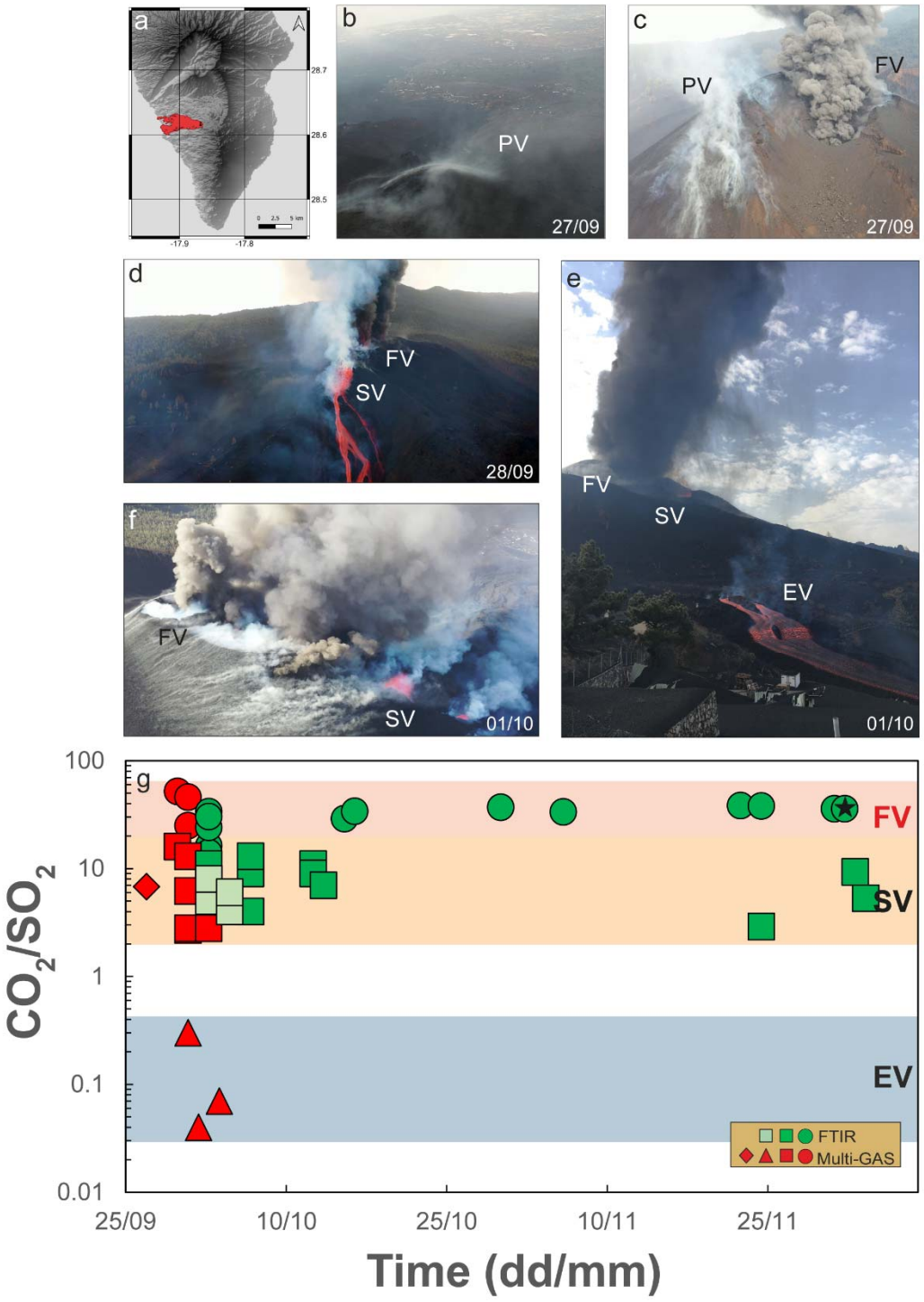

FIGURE 1: The 2021 Tajogaite eruption (Cumbre Vieja, La Palma) and chronology of volcanic gas measurements. (a) The 2021 lava flow field in south-western La Palma. Aerial images of the near-vent eruptive region, showing multiple distinct emission sources, eruptive styles, and degassing regimes (PV, passive vent; FV, fountaining vents; SV; spattering vent; EV, effusive vent). (b, c) Passive emissions during an eruptive pause and immediately following main vent reactivation on 27 September 2021. (d, e) Lateral progression in eruptive style from intense ash-producing lava fountaining activity at the upper vents (FV) through to spattering activity at the lower vent (SV), feeding lava flows; (f) Concurrent lava fountaining, spattering and non-explosive lava effusion on 1 October 2021. The EV opened at the base of the northern flank of the cone and fed lava extrusion for two days. (g) Temporal evolution of CO_2/SO_2 ratios in the gas plumes released by the different vents, as measured with Multi-GAS and OP-FTIR spectroscopy. Symbols indicate vent source (diamond = eruptive pause; circle = FV; square = SV (four especially water-rich compositions – see Figure 2 - are identified with light green tone); and triangle = EV). The star highlights the highest quality FV measurement.

predominantly outgassed through the central upper vents and, hence, already highly depleted prior to secondary degassing of the magma discharged effusively through the flank vents. A similar CO_2-fractionation pattern was previously documented on Mt. Etna between eruptive[16] and passive degassing[38].

Our second key observation is that explosive gas emissions from the central upper vents (FV) displayed very high CO_2/SO_2 ratios during the whole eruption (**Figure 1**). Our best OP-FTIR observations on December 2, 2021 (starred in **Figures 1** and **2**) constrain the FV gas to contain 37 mol% H_2O, 61 mol% CO_2 and 1.7 mol% SO_2, with a CO_2/SO_2 molar ratio of 36 (24 by mass) (**Extended Data Table 1**). A similarly high CO_2/SO_2 ratio persisted at the FV throughout the entire eruption (**Figure 1**), with a mean value of 33 ± 9.7 (or 23 ± 6.7 by mass). This makes the syn-eruptive gas from the explosive vents of Tajogaite one of the most CO_2-rich ever measured at an active volcano to date[25,26,39]. By contrast, the mean CO_2/SO_2 ratio at the lower flank vents exhibiting lava spattering (SV) was 7.3 ± 4.0 (or 5.0 ± 2.7 by mass) throughout the eruption.

To reconstruct the magma degassing path(s) (**Figure 2**), we measured the dissolved H_2O, CO_2 and S contents of glassy basanitic melt inclusions entrapped in erupted olivine crystals **(Extended Data Table 2; see Methods)**. The sulphur content of these inclusions displays a narrow range, averaging 3290 ± 390 ppm (one standard deviation), and shows no systematic variation during the eruption (**Extended Data Figure 1** and **Extended Data Figure 2**); it thus represents the initial sulphur abundance in the parental basanite. The same inclusions also contain 1.30-2.21 wt.% H_2O and 0.22-0.50 wt.% CO_2. According to experimental data for H_2O and CO_2 solubility in Canary basanites[40], such concentrations correspond to melt inclusion entrapment pressures of ~290 to ~350 MPa, or ~10-12 km depth given the local crustal density structure(D'Auria et al. 2022). This depth range fits with the near-Moho seismogenetic volume (at 10-16 km) active during the Cumbre Vieja eruption[9,37], which we interpret as an intermediate magma ponding zone fed by the more deeply sourced (15-27 km) basanites[9,36]. The presence of pure CO_2 fluid inclusions in olivine and other crystals within the erupted magma[9,36] indicate that the mantle-derived basanites already co-existed with a CO_2-rich gas phase prior to reaching this intermediate storage zone. It is thus very likely that the maximum dissolved CO_2 content in melt inclusions (0.50 wt.%) under-estimates the parental melt CO_2. Using a C-H-O-S solubility model[5], we therefore computed the evolving

fluid composition (**Figure 2**) during decompression of magma containing initial CO_2 contents of 0.5 to 5 wt.%, in both closed- and open-system conditions, under temperature-redox conditions typical for La Palma basanites (see Methods; **Extended Data Table 3**).

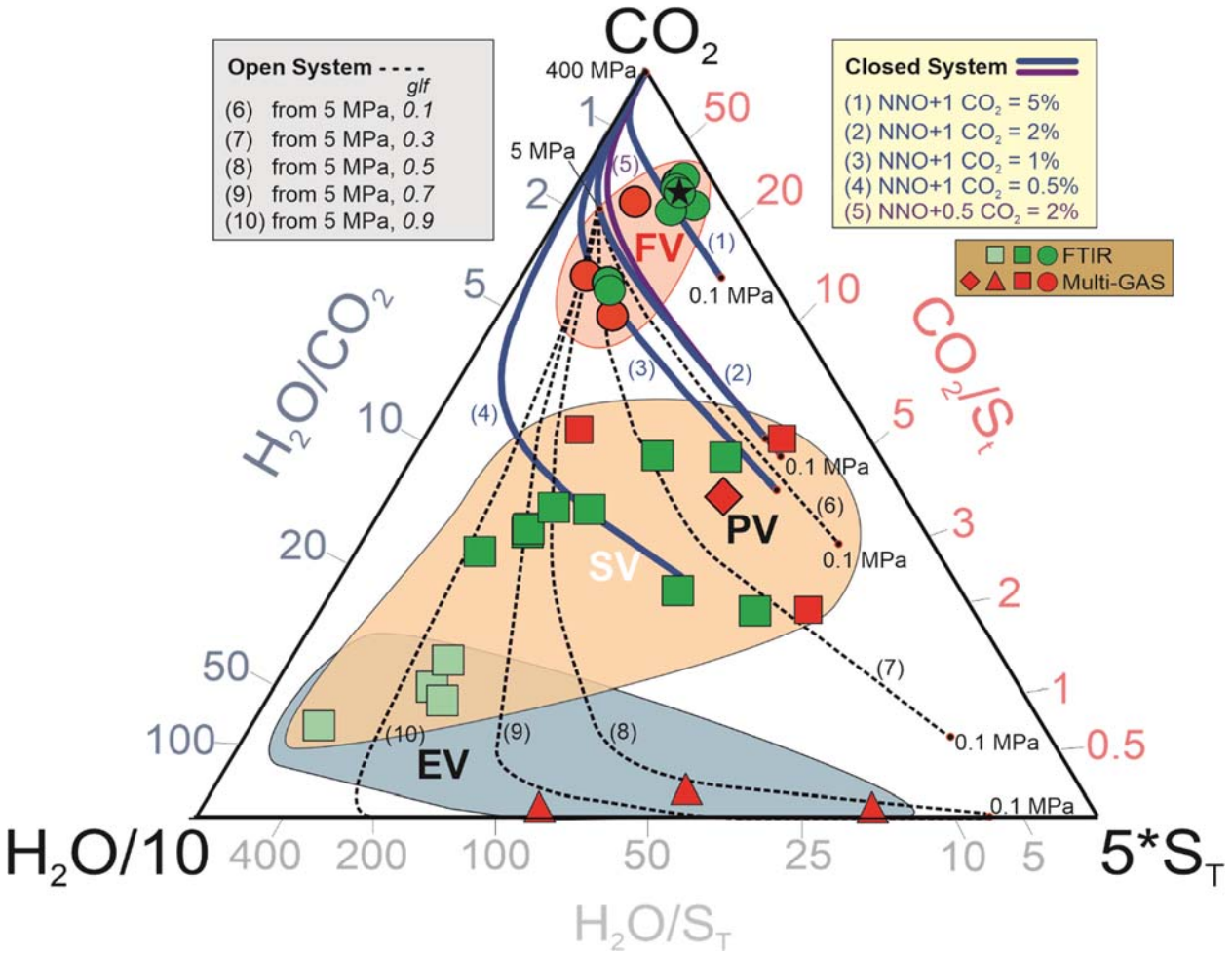

Figure 2: Triangular plot showing H_2O, CO_2 and S_T proportions (H_2O and S_T proportions scaled by factors 0.1 and 5, respectively, for illustration purposes) in gas emissions from the different vents during the 2021 Cumbre Vieja eruption, measured both remotely (OP-FTIR) and directly (Multi-GAS). Upper fountaining vents (FV), spattering vent (SV) and effusive vents (EV) plot in distinct compositional fields. Symbol labelled PV corresponds to the Passively degassing Vent measured during an eruptive pause on 27 September 2021 (see Figure 1 and Extended Data Table 1). Model degassing trends were computed for either closed- or open-system degassing using the solubility model of Moretti et al. (2003). Model runs are identified by numbers (Extended Data Table 3). For the open-system runs we assume all the erupting magma goes towards the effusive vents at a branch point at 5 MPa while a variable proportion, or gas-liquid fraction, glf, of the coexisting gas phase is transported to the explosive vent. Thus a glf of 0.9 indicates a degassing pathway for magma which lost 90% of its gas at 5 MPa to the explosive vent and then erupted at the effusive vent.

We interpret the gas composition data in the context of the distinct eruptive style observed at the fountaining vents (FV) compared with spattering and effusive vents (SV and EV). We propose that that magma and exsolved gas ascended rapidly as a near-closed system to a shallow branch

point, at which point gas-melt decoupling occurred. Most exsolved gas continued ascending vertically to fuel explosive fragmentation at the FV, whilst most of the magma erupted at the SV and EV; this is a typical dynamic in low-viscosity scoria cone-forming eruptions[41]. In this conceptual model, the gas emitted at the FV exsolved and last equilibrated at relatively high pressure and is therefore CO_2-rich and depleted in SO_2 and H_2O, while gas emitted at the SV and EV is dominated by magma degassing above the branch point (at low pressure and therefore rich in H_2O and SO_2 and CO_2-poor).

Ultimately, the final gas compositions at FV, SV and EV are controlled by the relative distributions of gas and magma between FV and EV/SV at the branch—which depends on geometry and fluid dynamics—and the dissolved concentration of SO_2 and H_2O remaining in the magma at the branch point. In **figure 2** we assume that the branch point is at 10 MPa, approximately 400 m, and that all magma is erupted at the EV/SV (i.e. an end-member assumption).

Comparing our observations with modelled degassing trajectories shows that closed-system degassing with 0.5 wt% CO_2 (run 4) cannot reproduce the CO_2-rich FV compositions, confirming that maximum CO_2 concentrations measured in melt inclusions (0.5 wt%) underestimate the initial CO_2 abundance and instead reflect a melt that has exsolved much of its initial CO_2. FV compositions require closed-system degassing of a magma containing between 1 and 5 wt% initial CO_2 (runs 1-3, & 5) with gas and melt remaining in equilibrium until the inferred branch point between FV and SV/EV (**Extended Data Figure 3**). In contrast, EV (and many SV) gas compositions can only be reproduced with open-system degassing from 5 MPa to atmospheric pressure.

An important result of our modelling is that the relatively oxidised melt produces an unusually high S solubility, such that most of the initial sulphur is still dissolved at the branch point between FV and SV/EV (**Extended Data Figure 3b**). The rapid magma ascent would also produce a kinetic limit on gas exsolution. This result provides a critical control on the gas compositions produced at FV and SV/EV and means that the SO_2 flux produced at the FV and SV/EV is controlled largely by the mass eruption rate (MER) at each vent, while the CO_2 flux is predominantly emitted at the FV. This explains the observed high CO_2/SO_2 ratio at the FV and much lower CO_2/SO_2 ratio at the SV/EV. We highlight that the MER at the fountaining vents is critical to determine the initial magmatic CO_2 content because, together with the total MER, the total SO_2 flux and the initial S content, this controls the CO_2/SO_2 ratio observed at the fountaining vents. The calculations used to determine the initial CO_2 concentrations are provided in Extended Data Tables 4 and 5, and the mass-balance approach we used is described below.

We quantify the total SO_2 flux using TROPOMI data collected from the Sentinel-5P satellite, analysed with a back-trajectory approach called PlumeTraj to determine the height, age and SO_2 mass in each pixel[21]. Here we report the initial CO_2 content for two cases: (1) focusing on a particular measurement day, 3rd October 2021, when simultaneous Multi-GAS, FTIR and TROPOMI measurements were made, and (2) considering the integrated emissions and MERs for the entire eruption.

On 3rd October, there was strong and sustained explosive activity at the summit vents during the day, accompanied by voluminous lava effusion from SV and EV. Our TROPOMI/PlumeTraj measurements indicate that the average SO_2 flux was 860 ± 450 kg/s and the height of the eruption plume was 4500 ± 200 m, confirmed by observations of the plume height from a camera

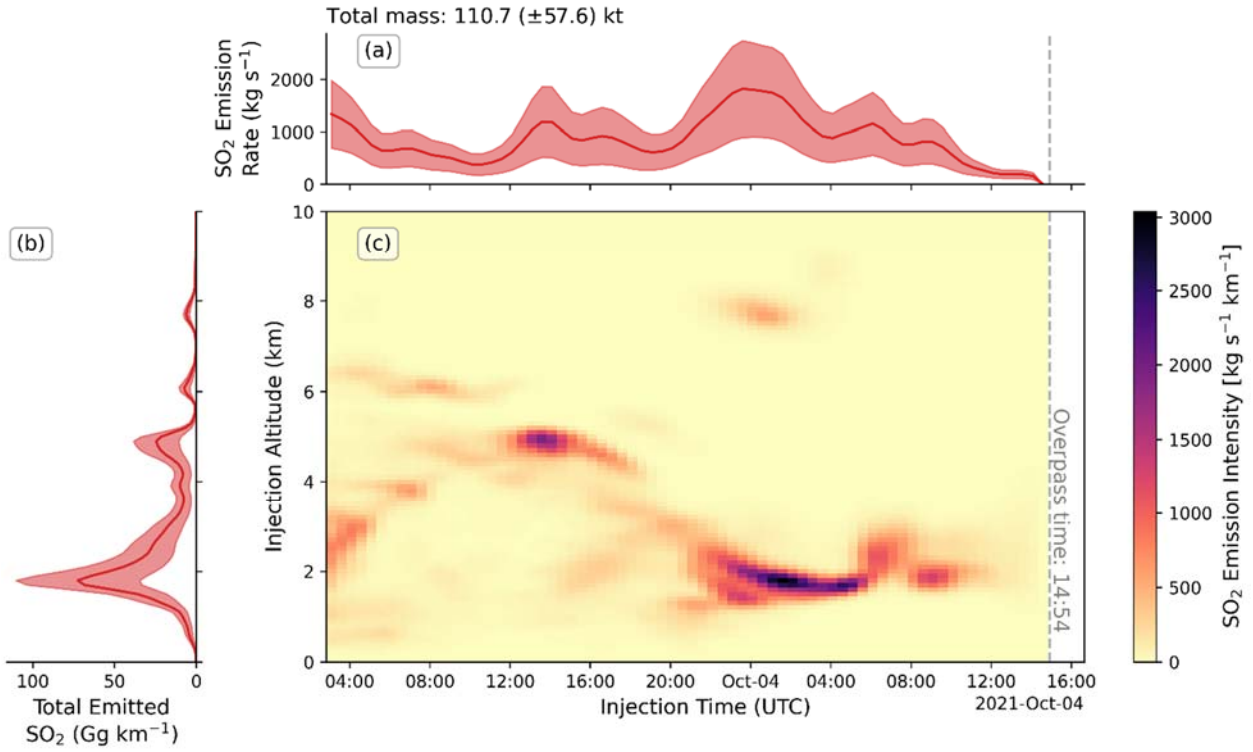

Figure 3: Plume heights and fluxes retrieved from PlumeTraj/TROPOMI for 3-4 October 2021 during the 2021 Tajogaite eruption, La Palma. (a) SO_2 emission rate calculated over 36 hours from a single TROPOMI SO_2 observation collected at 14:54 UTC on 4th October, by binning and integration of SO_2 from individual pixels in 10-minute time bins. Errors reflect wind and SO_2 quantification uncertainty. 111 kt SO_2 over 36 hours reflects an average SO_2 flux of 860 kg/s. (b) Height distribution of SO_2 emissions, dominated by a lower altitude persistent SO_2 emission from the lava field, and intermittent fountaining at the uppermost vents. (c) Emission intensity showing the evolution of SO_2 flux as a function of height and time.

at the Instituto Astrofísico de Canarias (IAC), 2,365 m a.s.l. and 16.5 km north of the eruption[42]. The height of the cone was measured as 1100 m[33] and therefore the net plume height was 3400 m. We quantify an explosive MER from this plume height of 22600 ± 3300 kg/s using published scaling relationships [43] (**Extended Data Table 4**). This compares with 9000 kg/s attributed to the tephra and cone deposit[42], with the difference arising from the mass of ash emitted into the atmosphere and transported more distally. Lava effusion rates were reported as 60 m^3/s on 27th September [33] and 30 ± 15 m^3/s on 3rd October[44], and we use

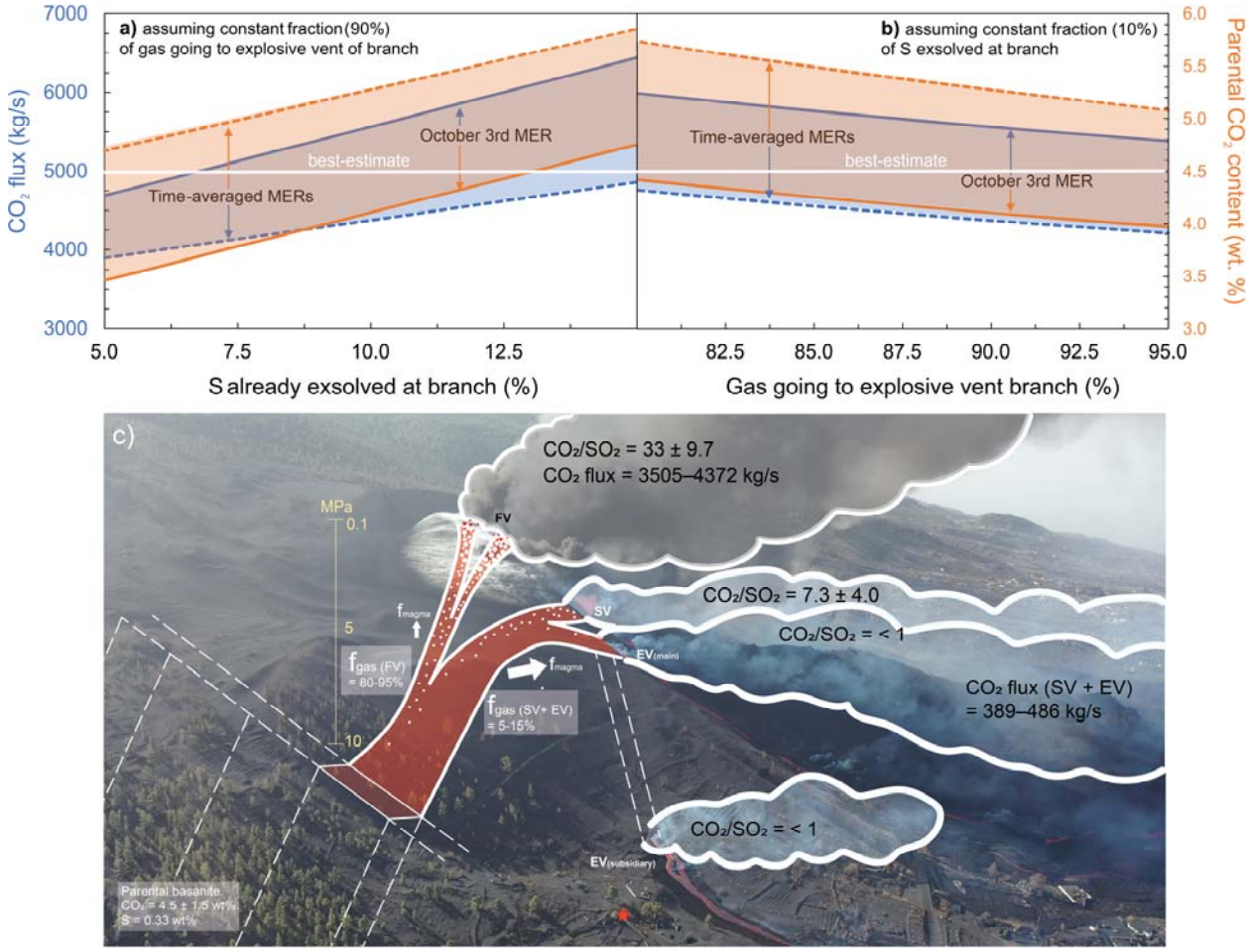

Figure 4: Parental CO_2 content and total eruptive CO_2 flux computed from mass balance calculations (Extended Data Table 5). Panel (a) shows the range of variation of these two parameters when, at the branch point (about 10 MPa), the exsolved fraction of initial S is varied from 5 to 15 % and 90% of the total exsolved at that point migrate in FV conduit. In panel (b) the latter is varied from 80 to 95%, while the exsolved fraction of initial S is kept constant at 10%. In both plots, the solid and dashed lines delineate the ranges in CO_2 content and flux obtained by considering magma eruption rates (MER) and SO_2 fluxes on October 3rd and for the entire eruption, respectively. c) Photo of Tajogaite volcanic cone (drone flight on 2nd October) and schematic cross-section of the shallow (0.1-10 MPa)-conduit system feeding FV, SV and EV vents that best explains our observations and the above results. From about 10 MPa the eruption feeder dyke (D'Auria et al., 2022) transitions into branched conduits where most of the CO_2-rich gas flux (f_{gas}) is preferentially channelled into subvertical FV conduit, sustaining powerful lava fountain, whereas magma influx (f_{magma}) predominantly concentrates through SV conduit then EV drains. The star points to our MultiGas and FTIR measuring site on 3rd October.

43 ± 15 m^3/s for our calculations. This yields an effusive effusion MER of 113000±40000 kg/s using a measured lava density of 2618 ± 179 kg/s[42].

From the melt inclusion analysis we have the initial S content as 3290 ± 390 ppm and a final content from measurements of glass of 440 ppm. Assuming a negligible initial crystal load and that all crystals that formed during ascent were retained we can correct the final S content for crystallisation-induced enhancement of S concentration in the residual melt and quantify a bulk

final S content of 250 ppm. In **Extended Data Table 5** the key parameters described above constrain much of the degassing system, but two key parameters remain to be defined. These are the quantity of SO_2 which had exsolved at the pressure of the branch point between effusive and explosive conduits, and the percentage of total exsolved gas which was transferred to the explosive vents. There was ~200 m height difference between the effusive vents and the fountaining vents, and these probably joined even deeper within the system at the branch point, so we estimate a 400 m depth and approximately 10 MPa. Using the S solubility vs. pressure relationship shown in **Extended Data figure 3** this implies only 5-10% of the initial S was exsolved. This will be modified by kinetic controls and is an upper limit. The percentage of exsolved gas entering the FV conduit can be estimated by volcanological observation, as there was only mild spattering at the SV, if a significant percentage of gas were entering this then we would expect to see more vigorous activity. Our best estimate is 90 ± 10% of the exsolved gas ascending directly to the fountaining vents and 10% was carried to the spattering and effusive vents.

With a 10% exsolution of S at the branch point and 90% of exsolved gas entering the FV, for the 3rd October we calculate an initial CO_2 content of 4.5 ± 1.5 wt% is required to explain the observed CO_2/SO_2 mass ratio of 24 (see figure 4). The calculated SO_2 flux produced in this approach matches the observed SO_2 flux of 860 kg/s (**Extended Data Table 5)**. We can do the same calculation for the time averaged effusion and explosive MERs, reported as 63000 kg/s for the effusion and 10000 kg/s for the tephra and cone[42], which we estimate is also the same MER for the total airborne ash emissions. The time-averaged SO_2 flux comes from the TROPOMI-PlumeTraj data and is 600 kg/s(Burton et al., in review). With the same assumptions as above we calculate an initial CO_2 content of 5.3 wt% and again a good agreement between calculated and observed average SO_2 flux. Overall, the range of initial CO_2 concentrations which can be produced in this mass balance approach is 3.3 wt% to 5.7 wt%, by varying between 5-10% pre-exsolved SO_2 and 80-95% exsolved gas entering the FV conduit, and our best estimate is 4.5 wt% (figure 4).

An initial CO_2 content of 4.5 wt% corresponds to a daily average emission rate of 0.33 ± 0.16 Mt d^{-1} of CO_2, and an overall CO_2 emission of 28 ± 14 Mt. This emitted mass is unprecedently high compared to previously reported volcanic CO_2 flux measurements at other volcanoes[25,26,45]. Such an initial magmatic CO_2 content ranks as the highest yet calculated from analysis of gas emissions during an eruption. It is the upper end of estimated parental melt CO_2 contents from the nearby 2011-2012 Tagoro volcano (El Hierro) (2.5 to 4.2 wt.%), based on dissolved/exsolved volatiles in melt inclusions and trace element ratios[30,46]. A high CO_2 content in La Palma basanite is consistent with a low degree of partial melting of a mantle source metasomatized by recycled components, as also proposed for Tagoro magmas[30,31,46].

Notably, at the intermediate magma storage zone of ~10-15 km depth (ca. 275-410 MPa), where most of the syn-eruptive seismicity was occurring (D'Auria et al., 2022), CO_2 solubility in La Palma basanitic melts is predicted by solubility models[40] to be only 0.25 to 0.6 wt%. Therefore, an important implication of our results is that about 3.9 wt% of CO_2 was already exsolved at these seismogenic depths, in agreement with the presence of CO_2 in fluid inclusions from depths

shallower than 27 km[9,36]. Under these conditions at least 1 wt% of H_2O may have coexisted with CO_2 in the exsolved fluid phase[40]. We thus verify that basanitic magma stored at depths <27 km coexisted with an abundant exsolved fluid phase, which not only enhanced the explosivity of the eruption but also increased the magma compressibility, buffering volumetric changes during depressurization as the magma was erupted[47].

The volatile-rich nature of the 2021 Cumbre Vieja magma, particularly with respect to CO_2, highlights that large magnitude volatile emissions can be produced by intraplate alkaline ocean volcanism from mantle sources previously enriched in recycled oceanic crust. This observation suggests that throughout Earth's history the formation of ocean islands may have made a significant contribution to the geological carbon cycle. During the initial submarine formation of La Palma, there would have been substantial emission of volatiles into the ocean, followed by subaerial discharge once the island breached the surface. La Palma has a maximum height of 6423 m from ocean floor to summit and is therefore one of the tallest volcanic edifices on the planet. Its total submarine volume is estimated to be 3300 km^3 from topographic surveys[48,49]. Its subaerial age is 1.7 Ma and volume is 600 km^3 [50-52], composed of a combination of gabbro, basanite and phonolite. Assuming for simplicity that basanite is the average composition of the entire edifice and initially contains 4.5 wt% CO_2, we estimate a maximum discharge of 68,000 Mt CO_2 ($1.6x10^{15}$ moles) of CO_2 during La Palma's subaerial growth (**Extended Data Table 4**). Assuming the same eruption rate throughout La Palma's history implies a total age of ~12 Ma and a total CO_2 production of 475,000 Mt ($1.1x10^{16}$ moles). This is equivalent to ca. 20% of the estimated CO_2 release from a typical large igneous province[27], many of which are implicated in periods of major environmental and climatic change in Earth's history. Considering that La Palma is amongst the smaller of the eight main islands composing the Canary archipelago, we suggest that the integrated CO_2 emissions associated with the construction of the entire archipelago may have approached that of a LIP.

Data and code availability

All results from field campaigns and further analysis are contained within the extended data tables included in the submission. The solubility model code is available here https://github.com/charlesll//chosetto. Original data and analysis codes are available on request.

Figure Captions

Figure 1: The 2021 Tajogaite eruption (Cumbre Vieja, La Palma) and chronology of volcanic gas measurements. (a) The 2021 lava flow field in south-western La Palma. Aerial images of the near-vent eruptive region, showing multiple distinct emission sources, eruptive styles, and degassing regimes (PV, passive vent; FV, fountaining vents; SV; spattering vent; EV, effusive vent). (b, c) Passive emissions during an eruptive pause and immediately following main vent reactivation on 27 September 2021. (d, e) Lateral progression in eruptive style from intense ash-producing lava fountaining activity at the upper vents (FV) through to spattering activity at the lower vent (SV), feeding lava flows; (f) Concurrent lava fountaining, spattering and non-explosive lava effusion on 1 October 2021. The EV opened at the base of the northern flank of the cone and fed lava extrusion for two days. (g) Temporal evolution of CO_2/SO_2 ratios in the gas plumes released by the different vents, as measured with Multi-GAS and OP-FTIR spectroscopy. Symbols indicate vent source (diamond = eruptive pause; circle = FV; square = SV (four especially water-rich

compositions – see Figure 2 - are identified with light green tone); and triangle = EV). The star highlights the highest quality FV measurement.

Figure 2: Triangular plot showing H_2O, CO_2 and S_T proportions (H_2O and S_T proportions scaled by factors 0.1 and 5, respectively, for illustration purposes) in gas emissions from the different vents during the 2021 Cumbre Vieja eruption, measured both remotely (OP-FTIR) and directly (Multi-GAS). Upper fountaining vents (FV), spattering vent (SV) and effusive vents (EV) plot in distinct compositional fields. Symbol labelled PV corresponds to the Passively degassing Vent measured during an eruptive pause on 27 September 2021 (see Figure 1 and Extended Data Table 1). Model degassing trends were computed for either closed- or open-system degassing using the solubility model of Moretti et al. (2003). Model runs are identified by numbers (Extended Data Table 3). For the open-system runs we assume all the erupting magma goes towards the effusive vents at a branch point at 5 MPa while a variable proportion of the coexisting gas phase is transported to the explosive vent. Thus a glf of 0.9 indicates a degassing pathway for magma which lost 90% of its gas at 5 MPa to the explosive vent and then erupted at the effusive vent.

Figure 3: Plume heights and fluxes retrieved from PlumeTraj/TROPOMI for 3-4 October 2021 during the 2021 Tajogaite eruption, La Palma. (a) SO_2 emission rate calculated over 36 hours from a single TROPOMI SO_2 observation collected at 14:54 UTC on 4th October, by binning and integration of SO_2 from individual pixels in 10-minute time bins. Errors reflect wind and SO_2 quantification uncertainty. 111 kt SO_2 over 36 hours reflects an average SO_2 flux of 860 kg/s. (b) Height distribution of SO_2 emissions, dominated by a lower altitude persistent SO_2 emission from the lava field, and intermittent fountaining at the uppermost vents. (c) Emission intensity showing the evolution of SO_2 flux as a function of height and time.

Figure 4: Parental CO_2 content and total eruptive CO_2 flux computed from mass balance calculations (Extended Data Table 5). Panel (a) shows the range of variation of these two parameters when, at the branch point (about 10 MPa), the exsolved fraction of initial S is varied from 5 to 15 % and 90% of the total exsolved at that point migrate in FV conduit. In panel (b) the latter is varied from 80 to 95%, while the exsolved fraction of initial S is kept constant at 10%. In both plots, the solid and dashed lines delineate the ranges in CO_2 content and flux obtained by considering magma eruption rates (MER) and SO_2 fluxes on October 3rd and for the entire eruption, respectively. c) Photo of Tajogaite volcanic cone (drone flight on 2nd October) and schematic cross-section of the shallow (0.1-10 MPa)-conduit system feeding FV, SV and EV vents that best explains our observations and the above results. From about 10 MPa the eruption feeder dyke (D'Auria et al., 2022) transitions into branched conduits where most of the CO_2-rich gas flux (f_{gas}) is preferentially channelled into subvertical FV conduit, sustaining powerful lava fountain, whereas magma influx (f_{magma}) predominantly concentrates through SV conduit then EV drains. The star points to our MultiGas and FTIR measuring site on 3rd October.

References

1 Sparks, R. S. J. Forecasting volcanic eruptions. *Earth and Planetary Science Letters* **210**, 1-15 (2003). https://doi.org:10.1016/s0012-821x(03)00124-9

2 Jambon, A. EARTH DEGASSING AND LARGE-SCALE GEOCHEMICAL CYCLING OF VOLATILE ELEMENTS. *Volatiles in Magmas* **30**, 479-517 (1994).

3 Ernst, R. E. & Youbi, N. How Large Igneous Provinces affect global climate, sometimes cause mass extinctions, and represent natural markers in the geological record. *Palaeogeography Palaeoclimatology Palaeoecology* **478**, 30-52 (2017). https://doi.org:10.1016/j.palaeo.2017.03.014

4 Eguchi, J. & Dasgupta, R. A CO2 solubility model for silicate melts from fluid saturation to graphite or diamond saturation. *Chemical Geology* **487**, 23-38 (2018). https://doi.org:10.1016/j.chemgeo.2018.04.012

5 Moretti, R., Papale, P. & Ottonello, G. A model for the saturation of C-O-H-S fluids in silicate melts. *Volcanic Degassing* **213**, 81-101 (2003). https://doi.org:10.1144/gsl.sp.2003.213.01.06

6 Hartley, M. E., Maclennan, J., Edmonds, M. & Thordarson, T. Reconstructing the deep CO2 degassing behaviour of large basaltic fissure eruptions. *Earth and Planetary Science Letters* **393**, 120-131 (2014). https://doi.org:10.1016/j.epsl.2014.02.031

7 Metrich, N. & Wallace, P. J. in *Minerals, Inclusions and Volcanic Processes* Vol. 69 *Reviews in Mineralogy & Geochemistry* (eds K. D. Putirka & F. J. Tepley) 363-402 (2008).

8 Maclennan, J. Bubble formation and decrepitation control the CO2 content of olivine-hosted melt inclusions. *Geochemistry Geophysics Geosystems* **18**, 597-616 (2017). https://doi.org:10.1002/2016gc006633

9 Dayton, K. *et al.* Deep magma storage during the 2021 La Palma eruption. *Science Advances* **9**, eade7641 (2023). https://doi.org:doi:10.1126/sciadv.ade7641

10 Longpre, M. A., Klugel, A., Diehl, A. & Stix, J. Mixing in mantle magma reservoirs prior to and during the 2011-2012 eruption at El Hierro, Canary Islands. *Geology* **42**, 315-318 (2014). https://doi.org:10.1130/g35165.1

11 Spilliaert, N., Allard, P., Metrich, N. & Sobolev, A. V. Melt inclusion record of the conditions of ascent, degassing, and extrusion of volatile-rich alkali basalt during the powerful 2002 flank eruption of Mount Etna (Italy). *Journal of Geophysical Research-Solid Earth* **111** (2006). https://doi.org:10.1029/2005jb003934

12 Aiuppa, A., Casetta, F., Coltorti, M., Stagno, V. & Tamburello, G. Carbon concentration increases with depth of melting in Earth's upper mantle. *Nature Geoscience* **14**, 697-+ (2021). https://doi.org:10.1038/s41561-021-00797-y

13 Saal, A. E., Hauri, E. H., Langmuir, C. H. & Perfit, M. R. Vapour undersaturation in primitive mid-ocean-ridge basalt and the volatile content of Earth's upper mantle. *Nature* **419**, 451-455 (2002). https://doi.org:10.1038/nature01073

14 Matthews, S., Shorttle, O., Rudge, J. F. & Maclennan, J. Constraining mantle carbon: CO2-trace element systematics in basalts and the roles of magma mixing and degassing. *Earth and Planetary Science Letters* **480**, 1-14 (2017). https://doi.org:10.1016/j.epsl.2017.09.047

15 Burton, M. R., Mader, H. M. & Polacci, M. The role of gas percolation in quiescent degassing of persistently active basaltic volcanoes. *Earth and Planetary Science Letters* **264**, 46-60 (2007). https://doi.org:10.1016/j.epsl.2007.08.028

16 Allard, P., Burton, M. & Mure, F. Spectroscopic evidence for a lava fountain driven by previously accumulated magmatic gas. *Nature* **433**, 407-410 (2005). https://doi.org:10.1038/nature03246

17 Burton, M., Allard, P., Mure, F. & La Spina, A. Magmatic gas composition reveals the source depth of slug-driven Strombolian explosive activity. *Science* **317**, 227-230 (2007). https://doi.org:10.1126/science.1141900

18 Aiuppa, A. *et al.* Total volatile flux from Mount Etna. *Geophysical Research Letters* **35** (2008). https://doi.org:10.1029/2008gl035871

19 Galle, B. *et al.* A miniaturised ultraviolet spectrometer for remote sensing of SO2 fluxes: a new tool for volcano surveillance. *Journal of Volcanology and Geothermal Research* **119**, 241-254 (2003). https://doi.org:10.1016/s0377-0273(02)00356-6
20 Carn, S. A., Fioletov, V. E., McLinden, C. A., Li, C. & Krotkov, N. A. A decade of global volcanic SO2 emissions measured from space. *Scientific Reports* **7** (2017). https://doi.org:10.1038/srep44095
21 Burton, M., Hayer, C., Miller, C. & Christenson, B. Insights into the 9 December 2019 eruption of Whakaari/White Island from analysis of TROPOMI SO2 imagery. *Science Advances* **7** (2021). https://doi.org:10.1126/sciadv.abg1218
22 Pardini, F. B., M., Arzilli, F., La Spina, G., Polacci, M. SO2 emissions, plume heights and magmatic processes inferred from satellite data: The 2015 Calbuco eruptions. *Journal of Volcanology and Geothermal Research* **64232**, 13 (2018).
23 Anderson, K. R. & Poland, M. P. Bayesian estimation of magma supply, storage, and eruption rates using a multiphysical volcano model: Kilauea Volcano, 2000-2012. *Earth and Planetary Science Letters* **447**, 161-171 (2016). https://doi.org:10.1016/j.epsl.2016.04.029
24 Blundy, J., Cashman, K. V., Rust, A. & Witham, F. A case for CO2-rich arc magmas. *Earth and Planetary Science Letters* **290**, 289-301 (2010). https://doi.org:10.1016/j.epsl.2009.12.013
25 Werner, C. *et al.* Carbon Dioxide Emissions from Subaerial Volcanic Regions Two Decades in Review. *Deep Carbon: Past to Present*, 188-236 (2020).
26 Burton, M. R., Sawyer, G. M. & Granieri, D. Deep Carbon Emissions from Volcanoes. *Carbon in Earth* **75**, 323-354 (2013). https://doi.org:10.2138/rmg.2013.75.11
27 Mills, B., Daines, S. J. & Lenton, T. M. Changing tectonic controls on the long-term carbon cycle from Mesozoic to present. *Geochemistry Geophysics Geosystems* **15**, 4866-4884 (2014). https://doi.org:10.1002/2014gc005530
28 Allard, P. *et al.* ERUPTIVE AND DIFFUSE EMISSIONS OF CO2 FROM MOUNT ETNA. *Nature* **351**, 387-391 (1991). https://doi.org:10.1038/351387a0
29 Oppenheimer, C. *et al.* Mantle to surface degassing of alkalic magmas at Erebus volcano, Antarctica. *Earth and Planetary Science Letters* **306**, 261-271 (2011). https://doi.org:10.1016/j.epsl.2011.04.005
30 Longpre, M. A., Stix, J., Klugel, A. & Shimizu, N. Mantle to surface degassing of carbon- and sulphur-rich alkaline magma at El Hierro, Canary Islands. *Earth and Planetary Science Letters* **460**, 268-280 (2017). https://doi.org:10.1016/j.epsl.2016.11.043
31 Day, J. M. D., Pearson, D. G., Macpherson, C. G., Lowry, D. & Carracedo, J. C. Evidence for distinct proportions of subducted oceanic crust and lithosphere in HIMU-type mantle beneath El Hierro and La Palma, Canary Islands. *Geochimica Et Cosmochimica Acta* **74**, 6565-6589 (2010). https://doi.org:10.1016/j.gca.2010.08.021
32 Romero, J. E. *et al.* The initial phase of the 2021 Cumbre Vieja ridge eruption (Canary Islands): Products and dynamics controlling edifice growth and collapse. *Journal of Volcanology and Geothermal Research* **431** (2022). https://doi.org:10.1016/j.jvolgeores.2022.107642
33 Civico, R. *et al.* High-resolution Digital Surface Model of the 2021 eruption deposit of Cumbre Vieja volcano, La Palma, Spain. *Scientific Data* **9** (2022). https://doi.org:10.1038/s41597-022-01551-8
34 Bonadonna, C., Folch, A., Loughlin, S. & Puempel, H. Future developments in modelling and monitoring of volcanic ash clouds: outcomes from the first IAVCEI-WMO workshop on Ash Dispersal Forecast and Civil Aviation. *Bulletin of Volcanology* **74**, 1-10 (2012). https://doi.org:10.1007/s00445-011-0508-6

35 Day, J. M. D. *et al.* Mantle source characteristics and magmatic processes during the 2021 La Palma eruption. *Earth and Planetary Science Letters* **597** (2022). https://doi.org:10.1016/j.epsl.2022.117793
36 Zanon, V. *et al.* in *EGU General Assembly 2022* (Copernicus, Vienna, Austria, 2022).
37 D'Auria, L. *et al.* Rapid magma ascent beneath La Palma revealed by seismic tomography. *Scientific Reports* **12** (2022). https://doi.org:10.1038/s41598-022-21818-9
38 La Spina, A., Burton, M. & Salerno, G. G. Unravelling the processes controlling gas emissions from the central and northeast craters of Mt. Etna. *Journal of Volcanology and Geothermal Research* **198**, 368-376 (2010). https://doi.org:10.1016/j.jvolgeores.2010.09.018
39 Aiuppa, A., Fischer, T. P., Plank, T., Robidoux, P. & Di Napoli, R. Along-arc, inter-arc and arc-to-arc variations in volcanic gas CO2/S-T ratios reveal dual source of carbon in arc volcanism. *Earth-Science Reviews* **168**, 24-47 (2017). https://doi.org:10.1016/j.earscirev.2017.03.005
40 Jimenez-Mejias, M., Andujar, J., Scaillet, B. & Casillas, R. Experimental determination of H2O and CO2 solubilities of mafic alkaline magmas from Canary Islands. *Comptes Rendus Geoscience* **353** (2021). https://doi.org:10.5802/crgeos.84
41 Pioli, L., Azzopardi, B. J. & Cashman, K. V. Controls on the explosivity of scoria cone eruptions: Magma segregation at conduit junctions. *Journal of Volcanology and Geothermal Research* **186**, 407-415 (2009). https://doi.org:https://doi.org/10.1016/j.jvolgeores.2009.07.014
42 Bonadonna, C. *et al.* Physical Characterization of Long-Lasting Hybrid Eruptions: The 2021 Tajogaite Eruption of Cumbre Vieja (La Palma, Canary Islands). *Journal of Geophysical Research-Solid Earth* **127** (2022). https://doi.org:10.1029/2022jb025302
43 Mastin, L. G. *et al.* A multidisciplinary effort to assign realistic source parameters to models of volcanic ash-cloud transport and dispersion during eruptions. *Journal of Volcanology and Geothermal Research* **186**, 10-21 (2009). https://doi.org:10.1016/j.jvolgeores.2009.01.008
44 Plank, S. *et al.* Combining thermal, tri-stereo optical and bi-static InSAR satellite imagery for lava volume estimates: the 2021 Cumbre Vieja eruption, La Palma. *Scientific Reports* **13**, 2057 (2023). https://doi.org:10.1038/s41598-023-29061-6
45 Aiuppa, A., Fischer, T. P., Plank, T. & Bani, P. CO2 flux emissions from the Earth's most actively degassing volcanoes, 2005-2015. *Scientific Reports* **9** (2019). https://doi.org:10.1038/s41598-019-41901-y
46 Taracsak, Z. *et al.* High fluxes of deep volatiles from ocean island volcanoes: Insights from El Hierro, Canary Islands. *Geochimica Et Cosmochimica Acta* **258**, 19-36 (2019). https://doi.org:10.1016/j.gca.2019.05.020
47 Kilbride, B. M., Edmonds, M. & Biggs, J. Observing eruptions of gas-rich compressible magmas from space. *Nature Communications* **7** (2016). https://doi.org:10.1038/ncomms13744
48 Masson, D. G. *et al.* Slope failures on the flanks of the western Canary Islands. *Earth-Science Reviews* **57**, 1-35 (2002). https://doi.org:10.1016/s0012-8252(01)00069-1
49 Mitchell, N. C., Masson, D. G., Watts, A. B., Gee, M. J. R. & Urgeles, R. The morphology of the submarine flanks of volcanic ocean islands - A comparative study of the Canary and Hawaiian hotspot islands. *Journal of Volcanology and Geothermal Research* **115**, 83-107 (2002). https://doi.org:10.1016/s0377-0273(01)00310-9
50 Guillou, H., Carracedo, J. C. & Duncan, R. A. K-Ar, 40Ar-39Ar ages and magnetostratigraphy of Brunhes and Matuyama lava sequences from La Palma Island. *Journal of Volcanology and Geothermal Research* **106**, 175-194 (2001). https://doi.org:10.1016/s0377-0273(00)00294-8

51 Staudigel, H. & Schmincke, H. U. THE PLIOCENE SEAMOUNT SERIES OF LA PALMA CANARY-ISLANDS. *Journal of Geophysical Research* **89**, 1195-1215 (1984). https://doi.org:10.1029/JB089iB13p11195
52 Staudigel, H., Feraud, G. & Giannerini, G. THE HISTORY OF INTRUSIVE ACTIVITY ON THE ISLAND OF LA-PALMA (CANARY-ISLANDS). *Journal of Volcanology and Geothermal Research* **27**, 299-322 (1986). https://doi.org:10.1016/0377-0273(86)90018-1

Methods

Volcanic gas composition. We measured plume gas composition during the Cumbre Vieja eruption using two independent and complementary techniques: in-situ plume measurements using aerial and ground-based Multi-GAS to characterize plume composition during the initial phase of the eruption (27 September to 4 October 2021) and remote sensing Fourier Transform Infrared (FTIR) spectroscopy observations on 3 October to 2 December 2021 (**Figure 1**). All gas composition results are listed in **Extended Data Table 1**.

Multi-GAS. The multi-component gas analyser system (Multi-GAS) technique was used to measure concentrations of CO_2, SO_2, H_2S ± H_2 (and P, T, RH) in the emitted gases The Multi-GAS was operated as (a) a ground-based mobile instrument, (b) a ground-based fixed station, and (c) an aerial instrument, mounted onboard a DJI Matrice M210 quad-rotor Unoccupied Aerial System (UAS) platform (**Extended Data Table 1**). For all instruments, air is sampled through a 1 µm particle filter exposed to ambient air, at a pump rate of 1.0 L min^{-1}, and sensor data are logged at 1 Hz. SO_2 and H_2S electrochemical sensors (T3ST/F and T3H, both City Technology) were calibrated for 0–200 and 0–200 ppmv, respectively, with an accuracy of ± 2% and a resolution of 0.1 ppmv. A non-dispersive infrared (NDIR) spectrometer - either a Microsensorik Smartgas Modul Premium2 (aerial Multi-GAS; 0-5000 ppm range) or a Edinburgh Gascard ND (ground-based Multi-GAS; 0-10000 ppm range) - were calibrated for CO_2 with an accuracy of ± 2% and a resolution of 1 ppmv. Units are shielded from radio frequency interference using a foil bag. Pressure (±1 hPa), temperature (±0.5˚C) and relative humidity (0-100%; ±3%) were also measured at 1 Hz using either a Bluedot BME280 sensor exposed to ambient air (aerial Multi-GAS) or Galltec sensor connected in series with the other sensors within the unit (ground-based).

UAS flights were undertaken in accordance with EU operating procedures, with airspace permission. Take off locations were from two sites along Carretera San Nicolas, A (28.621302, -17.873859) and B (28.620874, -17.871741), each located ~900 m north of the summit vents (**Extended Data Figure 4**). Flights involved between 30 and 1000 m of vertical ascent, depending on the target vent emissions, and were between 10 and 20 minutes in duration—although typically only a fraction of that time was spent in the dense region of the gas plume.

We measured passive gas emissions during a pause in the eruption on 27 September 2021 from a position hovering several meters above the northern rim of the cone (labelled PV in Figure 1b). The pause lasted several hours before the main upper vent reactivated with vigorous fountaining

595 and ash emission (Figure 1c), approximately 30 minutes after our sampling flight. The reactivation
596 was preceded by the emission of a white steam-rich plume from the lower, spattering vent.

597 The gas plume from the main upper vents producing strong lava fountaining (labelled FV in Figure
598 1) grounded towards the northwest of the cone on 30 September 2021. We measured the gas
599 composition at a distance of approximately ~900 m from the vent using a ground-based Multi-
600 GAS operating in portable mode, by walking traverses through the plume. Subsequently, the unit
601 was installed as a fixed, ground-based station and this remained in place until 2 October 2021
602 when the site became at risk from lava flows. The station was programmed to acquire data for 30
603 mins every hour. The fixed station was exposed periodically to grounding plumes from both the
604 upper, lava fountaining vents (FV) and lower, spattering vent (labelled SV in Figure 1) and these
605 two distinct emission sources produced resolvable CO_2/SO_2 ratios in the time series gas data.
606 The gas emissions from the spattering vent (SV) were measured again on 3 October 2021 much
607 closer to source using an aerial Multi-GAS unit on-board the UAS.

608 An effusive vent opened at the base of the northern flank of the cone overnight between 30
609 September and 1 October 2021 (labelled EV in Figure 1f), producing a lava flow and a strong gas
610 plume. We measured the gas composition from the effusive vent during a UAS flight on 1 October,
611 a few tens of meters downwind from the vent and at around 30 m elevation above ground level.
612 Subsequently, a second effusive vent opened at slightly higher elevation on the northern flank on
613 4 October 2021 and was again sampled using the UAS-mounted aerial Multi-GAS on the same
614 day.

615 Multi-GAS instruments were calibrated with standard reference gases at University of Palermo,
616 Italy, prior to and following the field campaign, but required no instrumental drift corrections. All
617 sensor data are logged locally to a micro-SD card and, for the aerial Multi-GAS, also telemetered
618 directly to the ground station (using a RFD 868x Modem by RFDesign) where it can be viewed in
619 real-time. The angle of the transmission antenna on the landing leg of the UAS required outwards
620 orientation to minimize interference with the landing sensors located beneath the main body of
621 the UAS. H_2O concentrations were calculated from records of temperature and relative humidity,
622 using the ambient pressure at the measurement altitude, according to the Arden Buck equations
623 relating the pressure of vapor saturation to temperature for moist air. We post-processed gas
624 concentration time series using Ratiocalc software(Tamburello, 2015) and R. H_2S concentrations
625 were corrected for the 13% cross-sensitivity of the sensor to SO_2 (determined during calibration
626 with standard reference gases).

627 **OP-FTIR.** Two OP-FTIR spectrometers were deployed to measure the gas compositions
628 produced by the eruptive vents, and lava flows. The OP-FTIR is a very powerful and flexible
629 instrument, and when performing absorption measurements can work wherever there is cooler
630 magmatic gas observed in front of a warmer radiation source. We used it in both passive and
631 solar absorption modes. Passive measurements were conducted using incandescent ash
632 eruption, lava fountaining and lava flow sources(Allard et al., 2016; Burton et al., 2003; La Spina
633 et al., 2015; La Spina et al., 2013; Oppenheimer et al., 2006; Pfeffer et al., 2018). Passive
634 measurements provide constraints on H_2O, CO_2, SO_2 and HCl, but because there are multiple
635 gas sources each with a distinct gas composition the total CO_2 and H_2O emission rates must be

estimated by summation of the relative emission rates of each eruptive style. FTIR spectra were analysed using the FTIR_FIT software(Burton et al., 2007) written in the IDL language and available on request. FTIR_FIT works in a similar manner to iFit(Esse et al., 2020), reproducing the measured intensity spectrum using a forward model built upon the RFM radiative transfer model and the HITRAN 2008 database.

FTIR observations were taken in a variety of eruptive vents and activity styles from October 3 to December 4 (**Extended Data Table 1**). As an illustration, we detail our measurements on October 3, when we operated simultaneously two OP-FTIR spectrometers; a first one measured degassing from the main lava spattering flank vent (SV), from a distance of 0.7 km in the Tacande Village area, while the other was targeting the ash-rich eruptive column from summit vents (FV) from a distance of 3 km (figure 5). Eruptive activity at the latter vents gradually increased in intensity as the measurements progressed, and we observed a mixed gas emission, partly arising from the SV and partly from the FV. Gas emissions from the SV clearly reflected a secondary, CO_2-depleted degassing stage of the magma, but still displaying a high CO_2/SO_2 molar ratio up to 11, plus $SO_2/HCl = 8$ and $H_2O/SO_2 = 126$ (**Extended Data Table 1**). Explosive degassing from the FV showed variable compositions at different times, due to the changing conditions in ash content, eruption intensity, and interference with the drifting plume from the SV. **Extended Data Table 1** lists the October 3 gas compositions measured successively during 5 intervals of ~10 minutes each. The increasing intensity of explosive activity during this sequence is reflected in an increasing cleanness of the chemical signature of the main summit degassing, with CO_2/SO_2 ratios increasing up to 33.6 while SO_2/HCl ratio remained in the range from 6 to 10 (**Extended Data Table 1**). On the evening of November 6, the eruptive activity shifted from ash-rich to Strombolian/lava fountaining, and we measured the lava fountain degassing from a distance of 5 km (dos Pinos area). We again recorded $CO_2/SO_2 = 33.5$, but also high SO_2/HCl ratios (20.7) that suggest weaker Cl exsolution during lava fountaining (La Spina et al., 2015). After a pause in explosive activity at the summit on 2nd December, a powerful sequence of continuous jetting of lava and gas started from a new vent cutting the NE flank of the grown main cone. We measured this sequence at 600 m from the vent, at Cabeza de Vaca, and obtained FTIR spectra of extremely high quality. The results further provided a high CO_2/SO_2 of 35.8, with $SO_2/HCl = 16.8$ and $H_2O/SO_2 = 22.4$. This is our best compositional record of the FV eruptive plume.

Analyses of silicate melt inclusions and matrix glasses. We measured the volatile contents of olivine-hosted glassy melt inclusions and the groundmass glass of rapidly quenched air fall tephra. Major and minor elements plus sulfur, fluorine and chlorine in melt inclusions and matrix glasses were measured by electron microprobe in two independent laboratories in Paris (France) and Bristol University (UK). Analytical procedures are fully detailed in the **Supplementary Material S1**

Melt inclusions, corrected for post-entrapment crystallization, are basanitic in composition, and contain 40.2-46.4 wt.% SiO_2, 2.8-4.5 wt.% TiO_2, 4.4-6.3 wt.% MgO and 1.1-2.1 wt.% K_2O (**Extended Data Figure 1; Extended Data Table 2**). Embayments and matrix glasses have more evolved and overlapping compositions, containing 43.0-49.5 wt.% SiO_2, 1.4-4.1 wt.% TiO_2, 0.8-5.3 wt.% MgO and 1.0-2.9 wt.% K_2O (**Extended Data Figure 1**). The olivines hosting melt inclusions and embayments have compositions between Fo78 and Fo85 (**Extended Data Figure**

2). The mean melt inclusion S content is 3290 µg/g; one sulfur-rich inclusion contains 4871 µg/g S, and the highest S content in the main melt inclusion population is 3715 µg/g (**Extended Data Figure 1, Extended Data Figure 2**). Groundmass glasses have a mean S content of 474 µg/g, indicating that approximately 85% of magmatic sulfur was outgassed during magma ascent and eruption (**Supplementary Material**), as also tracked by glassy embayments trapped at the rim of crystals in comparison to sulfur, chlorine and fluorine show only minor outgassing during ascent:dissolved concentrations respectively vary from ca 450-1050 µg/g Cl and 1000-1500 µg/g F in melt inclusions, to ca. 1400 µg/g Cl and 1000-1500 µg/g F in groundmass glass and melt embayment (fluorine reaching up to 2200 µg/g in one embayment). Fluorine and chlorine become progressively more enriched as melt inclusions and glass compositions become more evolved, indicating that melt F and Cl contents are primarily governed by a fractional crystallization relationship. Embayments and groundmass glasses have similar F and Cl contents, suggesting that syn-eruptive F and Cl outgassing at the vents was inefficient. H_2O and CO_2 were determined in three melt inclusions only (**Extended Data Table 2**).. Analyzed groundmass glasses are tephritic in composition. They have degassed all their CO_2 and contain 520-1510 µg/g residual H_2O.

Degassing modelling. We model the theoretical composition of the exsolved fluid phase in equilibrium with the La Palma basanite using the C-S-O-H saturation model of Moretti et al., (2003). This model (publicly available for download at https://github.com/charlesll//chosetto) has been applied before to other volcanoes with widely different magma compositions (Aiuppa et al., 2010; Aiuppa et al., 2007; de Moor et al., 2016; Moretti et al., 2013; Moretti et al., 2018; Moretti and Papale, 2004; Oppenheimer et al., 2011; Papale et al., 2006). Model runs are initialized for a range of starting conditions and over a range of pressures and redox conditions relevant to La Palma basanites (**Extended Data Table 3)**. Details of all model runs are illustrated in **Extended Data Table 3**. Model runs are performed using as parental melt (major elements) a typical La Palma basanite. H_2O and S contents are from dissolved content in Cumbre Vieja melt inclusions (this study; **Extended Data Table 2**). CO_2 is assumed to vary from 1 to 5 wt.% in the different model runs to reproduce the postulated range for primary melts in the Canary(Longpre et al., 2017; Taracsak et al., 2019). All runs are performed by simulating isothermal (temperature kept constant at 1273 °K) magma decompression from an initial pressure of either 400 MPa (models (1) to (4)) or 5 MPa (models (5) to (9)) down to atmospheric conditions (0.1 MPa). Runs are performed in under closed system conditions (i.e., gas and melt continuously re-equilibrating during the decompression path) in runs (1) to (4) to simulate basanite ascent from source to shallow volcanic conduit. Runs (5) to (9) simulate the basanite degassing path in the shallow conduit, in which separated gas is allowed to freely escape from the melt (open system conditions). These models differ for the quantity (mass fraction) of gas removed at each pressure step, this "gas fraction lost" ranging from 0.1 (run (5)) to 0.9 (run (9)). In both closed and open system degassing, equilibrium compositions of the melt and the coexisting gas are calculated at each step throughout the decompression path. Redox conditions are fixed at 1 log units above the Nickel-Nickel Oxide (NNO) buffer (ΔNNO = +1) to fit the oxidized nature of the La Palma melt(Day et al., 2022) and intraplate alkaline melts in general(Taracsak et al., 2022) Run (4) uses slightly less oxidized redox conditions (ΔNNO = +0.5) to explore the effect of redox on the degassing path. Comparison between results obtained in runs (2) and (4) suggests a 0.5 log unit

change in redox has limited role in the degassing paths (Figure 2). In all model runs, the equilibrium exsolved gas varies during the degassing path from CO_2-rich at high pressure to H_2O-S-rich at low pressure (Figure 2). The pressure-dependent evolution of the modelled CO_2/S_T ratios is illustrated in **Extended Data Figure 3.** From this, we infer that the FV gas corresponds to the equilibrium gas at 1-3 MPa in runs (1) to (4), implying closed system degassing conditions likely prevailed until very shallow in the upper conduits. The largest CO_2 depletions are observed in open system and at low pressure, such conditions reproducing well the CO_2-poor compositions of EV gases (Figure 2 and **Extended Data Figure 3**). The modelled dissolved S contents (**Extended Data Figure 4**) also imply that S degassing from melt becomes significant only at very shallow levels (< 10 MPa). The predicted dissolved S content at atmospheric pressure (0.1 MPa) matches closely the mean groundmass glass S content of 474 ppm (**Extended Data Figure 4**).

SO_2 flux and plume height. TROPOMI data were analysed with the PlumeTraj approach(Burton et al., 2021; Hayer et al., 2023; Pardini et al., 2018; Pardini et al., 2019; Queisser et al., 2019), in which back-trajectory analysis is applied to determine the height at which gas would have needed to have been injected into the atmosphere above Cumbre Vieja to arrive at the observed pixel location. The height constraints then allow correction of the retrieved SO_2 masses. This is critical because the sensitivity of TROPOMI to SO_2 is strongly height dependent, meaning that without an accurate quantification of plume height SO_2 masses cannot be accurately quantified. Errors on the retrieved height and SO_2 mass are determined using the size of each pixel, the reported retrieved SO_2 mass error and the meteorological wind field error. Pixel heights and masses are then distributed in 10 minute time bins, combining uncertainties from each pixel's contribution to a time bin in quadrature. This produces a time series of SO_2 flux density, the distribution of SO_2 mass as a function of height and time. The initial motivation for retrieving plume height is to correct the retrieved SO_2 mass, but it is also an extremely valuable measurement, reflecting the evolution of the explosive mass eruption rate. The intense degassing during the first two weeks of the Cumbre Vieja eruption permitted the quantification of gas emissions emitted up to 36-48 hours prior to image collection, providing complete and continuous temporal coverage of the plume height and SO_2 emission rate. This was particularly valuable in the early stage of the eruption before ground-based measurements could be deployed.

Methods References

Aiuppa, A., Burton, M., Caltabiano, T., Giudice, G., Guerrieri, S., Liuzzo, M., Mure, F. and Salerno, G., 2010. Unusually large magmatic CO2 gas emissions prior to a basaltic paroxysm. Geophysical Research Letters, 37.

Aiuppa, A., Moretti, R., Federico, C., Giudice, G., Gurrieri, S., Liuzzo, M., Papale, P., Shinohara, H. and Valenza, M., 2007. Forecasting Etna eruptions by real-time observation of volcanic gas composition. Geology, 35(12): 1115-1118.

Allard, P., Burton, M., Sawyer, G. and Bani, P., 2016. Degassing dynamics of basaltic lava lake at a top-ranking volatile emitter: Ambrym volcano, Vanuatu arc. Earth and Planetary Science Letters, 448: 69-80.

Burton, M., Allard, P., Mure, F. and La Spina, A., 2007. Magmatic gas composition reveals the source depth of slug-driven Strombolian explosive activity. Science, 317(5835): 227-230.

764 Burton, M., Allard, P., Mure, F., Oppenheimer, C., Pyle, D. and Barclay, J., 2003. FTIR remote
765 sensing of fractional magma degassing at Mount Etna, Sicily. Volcanic Degassing, 213:
766 281-293.
767 Burton, M., Hayer, C., Miller, C. and Christenson, B., 2021. Insights into the 9 December 2019
768 eruption of Whakaari/White Island from analysis of TROPOMI SO2 imagery. Science
769 Advances, 7(25).
770 Day, J.M.D., Troll, V.R., Aulinas, M., Deegan, F.M., Geiger, H., Carracedo, J.C., Pinto, G.G. and
771 Perez-Torrado, F.J., 2022. Mantle source characteristics and magmatic processes
772 during the 2021 La Palma eruption. Earth and Planetary Science Letters, 597.
773 de Moor, J.M., Aiuppa, A., Pacheco, J., Avard, G., Kern, C., Liuzzo, M., Martínez, M., Giudice,
774 G. and Fischer, T.P., 2016. Short-period volcanic gas precursors to phreatic eruptions:
775 Insights from Poás Volcano, Costa Rica. Earth and Planetary Science Letters, 442: 218-
776 227.
777 Esse, B., Burton, M., Varnam, M., Kazahaya, R. and Salerno, G., 2020. iFit: A simple method
778 for measuring volcanic SO2 without a measured Fraunhofer reference spectrum. Journal
779 of Volcanology and Geothermal Research, 402.
780 Hayer, C., Burton, M., Ferrazzini, V., Esse, B. and Di Muro, A., 2023. Unusually high SO2
781 emissions and plume height from Piton de la Fournaise volcano during the April 2020
782 eruption. Bulletin of Volcanology, 85(4): 21.
783 La Spina, A., Burton, M., Allard, P., Alparone, S. and Mure, F., 2015. Open-path FTIR
784 spectroscopy of magma degassing processes during eight lava fountains on Mount
785 Etna. Earth and Planetary Science Letters, 413: 123-134.
786 La Spina, A., Burton, M.R., Harig, R., Mure, F., Rusch, P., Jordan, M. and Caltabiano, T., 2013.
787 New insights into volcanic processes at Stromboli from Cerberus, a remote-controlled
788 open-path FTIR scanner system. Journal of Volcanology and Geothermal Research,
789 249: 66-76.
790 Longpre, M.A., Stix, J., Klugel, A. and Shimizu, N., 2017. Mantle to surface degassing of
791 carbon- and sulphur-rich alkaline magma at El Hierro, Canary Islands. Earth and
792 Planetary Science Letters, 460: 268-280.
793 Moretti, R., Arienzo, I., Civetta, L., Orsi, G. and Papale, P., 2013. Multiple magma degassing
794 sources at an explosive volcano. Earth and Planetary Science Letters, 367: 95-104.
795 Moretti, R., Metrich, N., Arienzo, I., Di Renzo, V., Aiuppa, A. and Allard, P., 2018. Degassing vs.
796 eruptive styles at Mt. Etna volcano (Sicily, Italy). Part I: Volatile stocking, gas fluxing, and
797 the shift from low-energy to highly explosive basaltic eruptions. Chemical Geology, 482:
798 1-17.
799 Moretti, R. and Papale, P., 2004. On the oxidation state and volatile behavior in multicomponent
800 gas-melt equilibria. Chemical Geology, 213(1-3): 265-280.
801 Oppenheimer, C., Bani, P., Calkins, J.A., Burton, M.R. and Sawyer, G.M., 2006. Rapid FTIR
802 sensing of volcanic gases released by Strombolian explosions at Yasur volcano,
803 Vanuatu. Applied Physics B-Lasers and Optics, 85(2-3): 453-460.
804 Oppenheimer, C., Moretti, R., Kyle, P.R., Eschenbacher, A., Lowenstern, J.B., Hervig, R.L. and
805 Dunbar, N.W., 2011. Mantle to surface degassing of alkalic magmas at Erebus volcano,
806 Antarctica. Earth and Planetary Science Letters, 306(3-4): 261-271.
807 Papale, P., Moretti, R. and Barbato, D., 2006. The compositional dependence of the saturation
808 surface of H2O+CO2 fluids in silicate melts. Chemical Geology, 229(1-3): 78-95.
809 Pardini, F., Burton, M., Arzilli, F., La Spina, G. and Polacci, M., 2018. SO2 emissions, plume
810 heights and magmatic processes inferred from satellite data: The 2015 Calbuco
811 eruptions. Journal of Volcanology and Geothermal Research, 361: 12-24.
812 Pardini, F., Queisser, M., Naismith, A., Watson, I.M., Clarisse, L. and Burton, M.R., 2019. Initial
813 constraints on triggering mechanisms of the eruption of Fuego volcano (Guatemala)

from 3 June 2018 using IASI satellite data. Journal of Volcanology and Geothermal Research, 376: 54-61.

Pfeffer, M.A., Bergsson, B., Barsotti, S., Stefansdottir, G., Galle, B., Arellano, S., Conde, V., Donovan, A., Ilyinskaya, E., Burton, M., Aiuppa, A., Whitty, R.C.W., Simmons, I.C., Arason, P., Jonasdottir, E.B., Keller, N.S., Yeo, R.F., Arngrimsson, H., Johannsson, P., Butwin, M.K., Askew, R.A., Dumont, S., von Lowis, S., Ingvarsson, P., La Spina, A., Thomas, H., Prata, F., Grassa, F., Giudice, G., Stefansson, A., Marzano, F., Montopoli, M. and Mereu, L., 2018. Ground-Based Measurements of the 2014-2015 Holuhraun Volcanic Cloud (Iceland). Geosciences, 8(1).

Queisser, M., Burton, M., Theys, N., Pardini, F., Salerno, G., Caltabiano, T., Varnam, M., Esse, B. and Kazahaya, R., 2019. TROPOMI enables high resolution SO2 flux observations from Mt. Etna, Italy, and beyond. Scientific Reports, 9.

Tamburello, G., 2015. Ratiocalc: Software for processing data from multicomponent volcanic gas analyzers. Computers & Geosciences, 82: 63-67.

Taracsak, Z., Hartley, M.E., Burgess, R., Edmonds, M., Iddon, F. and Longpre, M.A., 2019. High fluxes of deep volatiles from ocean island volcanoes: Insights from El Hierro, Canary Islands. Geochimica Et Cosmochimica Acta, 258: 19-36.

Taracsak, Z., Longpre, M.A., Tartese, R., Burgess, R., Edmonds, M. and Hartley, M.E., 2022. Highly Oxidising Conditions in Volatile-Rich El Hierro Magmas: Implications for Ocean Island Magmatism. Journal of Petrology, 63(3).

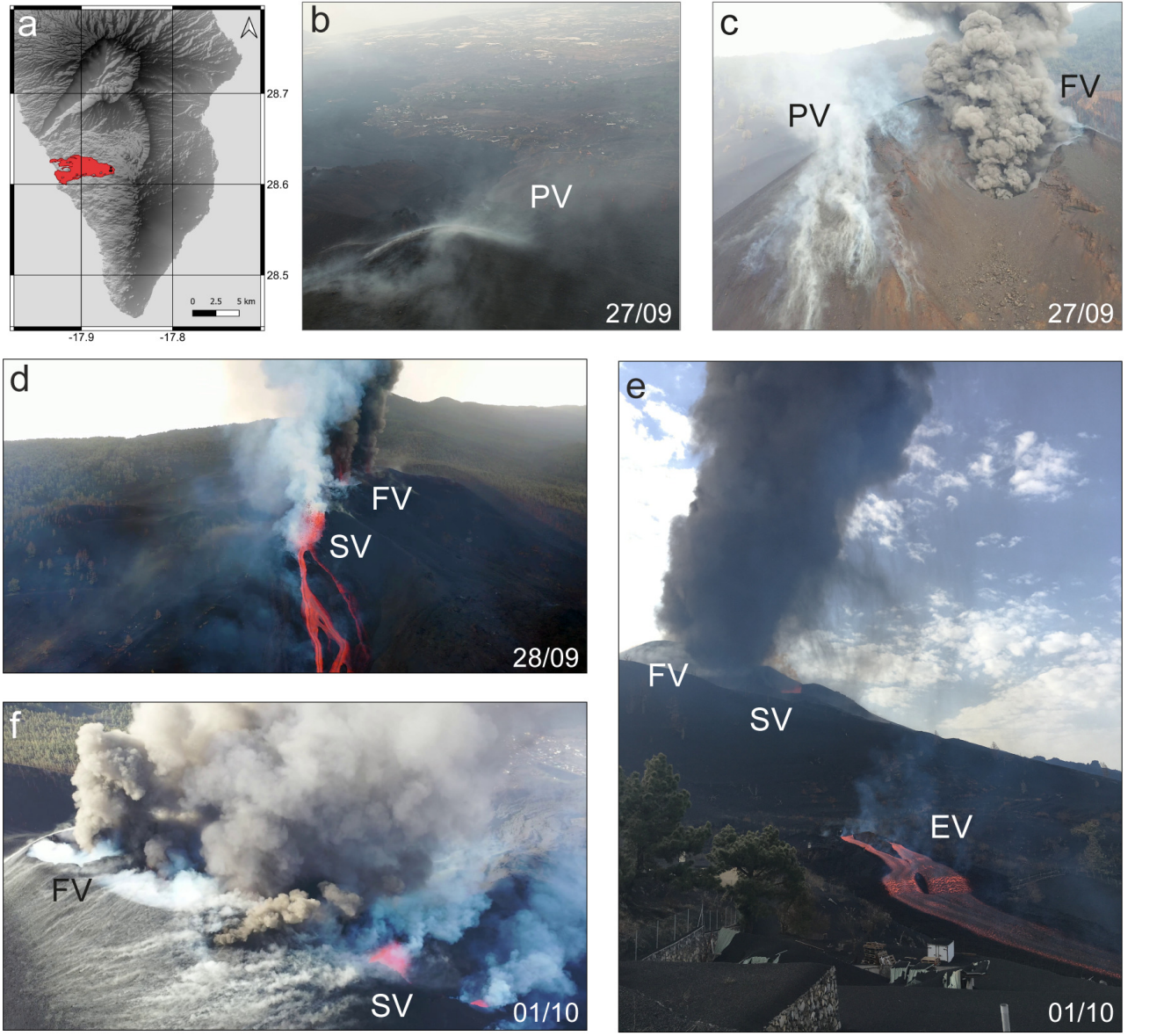
a
28.7
28.6
28.5
0 2.5 5 km
-17.9
-17.8
b
PV
27/09
c
PV
FV
27/09
d
FV
SV
28/09
e
FV
SV
EV
01/10
f
FV
SV
01/10

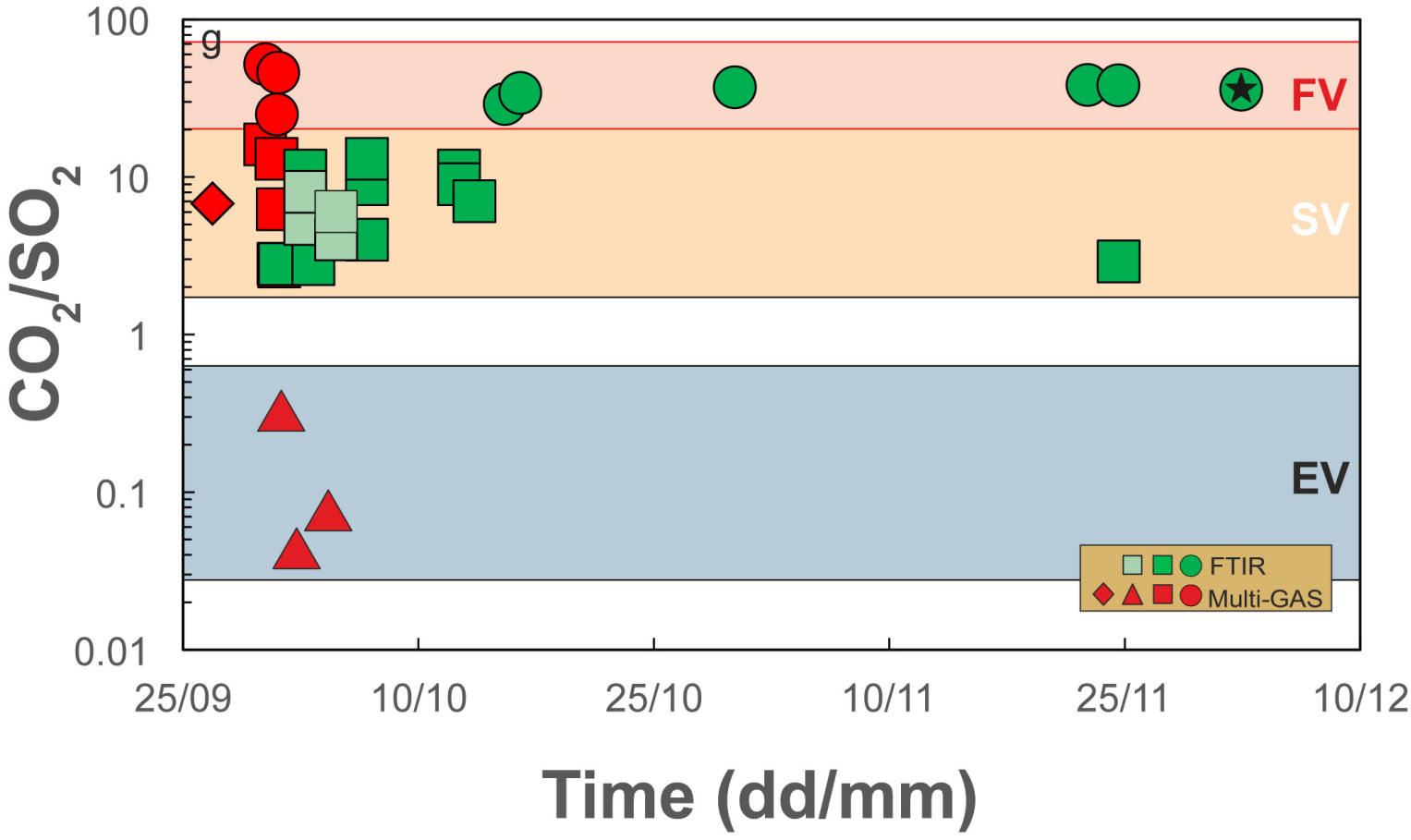
g
100
10
1
0.1
0.01
CO_2/SO_2
FV
SV
EV
FTIR
Multi-GAS
25/09
10/10
25/10
10/11
25/11
10/12
Time (dd/mm)

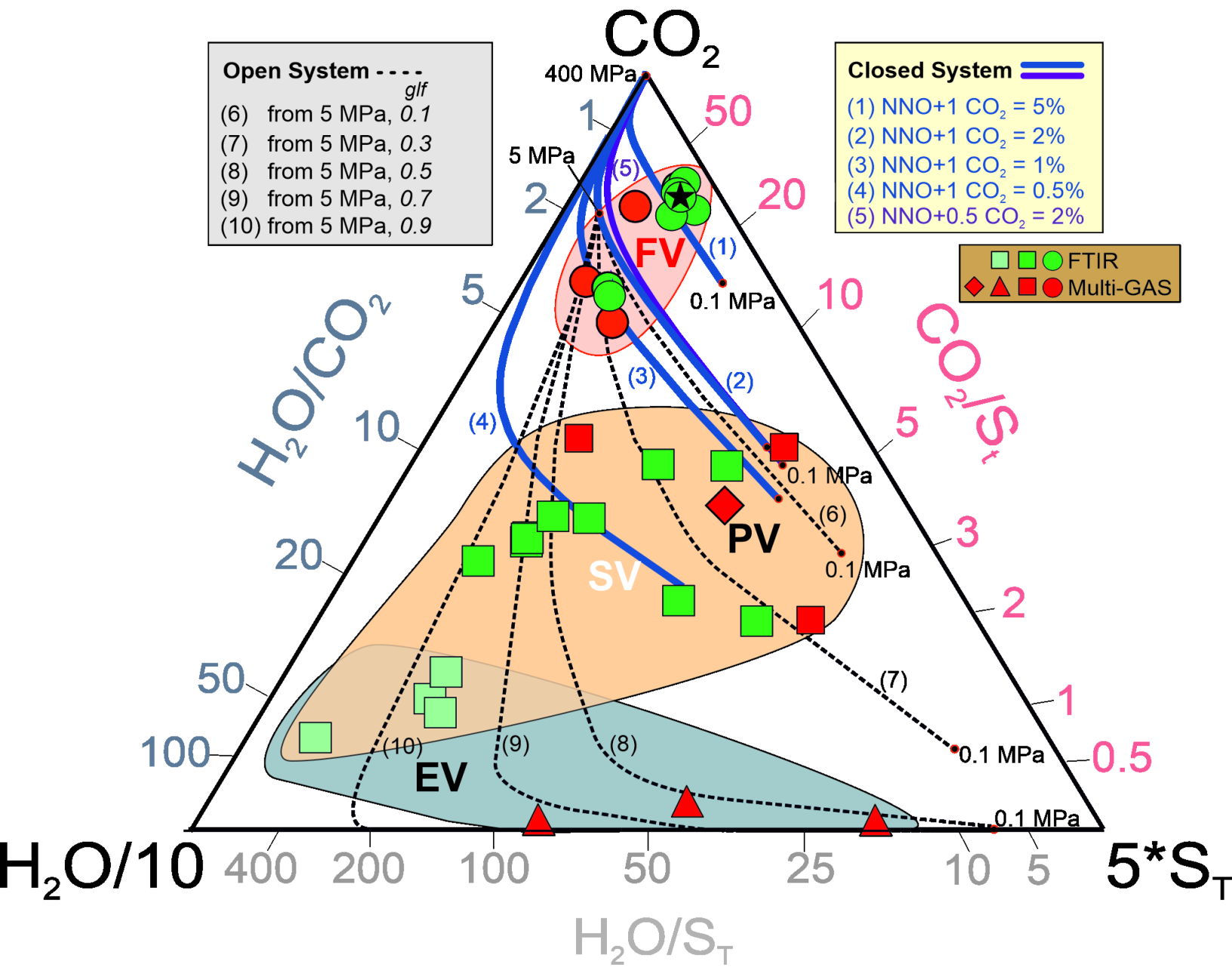
CO2
400 MPa
5 MPa
Open System - - - -
glf
(6) from 5 MPa, 0.1
(7) from 5 MPa, 0.3
(8) from 5 MPa, 0.5
(9) from 5 MPa, 0.7
(10) from 5 MPa, 0.9
Closed System
(1) NNO+1 CO2 = 5%
(2) NNO+1 CO2 = 2%
(3) NNO+1 CO2 = 1%
(4) NNO+1 CO2 = 0.5%
(5) NNO+0.5 CO2 = 2%
FTIR
Multi-GAS
FV
PV
SV
EV
0.1 MPa
H2O/CO2
CO2/St
H2O/10
H2O/ST
5*ST
1
2
5
10
20
50
100
400
200
100
50
25
10
5
3
0.5

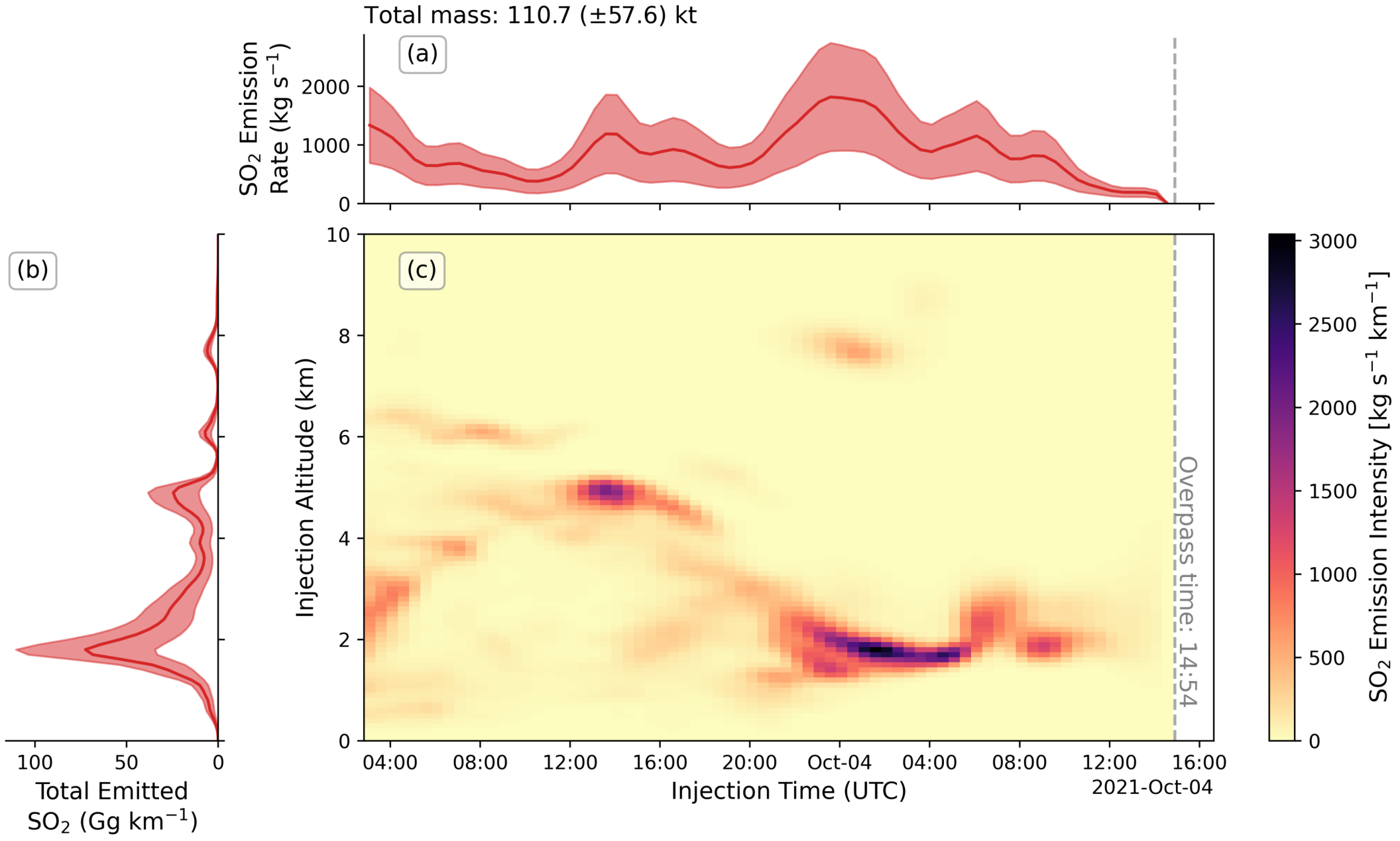
Total mass: 110.7 (±57.6) kt
(a)
SO2 Emission Rate (kg s−1)
2000
1000
0
(b)
100
50
0
Total Emitted SO2 (Gg km−1)
(c)
Injection Altitude (km)
10
8
6
4
2
0
04:00
08:00
12:00
16:00
20:00
Oct-04
04:00
08:00
12:00
16:00
Injection Time (UTC)
2021-Oct-04
Overpass time: 14:54
3000
2500
2000
1500
1000
500
0
SO2 Emission Intensity [kg s−1 km−1]

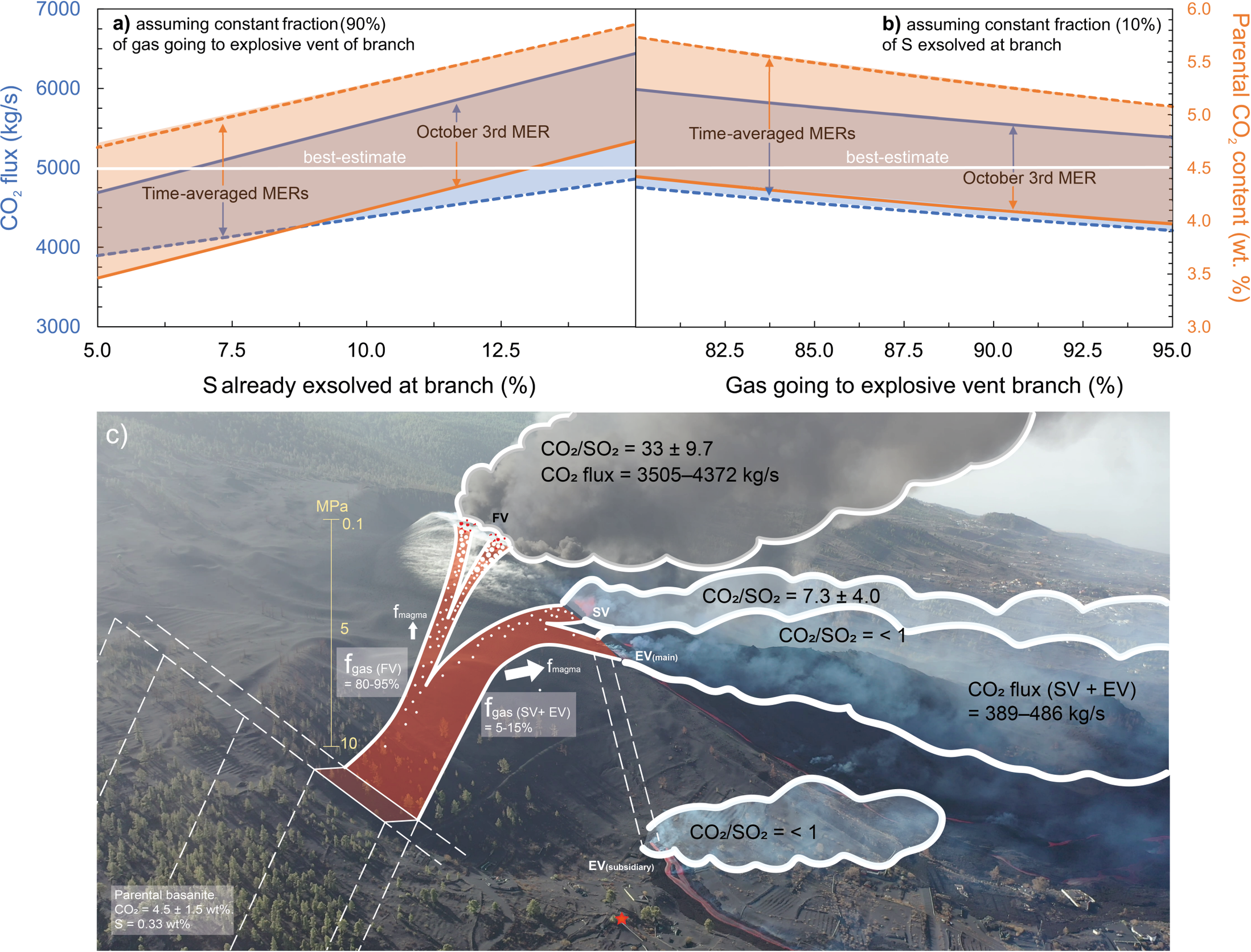
a) assuming constant fraction (90%) of gas going to explosive vent of branch
b) assuming constant fraction (10%) of S exsolved at branch
October 3rd MER
best-estimate
Time-averaged MERs
Time-averaged MERs
best-estimate
October 3rd MER
CO2 flux (kg/s)
Parental CO2 content (wt. %)
7000
6000
5000
4000
3000
6.0
5.5
5.0
4.5
4.0
3.5
3.0
5.0
7.5
10.0
12.5
82.5
85.0
87.5
90.0
92.5
95.0
S already exsolved at branch (%)
Gas going to explosive vent branch (%)
c)
CO2/SO2 = 33 ± 9.7
CO2 flux = 3505–4372 kg/s
MPa
0.1
5
10
FV
fmagma
fgas (FV) = 80-95%
SV
EV(main)
fmagma
fgas (SV+ EV) = 5-15%
CO2/SO2 = 7.3 ± 4.0
CO2/SO2 = < 1
CO2 flux (SV + EV) = 389–486 kg/s
CO2/SO2 = < 1
EV(subsidiary)
Parental basanite
CO2 = 4.5 ± 1.5 wt%
S = 0.33 wt%

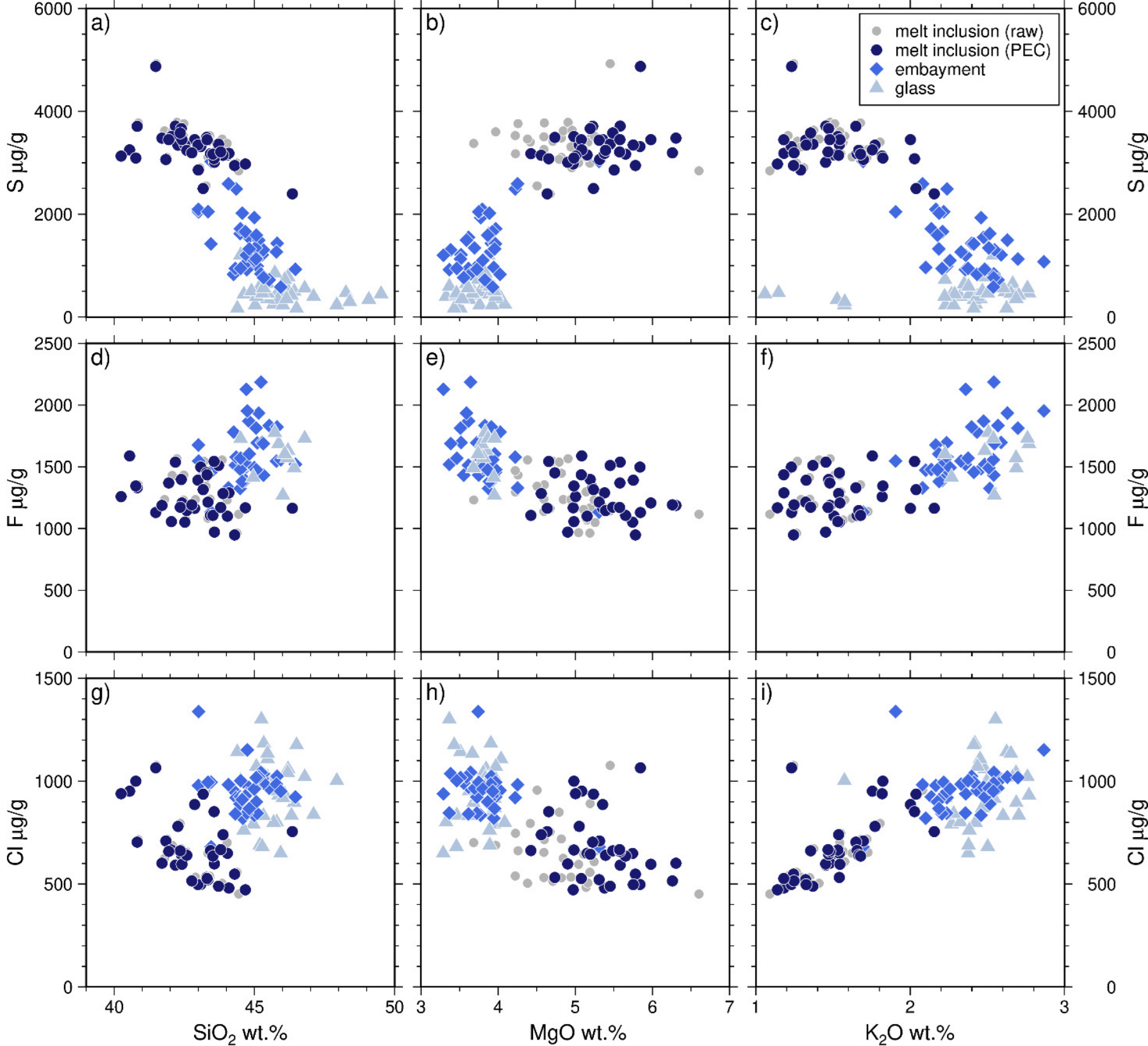
a)
b)
c)
d)
e)
f)
g)
h)
i)
melt inclusion (raw)
melt inclusion (PEC)
embayment
glass
S µg/g
F µg/g
Cl µg/g
SiO2 wt.%
MgO wt.%
K2O wt.%
0
2000
4000
6000
500
1000
1500
2500
40
45
50
3
4
5
6
7
1
2
3

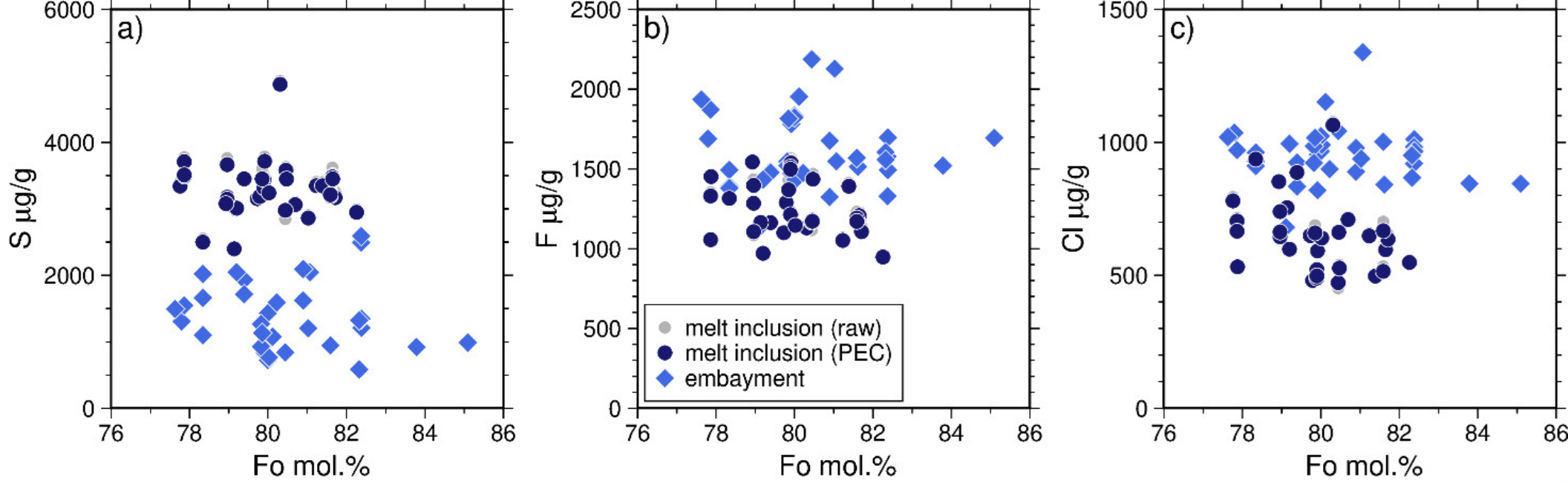
a)
b)
c)
S µg/g
F µg/g
Cl µg/g
Fo mol.%
melt inclusion (raw)
melt inclusion (PEC)
embayment

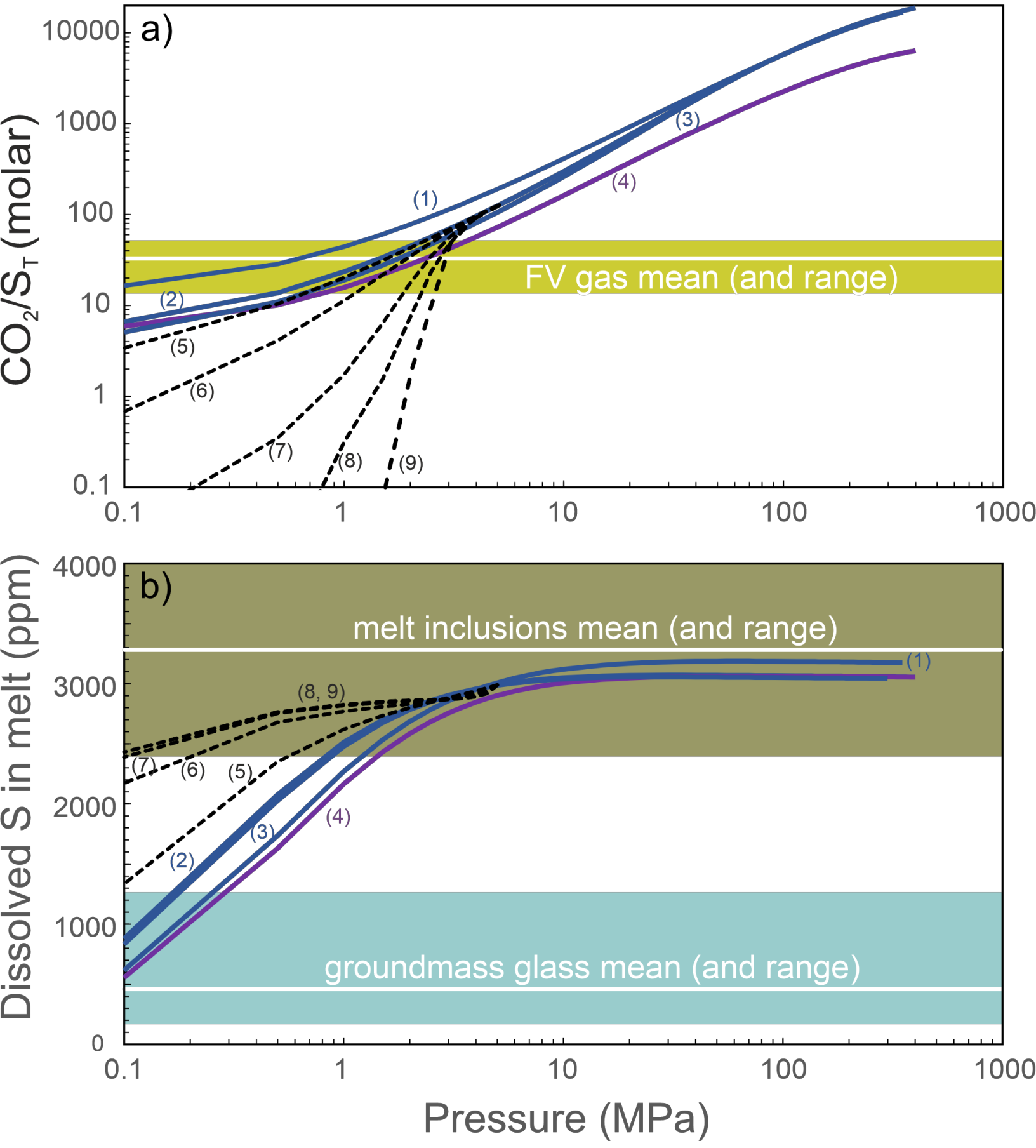
a)
10000
1000
100
10
1
0.1
CO_2/S_T (molar)
(1)
(2)
(3)
(4)
(5)
(6)
(7)
(8)
(9)
FV gas mean (and range)
0.1
1
10
100
1000
b)
4000
3000
2000
1000
0
Dissolved S in melt (ppm)
melt inclusions mean (and range)
(8, 9)
(7)
(6)
(5)
(4)
(3)
(2)
(1)
groundmass glass mean (and range)
0.1
1
10
100
1000
Pressure (MPa)

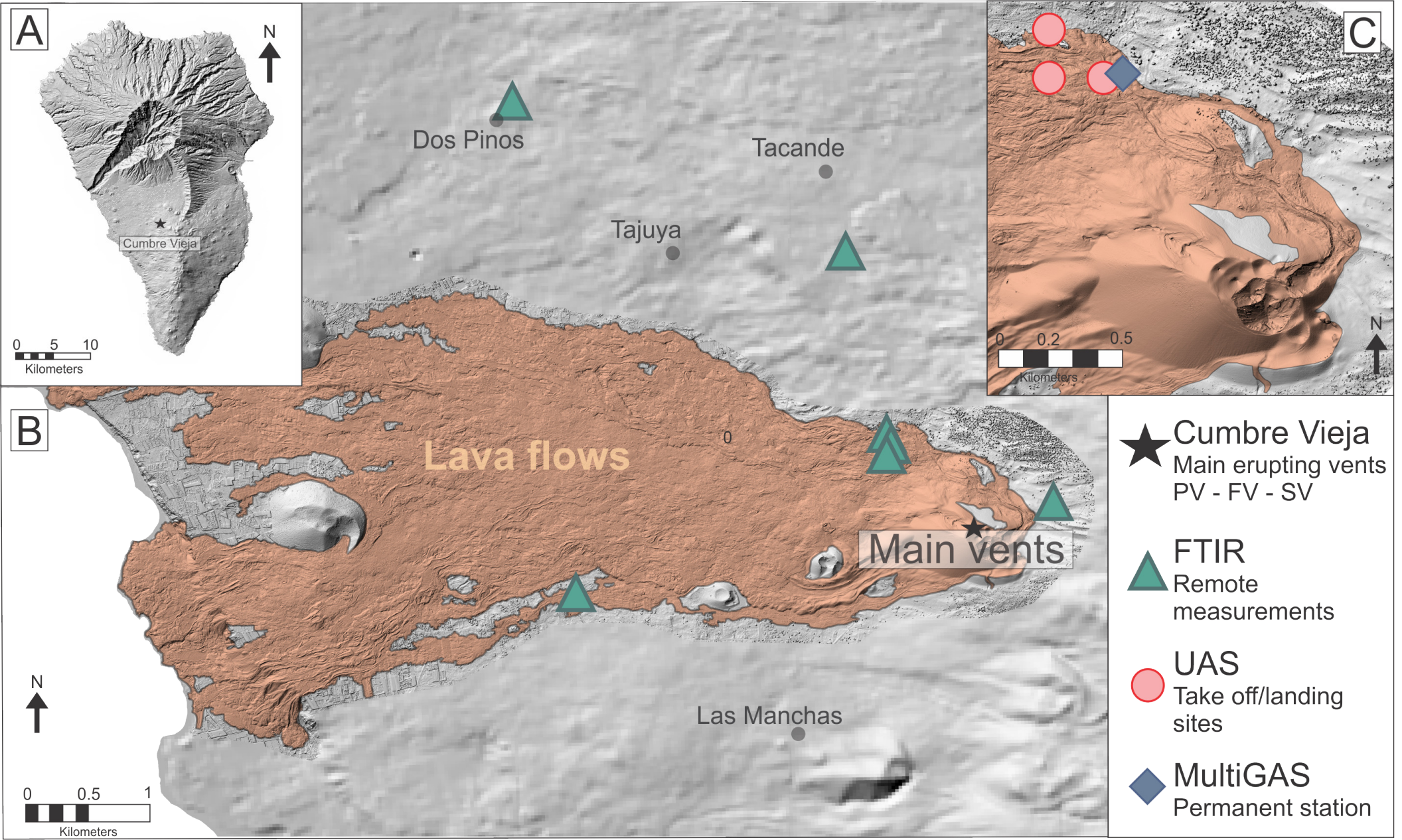
A
N
Cumbre Vieja
0 5 10
Kilometers
Dos Pinos
Tacande
Tajuya
B
Lava flows
Main vents
Las Manchas
N
0 0.5 1
Kilometers
C
0 0.2 0.5
Kilometers
N
Cumbre Vieja
Main erupting vents
PV - FV - SV
FTIR
Remote measurements
UAS
Take off/landing sites
MultiGAS
Permanent station

Method	Date	Time UTC	Measurement Site
Multi-GAS	10/1/2021	10:00	Gas composition measured by aerial multigas from lateral vent on northern flank
Multi-GAS	10/2/2021	11:30	Gas composition measured by aerial multigas from lateral vent on northern flank
Multi-GAS	10/4/2021	11:15	Gas composition measured by aerial multigas above the upper effusive vent
Multi-GAS	9/30/2021	9:00	Gas composition measured by ground-based portable multi-gas in the downwind grounding plume of the lava fountaining, taken about ~900m from the main cone.
Multi-GAS	10/1/2021	2:00	Gas composition measured by ground-based fixed multi-gas in the downwind grounding plume of the lava fountaining, taken about ~900m from the main cone.
Multi-GAS	10/1/2021	5:00	Gas composition measured by ground-based fixed multi-gas in the downwind grounding plume of the lava fountaining, taken about ~900m from the main cone
Multi-GAS	9/27/2021	16:30	Gas composition measured by aerial multigas above the rim of the main cone. The measurements were acquired during a period of eruptive quiescence before explosive activity resumed approximately 30 minutes later.
Multi-GAS	9/30/2021	9:00	Gas composition measured by ground-based fixed multi-gas in the downwind grounding plume of the spattering vent taken about ~900m from the main cone
Multi-GAS	10/1/2021	2:00	Gas composition measured by ground-based fixed multi-gas in the downwind grounding plume of the spattering vent taken about ~900m from the main cone
Multi-GAS	10/1/2021	5:00	Gas composition measured by ground-based fixed multi-gas in the downwind grounding plume of the spattering vent taken about ~900m from the main cone
Multi-GAS	10/1/2021	6:00	Gas composition measured by ground-based fixed multi-gas in the downwind grounding plume of the spattering vent taken about ~900m from the main cone
Multi-GAS	10/1/2021	7:00	Gas composition measured by ground-based fixed multi-gas in the downwind grounding plume of the spattering vent taken about ~900m from the main cone
Multi-GAS	10/1/2021	8:00	Gas composition measured by ground-based fixed multi-gas in the downwind grounding plume of the spattering vent taken about ~900m from the main cone
Multi-GAS	10/3/2021	11:00	Gas composition measured by aerial multi-gas in the plume from the spattering vent on the northern flank.
OP-FTIR	10/3/2021	14:21	Tacande house 28.635N, 17.877W
OP-FTIR	10/3/2021	15:12	Tacande house 28.635N, 17.877W
OP-FTIR	10/3/2021	15:39	Tacande house 28.635N, 17.877W
OP-FTIR	10/3/2021	16:15	Tacande house 28.635N, 17.877W
OP-FTIR	10/3/2021	16:25	Tacande house 28.635N, 17.877W

OP-FTIR	10/16/2021		Tajuya
OP-FTIR	10/17/2021		Paraiso
OP-FTIR	10/31/2021		Las Manchas 28.610N, 17.896W
OP-FTIR	11/6/2021	21:00	Dos Pinos Involcan Base 28.646N, 17.901W
OP-FTIR	11/23/2021		Base
OP-FTIR	11/25/2021		Tacande
OP-FTIR	12/2/2021	18:25	Cabeza de Vaca 2 28.617N, 17.862W
OP-FTIR	12/3/2021		Cabeza de Vaca 2 28.617N, 17.862W
OP-FTIR	10/3/2021	14:30	Tacande flow 28.622N, 17.874W
OP-FTIR	10/3/2021		Tacande_middleVent_INGV
OP-FTIR	10/3/2021		Tacande spattering_INGV
OP-FTIR	10/3/2021		Villa UK
OP-FTIR	10/5/2021		Tacande
OP-FTIR	10/5/2021		Tacande 4coadds
OP-FTIR	10/7/2021		Tajuya mid_vent
OP-FTIR	10/7/2021		Tajuya low vent
OP-FTIR	10/7/2021		Tajuya
OP-FTIR	10/13/2021		Tacande
OP-FTIR	10/13/2021		Tajuya rotonda
OP-FTIR	10/14/2021		Tacande
OP-FTIR	11/25/2021		base lava fountain
OP-FTIR	12/4/2021	19:30	Las Manchas 28.610N, 17.896W
OP-FTIR	12/5/2021	13:30	Las Manchas 28.610N, 17.896W

Vent Type	activity type	CO_2/SO_2	H_2O/SO_2
EV	lateral effusive vent	0.3	41.9
EV	lateral effusive vent	0.04	16.7
EV	main effusive vent	0.07	82
FV	lava fountaining	52	71
FV	lava fountaining	25	80
FV	lava fountaining	46	141
PV	quiescently degassing vent	6.8	33.4
SV	spattering vent	16	95
SV	spattering vent	13	
SV	spattering vent	6.2	13
SV	spattering vent	2.8	
SV	spattering vent	2.7	
SV	spattering vent	2.8	
SV	spattering vent	2.8	17.9
FV	main ash column	16.3	
FV	main ash column	14.1	
FV	main ash column	24.1	
FV	main ash column	33.6	
FV	main ash column	30.3	

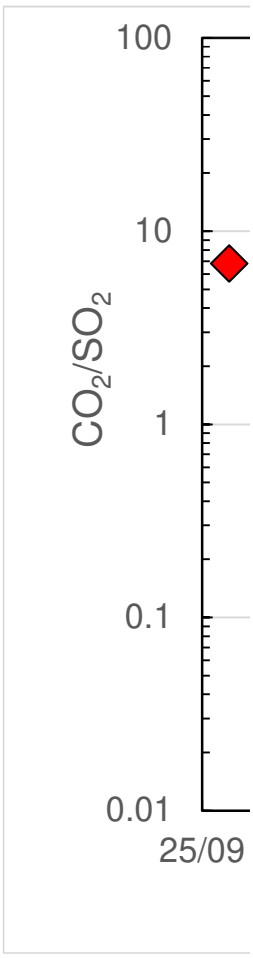

FV	base of lava fountain	29	16
FV	base of lava fountain	34	31
FV	base of lava fountain	37	22.3
FV	vigorous strombolian activity at main vent	33.5	92.2
FV	base of lava fountain	38.3	17
FV	base of lava fountain	38	24
FV	lava fountaining at NE vent	35.8	22.4
FV	base of lava fountain	35.8	22.4
SV	spattering vent	10.8	126
SV	spattering vent	5	186
SV	spattering vent	11	126
SV	spattering vent	8	518
SV	spattering vent	4	166
SV	spattering vent	6	176
SV	spattering of vent of lava flow	4	42
SV	spattering of vent of lava flow	9	79
SV	spattering vent	13	186
SV	spattering vent	11	106
SV	spattering vent	9	47
SV	spattering vent	7	26
SV	base of lava fountain	2.9	26
SV	spattering of vent of lava flow	9.3	
SV	vent of lava flow	5.3	36

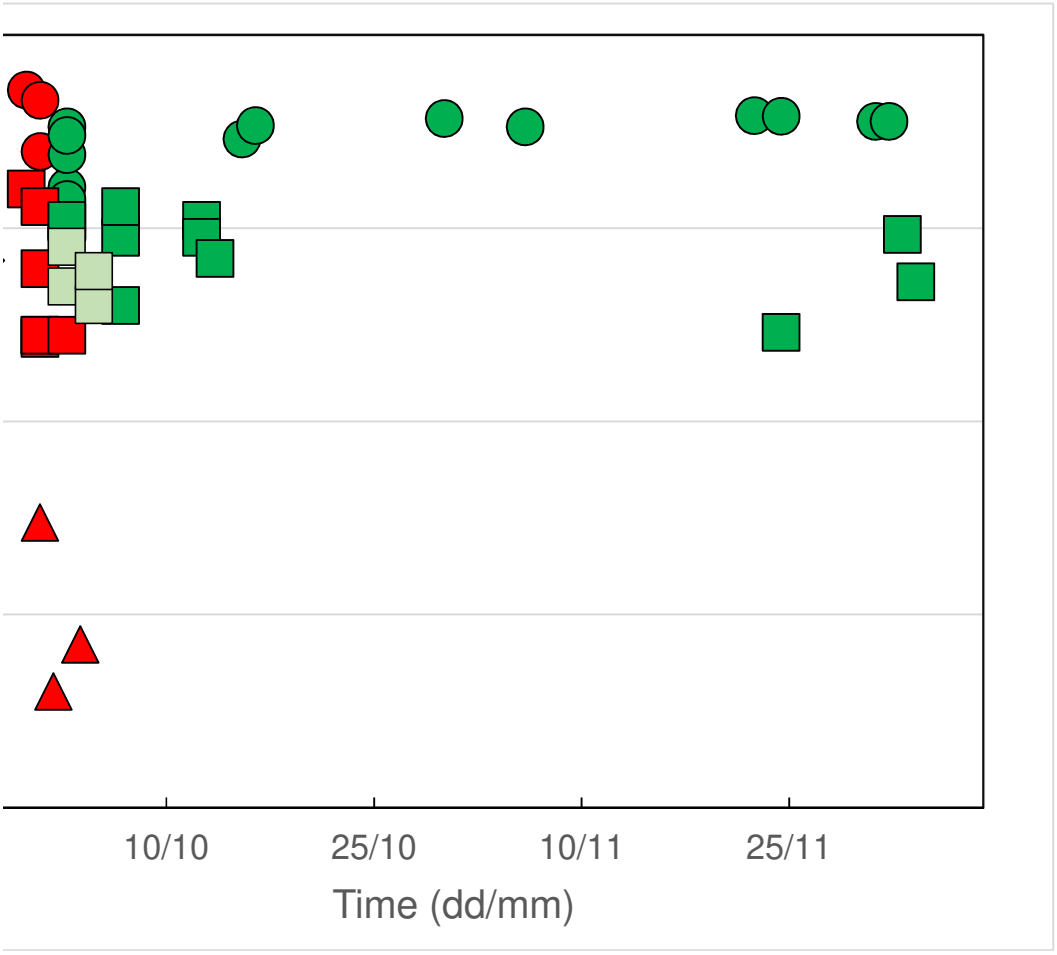
10/10
25/10
10/11
25/11
Time (dd/mm)

	SAMPLE	crystal-inclusion	type	lab	SiO2_mea wt.%	TiO2_mea wt.%	Al2O3_me wt.%	FeO_meas wt.%
					uncorrected EPMA data			
1	CAN-TLP-0037	ol3-mi1	mi	LMV	41.88	4.24	15.52	9.51
2	CAN-TLP-0040	ol4-mi1	mi	LMV	43.06	4.08	15.49	9.58
3	CAN-TLP-0052	ol2-mi1	mi	LMV	42.35	3.71	15.31	10.64
4	CAN-TLP-0042	ol3-mi1	mi	UoB	44.12	3.82	15.03	10.31
5	CAN-TLP-0042	ol8-mi1	mi	UoB	43.85	3.91	15.40	10.22
6	CAN-TLP-0042	ol8-mi2	mi	UoB	43.42	3.89	15.38	10.01
7	CAN-TLP-0042	ol8-mi3	mi	UoB	43.20	4.20	14.85	10.86
8	CAN-TLP-0042	ol12-mi1	mi	UoB	42.23	4.55	14.75	10.52
9	CAN-TLP-0042	ol22-mi2	mi	UoB	44.04	3.65	14.52	10.05
10	CAN-TLP-0042	o29-mi2	mi	UoB	42.88	3.43	14.67	10.50
11	CAN-TLP-0168	ol53-mi2	mi	UoB	41.50	4.04	14.83	10.90
12	CAN-TLP-0168	ol66-mi1	mi	UoB	46.35	2.76	16.23	9.61
13	CAN-TLP-0168	ol67-mi1	mi	UoB	44.38	3.79	14.51	9.56
14	M8-A	ol35-mi1	mi	UoB	43.28	3.96	14.96	10.21
15	M8-A	ol41-mi1	mi	UoB	42.57	4.23	14.51	9.97
16	M8-A	ol45-mi1	mi	UoB	41.80	4.21	14.66	10.37
17	M8-A	ol62-mi1	mi	UoB	44.44	3.23	15.25	9.86
18	M8-A	ol69-mi1	mi	UoB	42.48	4.19	14.94	10.30
19	M8-A	ol69-mi2	mi	UoB	43.34	3.61	15.00	9.38
20	M8-A	ol69-mi3	mi	UoB	43.92	3.67	14.77	9.31
21	M8-A	ol75-mi1	mi	UoB	43.04	4.32	15.30	9.86
22	M8-A	ol76-mi1	mi	UoB	42.47	4.20	14.37	9.95
23	M8-A	ol90a-mi1	mi	UoB	43.55	3.49	16.82	9.55
24	M8-A	ol102-mi1	mi	UoB	40.86	3.99	14.67	10.74
25	M8-A	ol102-mi1	mi	UoB	42.01	4.05	14.55	10.83
26	M8-A	ol109-mi1	mi	UoB	43.55	3.37	15.63	9.95
27	M8-C	ol4-mi1	mi	UoB	42.40	3.91	14.77	9.93
28	M8-C	ol7-mi2	mi	UoB	42.07	4.39	15.02	10.21
29	M8-C	ol13-mi1	mi	UoB	42.62	4.01	14.74	10.23
30	M8-C	ol30-mi1	mi	UoB	43.64	3.66	15.92	9.60
31	M8-C	ol39-mi1	mi	UoB	43.27	3.62	15.54	11.01
32	M8-D	ol41-mi1	mi	UoB	42.90	4.33	14.81	10.40
33	M8-D	ol41-mi2	mi	UoB	44.03	3.37	15.65	9.23
34	M8-D	ol44-mi1	mi	UoB	43.40	3.78	15.78	9.23
35	M8-C	ap94-mi1	mi	UoB	40.55	3.60	14.52	11.81
36	M8-C	ap94-mi2	mi	UoB	40.25	3.55	14.50	11.73
37	M8-C	ap94-mi3	mi	UoB	40.77	3.59	14.48	11.97
38	CAN-TLP-0042	ol1-emb1	emb	UoB	44.26	3.98	15.83	11.70
39	CAN-TLP-0042	ol12-emb2	emb	UoB	44.59	3.88	15.52	11.65
40	CAN-TLP-0042	ol29-emb1	emb	UoB	44.50	3.77	16.10	11.40
41	CAN-TLP-0042	ol30-emb2	emb	UoB	44.99	2.46	16.80	9.80
42	CAN-TLP-0168	ol5-emb1	emb	UoB	44.73	3.76	16.24	11.48
43	CAN-TLP-0168	ol8-emb1	emb	UoB	44.71	3.50	16.30	11.92
44	CAN-TLP-0168	ol13-emb1	emb	UoB	45.10	3.84	15.98	12.16
45	CAN-TLP-0168	ol50-emb1	emb	UoB	43.01	4.08	17.15	9.96

46	CAN-TLP-0168	ol72-emb2	emb	UoB	44.32	4.10	16.08	12.03
47	M8-A	ol19-emb1	emb	UoB	45.78	3.25	16.82	9.99
48	M8-A	ol19-emb2	emb	UoB	46.46	3.32	16.95	9.54
49	M8-A	ol47-emb1	emb	UoB	45.03	3.50	16.74	10.34
50	M8-A	ol47-emb2	emb	UoB	45.28	3.31	16.86	10.40
51	M8-A	ol57-emb1	emb	UoB	45.31	3.81	16.38	11.13
52	M8-A	ol62-emb1b	emb	UoB	45.23	3.32	16.50	10.63
53	M8-A	ol65-emb1	emb	UoB	45.52	3.80	15.93	10.94
54	M8-A	ol66-emb1	emb	UoB	43.46	3.89	14.70	9.80
55	M8-A	ol102-emb3	emb	UoB	44.80	3.40	16.85	11.01
56	M8-A	ol109-emb1	emb	UoB	43.35	3.59	16.00	11.85
57	M8-A	ol123-emb1	emb	UoB	44.35	3.31	16.23	10.73
58	M8-A	ol123-emb2	emb	UoB	44.07	3.54	16.17	10.66
59	M8-C	ol7-emb1	emb	UoB	45.06	3.46	16.43	10.67
60	M8-C	ol13-emb2	emb	UoB	45.32	3.56	15.99	10.80
61	M8-C	ol39-emb1-inner	emb	UoB	44.56	3.32	16.22	10.45
62	M8-C	ol39-emb1-mid	emb	UoB	44.68	3.34	16.57	10.12
63	M8-C	ol39-emb1-outer	emb	UoB	45.00	3.54	16.54	9.83
64	M8-C	ol43-emb1	emb	UoB	43.00	3.66	16.14	11.49
65	M8-C	ol43-emb3	emb	UoB	44.49	3.62	16.27	10.26
66	M8-C	ol85-emb1	emb	UoB	45.15	3.61	16.87	11.14
67	M8-D	ol18-emb1	emb	UoB	45.81	3.58	16.96	10.87
68	M8-D	ol41-emb1	emb	UoB	44.51	3.89	15.76	11.12
69	M8-D	ol47-emb1	emb	UoB	45.07	3.46	16.72	11.17
70	M8-D	ol71-emb1-inner	emb	UoB	44.81	3.81	16.39	11.07
71	M8-D	ol71-emb1-outer	emb	UoB	45.94	3.81	16.28	10.76
72	M8-D	ol91-emb1	emb	UoB	44.74	4.03	17.61	10.42
73	M8-C	ap94-emb1	emb	UoB	43.45	3.63	15.50	11.19
74	CAN-TLP-0042	ol10-gl1	gl	UoB	46.42	3.67	15.93	10.93
75	CAN-TLP-0042	ol15-gl1	gl	UoB	46.02	3.58	16.43	10.46
76	CAN-TLP-0168	ol37-gl1	gl	UoB	44.96	3.91	15.42	11.82
77	M8-A	ol25-gl1	gl	UoB	46.20	3.57	16.44	10.11
78	M8-A	ol65-gl1	gl	UoB	45.86	3.68	16.30	10.54
79	M8-A	ol71-gl1	gl	UoB	46.18	3.59	16.29	10.29
80	M8-A	ol91-gl1	gl	UoB	46.08	3.23	16.79	9.36
81	M8-C	ol39-gl1	gl	UoB	45.73	3.51	16.48	10.16
82	M8-C	ap94-gl1	gl	UoB	44.51	3.79	15.47	10.60
83	M8-D	ol18-gl1	gl	UoB	46.79	3.83	16.24	10.68
84	LPA-16	shard1-gl1	gl	LMV	48.55	1.95	23.21	5.55
85	LPA-16	shard1-gl2	gl	LMV	45.80	3.31	17.76	9.94
86	LPA-16	shard1-gl3	gl	LMV	45.68	3.81	15.65	10.61
87	LPA-16	shard1-gl4	gl	LMV	45.18	3.78	16.05	11.16
88	LPA-16	shard1-gl5	gl	LMV	44.39	3.89	15.76	11.53
89	LPA-16	shard1-gl6	gl	LMV	49.08	2.10	22.56	6.19
90	LPA-16	shard1-gl7	gl	LMV	45.83	3.76	15.76	10.92
91	LPA-16	shard1-gl8	gl	LMV	45.93	3.82	16.35	11.07
92	LPA-16	shard1-gl9	gl	LMV	45.25	3.83	15.89	10.75
93	LPA-16	shard1-gl10	gl	LMV	45.43	3.88	16.12	11.34

94	LPA-16	shard1-gl11	gl	LMV	45.12	3.91	16.11	11.23
95	CAN-TLP-0128	shard1-gl1	gl	LMV	48.26	2.16	23.48	6.21
96	CAN-TLP-0128	shard1-gl2	gl	LMV	47.94	2.65	21.56	7.20
97	CAN-TLP-0128	shard1-gl3	gl	LMV	45.37	3.91	15.94	11.54
98	CAN-TLP-0128	shard1-gl4	gl	LMV	45.84	3.91	16.25	11.36
99	CAN-TLP-0128	shard1-gl5	gl	LMV	44.62	3.99	15.92	11.55
100	CAN-TLP-0128	shard2-gl1	gl	LMV	45.47	4.00	16.15	12.31
101	CAN-TLP-0128	shard2-gl2	gl	LMV	45.33	3.88	16.19	11.54
102	CAN-TLP-0128	shard2-gl3	gl	LMV	46.01	3.71	16.92	11.33
103	CAN-TLP-0128	shard2-gl4	gl	LMV	49.30	1.35	25.40	5.34
104	CAN-TLP-0128	shard2-gl5	gl	LMV	49.51	1.96	25.69	6.45
105	CAN-TLP-0128	shard3-gl1	gl	LMV	45.03	3.93	16.03	11.35
106	CAN-TLP-0128	shard3-gl2	gl	LMV	45.34	3.94	15.91	11.66
107	CAN-TLP-0128	shard3-gl3	gl	LMV	45.14	3.96	15.79	12.19
108	CAN-TLP-0128	shard3-gl4	gl	LMV	45.07	3.95	16.10	11.99
109	CAN-TLP-0128	shard3-gl5	gl	LMV	45.19	3.97	16.15	11.86
110	CAN-TLP-0053	shard1-gl1	gl	LMV	45.47	3.77	16.45	11.02
111	CAN-TLP-0053	shard1-gl2	gl	LMV	46.50	3.42	17.42	9.97
112	CAN-TLP-0053	shard1-gl3	gl	LMV	48.40	2.61	20.37	7.85
113	CAN-TLP-0053	shard1-gl4	gl	LMV	44.89	3.76	15.73	11.11
114	CAN-TLP-0053	shard1-gl5	gl	LMV	46.32	3.68	16.36	11.36
115	CAN-TLP-0053	shard1-gl6	gl	LMV	45.47	3.86	15.84	11.18
116	CAN-TLP-0053	shard1-gl7	gl	LMV	45.28	3.79	16.17	11.26
117	CAN-TLP-0053	shard1-gl8	gl	LMV	46.14	3.71	16.22	11.15
118	CAN-TLP-0053	shard1-gl9	gl	LMV	45.32	3.83	16.24	11.21
119	CAN-TLP-0053	shard1-gl10	gl	LMV	47.11	3.12	19.13	9.37

MnO_mea wt.%	MgO_mea wt.%	CaO_meas wt.%	Na2O_me wt.%	K2O_meas wt.%	P2O5_mea wt.%	Cr2O3_me wt.%	H2O_meas wt.%	CO2-wt_m wt.%	SO3_meas wt.%
0.18	4.82	11.82	4.18	1.72	0.96	nm	1.30	0.22	0.31
0.18	4.95	11.38	4.25	1.31	1.00	nm	2.21	0.51	0.29
0.15	4.42	10.38	4.63	1.80	1.34	nm	1.48	0.23	0.34
0.17	5.14	11.41	4.35	1.19	0.66	0.01	nm	nm	0.80
0.17	4.38	12.21	4.19	1.41	0.95	0.01	nm	nm	0.87
0.16	4.59	12.28	4.12	1.35	0.92	bdl	nm	nm	0.88
0.16	4.71	12.08	4.07	1.27	0.95	bdl	nm	nm	0.85
0.17	4.91	12.09	4.17	1.48	0.98	0.00	nm	nm	0.95
0.16	5.13	12.22	3.87	1.51	0.87	0.05	nm	nm	0.79
0.17	5.19	10.71	4.21	2.01	1.83	bdl	nm	nm	0.87
0.17	5.45	12.26	4.30	1.24	1.87	0.01	nm	nm	1.23
0.18	4.67	10.00	5.18	2.15	0.86	0.08	nm	nm	0.60
0.14	5.19	13.73	3.63	1.26	0.84	0.03	nm	nm	0.75
0.18	4.82	10.71	4.46	1.54	0.91	bdl	nm	nm	0.87
0.15	5.15	12.79	3.69	1.57	0.90	0.01	nm	nm	0.85
0.18	4.84	12.67	3.80	1.54	0.92	0.00	nm	nm	0.90
0.18	6.60	11.80	3.95	1.09	0.71	0.16	nm	nm	0.71
0.17	4.26	12.79	4.02	1.51	0.98	bdl	nm	nm	0.94
0.14	5.14	12.59	3.87	1.62	0.88	0.10	nm	nm	0.78
0.15	4.22	13.18	3.97	1.55	0.88	0.02	nm	nm	0.79
0.17	5.16	11.89	4.04	1.35	0.91	bdl	nm	nm	0.85
0.17	5.24	12.39	3.58	1.58	0.93	0.02	nm	nm	0.88
0.16	4.79	9.44	4.97	2.02	1.49	0.01	nm	nm	0.77
0.20	4.60	10.94	4.19	1.68	0.99	0.01	nm	nm	0.94
0.19	5.26	12.00	3.81	1.52	0.94	0.00	nm	nm	0.87
0.15	5.04	12.80	3.64	1.45	0.82	0.88	nm	nm	0.75
0.15	4.96	11.97	4.24	1.37	0.87	0.01	nm	nm	0.91
0.17	3.97	12.66	4.02	1.54	0.93	0.03	nm	nm	0.90
0.16	5.11	12.37	3.92	1.68	0.94	bdl	nm	nm	0.82
0.16	4.59	13.13	4.04	1.73	0.91	0.03	nm	nm	0.81
0.23	4.50	10.19	5.47	2.08	1.13	0.01	nm	nm	0.64
0.16	4.94	12.16	4.02	1.29	0.95	0.01	nm	nm	0.83
0.14	3.68	13.37	4.15	1.54	0.92	0.06	nm	nm	0.84
0.15	4.22	12.99	4.16	1.21	0.93	0.02	nm	nm	0.88
0.26	5.08	12.12	5.25	1.75	2.08	bdl	nm	nm	0.81
0.26	5.00	11.75	5.07	1.82	2.00	0.02	nm	nm	0.78
0.24	4.98	11.95	5.07	1.82	2.00	bdl	nm	nm	0.77
0.20	4.02	10.30	5.59	2.43	1.45	0.00	nm	nm	0.21
0.21	3.94	10.42	5.23	2.10	1.06	0.01	nm	nm	0.24
0.23	3.97	10.07	5.24	2.14	1.04	0.00	nm	nm	0.43
0.17	3.77	10.77	6.26	2.46	0.95	0.03	nm	nm	0.48
0.20	3.37	9.96	5.53	2.36	1.07	0.00	nm	nm	0.23
0.21	3.29	10.11	5.19	2.36	1.11	0.00	nm	nm	0.30
0.23	3.72	10.51	4.97	2.24	0.95	bdl	nm	nm	0.25
0.13	3.74	11.47	5.47	1.91	1.05	0.03	nm	nm	0.51

0.22	3.62	10.07	5.13	2.21	1.08	bdl	nm	nm	0.24
0.20	3.90	9.40	5.75	2.33	1.22	bdl	nm	nm	0.32
0.19	3.72	9.11	5.67	2.48	1.28	0.00	nm	nm	0.23
0.22	3.69	9.43	5.70	2.51	1.25	bdl	nm	nm	0.34
0.23	3.52	9.13	5.68	2.59	1.25	bdl	nm	nm	0.30
0.22	3.39	8.85	5.68	2.55	1.20	bdl	nm	nm	0.33
0.20	3.64	9.25	6.05	2.54	1.23	0.06	nm	nm	0.21
0.22	3.83	9.27	5.65	2.57	1.35	bdl	nm	nm	0.18
0.16	5.31	11.97	3.85	1.69	0.96	0.02	nm	nm	0.76
0.22	3.62	8.87	5.74	2.48	1.30	bdl	nm	nm	0.39
0.22	3.75	10.30	5.22	2.22	1.06	0.01	nm	nm	0.51
0.22	4.22	9.91	5.52	2.24	1.27	0.00	nm	nm	0.62
0.21	4.25	9.98	5.48	2.08	1.21	0.01	nm	nm	0.65
0.21	3.51	9.29	5.69	2.70	1.31	0.00	nm	nm	0.28
0.23	3.55	9.17	5.79	2.54	1.44	bdl	nm	nm	0.19
0.22	3.89	9.84	5.43	2.19	1.21	0.00	nm	nm	0.50
0.20	3.93	9.90	5.48	2.21	1.15	0.02	nm	nm	0.41
0.21	3.80	9.73	5.56	2.26	1.29	bdl	nm	nm	0.27
0.25	3.79	10.27	5.33	2.17	1.20	0.02	nm	nm	0.52
0.17	3.88	9.78	5.71	2.52	1.28	0.00	nm	nm	0.41
0.23	3.59	8.96	5.91	2.63	1.16	0.01	nm	nm	0.37
0.25	3.91	9.76	4.56	2.40	1.19	bdl	nm	nm	0.36
0.23	3.46	9.49	5.33	2.38	1.14	0.00	nm	nm	0.24
0.21	3.87	10.34	5.34	2.18	1.10	0.00	nm	nm	0.40
0.23	3.95	9.98	5.42	2.19	1.13	0.00	nm	nm	0.33
0.22	3.93	9.20	5.54	2.54	1.34	0.01	nm	nm	0.15
0.23	2.85	8.22	6.34	2.87	1.30	0.00	nm	nm	0.27
0.24	3.96	9.74	5.50	2.41	1.76	bdl	nm	nm	0.36
0.22	3.68	8.97	5.58	2.69	1.35	bdl	nm	nm	0.12
0.19	3.95	9.12	5.40	2.55	1.11	bdl	nm	nm	0.14
0.23	3.94	9.37	5.31	2.27	1.24	0.01	nm	nm	0.11
0.21	3.84	8.89	5.88	2.48	1.45	bdl	nm	nm	0.20
0.22	3.78	8.63	5.76	2.77	1.48	0.00	nm	nm	0.12
0.21	3.81	8.84	5.62	2.69	1.42	0.00	nm	nm	0.13
0.19	3.74	9.63	5.48	2.23	1.19	0.01	nm	nm	0.18
0.21	3.83	9.14	5.85	2.51	1.34	bdl	nm	nm	0.21
0.23	3.87	9.16	5.33	2.54	1.61	0.00	nm	nm	0.30
0.22	3.95	9.17	4.59	2.76	1.38	bdl	nm	nm	0.14
0.21	1.85	10.35	4.57	1.40	0.73	nm	nm	nm	bdl
0.14	3.32	9.33	5.35	2.33	1.33	nm	nm	nm	0.08
0.19	4.08	10.07	5.50	2.42	1.33	nm	nm	nm	0.05
0.21	3.76	8.68	5.67	2.69	1.44	nm	nm	nm	0.08
0.20	3.51	8.61	5.50	2.63	1.43	nm	nm	nm	0.03
0.14	1.74	10.12	5.19	1.53	0.84	nm	nm	nm	0.07
0.15	3.76	9.09	5.59	2.61	1.48	nm	nm	nm	0.10
0.13	3.29	8.59	5.24	2.38	1.44	nm	nm	nm	bdl
0.18	3.37	8.47	5.69	2.55	1.41	nm	nm	nm	0.12
0.24	3.79	8.99	5.67	2.52	1.42	nm	nm	nm	bdl

0.21	3.82	8.79	5.47	2.46	1.40	nm	nm	nm	bdl
bdl	1.92	11.53	4.38	1.15	0.78	nm	nm	nm	0.09
bdl	2.31	10.22	4.75	1.57	0.87	nm	nm	nm	0.05
0.21	3.86	9.40	5.19	2.35	1.28	nm	nm	nm	0.13
0.23	3.63	9.07	5.03	2.41	1.28	nm	nm	nm	0.07
0.25	3.89	9.54	5.40	2.38	1.22	nm	nm	nm	0.09
0.23	4.04	9.11	5.14	2.45	1.27	nm	0.15	nm	0.07
0.18	3.90	9.23	5.27	2.42	1.23	nm	0.15	nm	bdl
0.22	3.76	9.67	5.09	2.23	1.26	nm	0.15	nm	0.05
bdl	2.48	11.01	4.47	1.00	0.51	nm	0.15	nm	bdl
bdl	0.81	10.90	4.09	1.06	0.64	nm	0.15	nm	0.09
0.25	3.92	9.47	5.18	2.28	1.26	nm	nm	nm	0.05
0.20	3.97	9.21	5.47	2.29	1.21	nm	nm	nm	0.09
0.19	3.86	9.26	5.21	2.37	1.27	nm	nm	nm	bdl
0.25	3.97	9.05	5.43	2.44	1.26	nm	nm	nm	0.08
0.20	3.89	9.44	5.24	2.38	1.26	nm	nm	nm	0.12
0.24	3.59	8.63	5.20	2.66	1.38	nm	nm	nm	0.13
0.17	3.43	8.98	5.99	2.41	1.36	nm	nm	nm	0.03
0.20	2.39	9.78	5.11	1.58	1.03	nm	nm	nm	0.06
0.21	3.95	9.19	5.52	2.47	1.39	nm	nm	nm	0.10
0.31	3.46	8.62	5.59	2.70	1.48	nm	nm	nm	0.08
0.28	3.67	8.77	5.50	2.65	1.45	nm	nm	nm	0.09
bdl	3.46	8.95	5.53	2.50	1.41	nm	nm	nm	0.09
0.32	3.53	8.63	5.56	2.69	1.49	nm	nm	nm	0.07
0.18	3.61	8.95	5.34	2.60	1.46	nm	nm	nm	0.11
bdl	2.81	9.38	5.22	2.22	1.18	nm	nm	nm	0.08

Glass K2O	2.44	magma glass correcti	0.510059
MI K2O	1.37	magma MI correction	0.909091
initical xtal	10%		
initial K2O	1.245455		

F-wt_mea wt.%	Cl-wt_meas wt.%	S-ug/g_me ug/g	F-ug/g_me ug/g	Cl-ug/g_m ug/g	TOTAL_me	HOST	mineral
nan	0.07	3103	nm	719	94.83	CAN-TLP-0037-ol3	ol
nan	nan	2903	nm	bdl	95.27	CAN-TLP-0040-ol4	ol
nan	0.08	3403	nm	795	94.71	CAN-TLP-0052-ol2	ol
0.13	0.05	3204	1297	484	97.18	CAN-TLP-0042-ol3	ol
0.16	0.05	3461	1556	504	97.76	CAN-TLP-0042-ol8	ol
0.12	0.05	3505	1237	532	97.16	CAN-TLP-0042-ol8	ol
0.15	0.05	3419	1545	513	97.40	CAN-TLP-0042-ol8	ol
0.16	0.06	3784	1566	603	97.01	CAN-TLP-0042-ol12	ol
0.11	0.06	3155	1101	650	97.04	CAN-TLP-0042-ol22	ol
0.12	0.09	3464	1168	891	96.68	CAN-TLP-0042-ol29	ol
0.11	0.11	4925	1142	1076	98.04	CAN-TLP-0168-ol53	ol
0.12	0.08	2394	1163	754	98.87	CAN-TLP-0168-ol66-c	ol
0.10	0.06	2992	963	557	97.95	CAN-TLP-0168-ol67	ol
0.14	0.05	3483	1448	530	96.10	M8-A-ol35	ol
0.11	0.07	3403	1069	659	96.57	M8-A-ol41	ol
0.12	0.06	3619	1235	625	96.09	M8-A-ol45	ol
0.11	0.05	2844	1116	451	98.14	M8-A-ol62	ol
0.14	0.07	3761	1434	662	96.79	M8-A-ol69	ol
0.11	0.06	3114	1084	650	96.63	M8-A-ol69	ol
0.13	0.07	3173	1296	747	96.64	M8-A-ol69	ol
0.14	0.05	3398	1413	505	97.08	M8-A-ol75	ol
0.12	0.06	3519	1232	608	95.96	M8-A-ol76	ol
0.15	0.08	3066	1538	849	97.29	M8-A-ol90a	ol
0.14	0.07	3775	1354	716	94.01	M8-A-ol102-core	ol
0.10	0.07	3483	1048	660	96.20	M8-A-ol102-core	ol
0.10	0.06	2997	967	596	98.20	M8-A-ol109	ol
0.12	0.07	3630	1189	671	95.67	M8-C-ol4	ol
0.14	0.07	3602	1430	688	96.12	M8-C-ol7	ol
0.12	0.06	3266	1154	645	96.76	M8-C-ol13-core	ol
0.11	0.07	3258	1138	654	98.41	M8-C-ol30	ol
0.13	0.10	2551	1342	956	97.92	M8-C-ol39	ol
0.12	0.05	3309	1235	534	96.97	M8-D-ol41	ol
0.12	0.07	3375	1231	701	97.19	M8-D-ol41	ol
0.15	0.05	3528	1469	539	96.96	M8-D-ol44	ol
0.16	0.10	3250	1588	951	98.09	M8-C-ap94	ap
0.13	0.09	3131	1258	939	96.93	M8-C-ap94	ap
0.13	0.10	3091	1345	1000	97.87	M8-C-ap94	ap
0.18	0.10	831	1781	955	100.25	CAN-TLP-0042-ol1	ol
0.15	0.08	964	1473	820	99.09	CAN-TLP-0042-ol12	ol
0.15	0.09	1716	1478	924	99.12	CAN-TLP-0042-ol29	ol
0.15	0.08	1933	1486	834	99.19	CAN-TLP-0042-ol30	ol
0.15	0.08	921	1521	845	99.17	CAN-TLP-0168-ol5	ol
0.21	0.09	1202	2128	938	99.31	CAN-TLP-0168-ol8	ol
0.17	0.08	989	1694	844	100.19	CAN-TLP-0168-ol13	ol
0.15	0.13	2046	1548	1339	98.79	CAN-TLP-0168-ol50	ol

0.15	0.08	945	1513	841	99.30	CAN-TLP-0168-ol72	ol
0.15	0.10	1267	1546	986	99.21	M8-A-ol19	ol
0.15	0.09	928	1520	923	99.20	M8-A-ol19	ol
0.15	0.10	1345	1492	966	98.99	M8-A-ol47	ol
0.17	0.10	1211	1698	1011	98.83	M8-A-ol47	ol
0.17	0.10	1307	1688	1036	99.12	M8-A-ol57-core	ol
0.22	0.10	842	2187	1043	99.20	M8-A-ol62	ol
0.18	0.10	723	1835	966	99.55	M8-A-ol65	ol
0.11	0.07	3024	1133	681	96.75	M8-A-ol66-core	ol
0.19	0.10	1548	1871	970	98.95	M8-A-ol102-core	ol
0.14	0.10	2047	1434	995	98.30	M8-A-ol109	ol
0.16	0.09	2493	1579	920	98.87	M8-A-ol123	ol
0.13	0.10	2590	1329	982	98.54	M8-A-ol123	ol
0.18	0.10	1130	1814	1017	98.90	M8-C-ol7	ol
0.14	0.10	767	1433	990	98.82	M8-C-ol13-core	ol
0.14	0.09	2020	1380	911	98.07	M8-C-ol39	ol
0.14	0.09	1660	1391	928	98.23	M8-C-ol39	ol
0.15	0.10	1100	1493	962	98.27	M8-C-ol39	ol
0.17	0.10	2094	1677	979	98.11	M8-C-ol43-core	ol
0.13	0.09	1622	1324	890	98.60	M8-C-ol43-core	ol
0.19	0.10	1494	1935	1020	99.91	M8-C-ol85-core	ol
0.18	0.10	1431	1823	1023	99.92	M8-D-ol18	ol
0.16	0.10	945	1570	1002	97.80	M8-D-ol41	ol
0.15	0.09	1591	1475	900	100.08	M8-D-ol47-rim	ol
0.16	0.09	1323	1604	867	99.57	M8-D-ol71-rim	ol
0.16	0.10	584	1558	951	99.95	M8-D-ol71-rim	ol
0.20	0.12	1076	1953	1151	99.18	M8-D-ol91-core	ol
0.15	0.10	1422	1456	995	97.99	M8-C-ap94	ap
0.15	0.09	499	1490	895	99.78		
0.13	0.09	576	1269	915	99.15		
0.14	0.08	443	1414	791	98.81		
0.16	0.11	784	1632	1059	99.53		
0.17	0.09	468	1688	932	99.40		
0.16	0.10	529	1574	1041	99.33		
0.16	0.09	726	1604	936	98.35		
0.18	0.10	858	1777	1014	99.25		
0.17	0.10	1207	1728	1004	97.69		
0.17	0.10	562	1731	1021	100.01		
nm	bdl	bdl	nm	bdl	98.43		
nm	0.08	402	nm	801	98.76		
nm	0.08	253	nm	799	99.49		
nm	bdl	423	nm	bdl	98.75		
nm	0.11	169	nm	1142	97.58		
nm	bdl	343	nm	bdl	99.61		
nm	bdl	487	nm	bdl	99.14		
nm	0.07	nan	nm	650	98.36		
nm	0.13	594	nm	1301	97.64		
nm	bdl	bdl	nm	bdl	99.48		

nm	bdl	bdl	nm	bdl	98.60
nm	bdl	472	nm	bdl	100.01
nm	0.10	236	nm	1003	99.33
nm	bdl	645	nm	bdl	99.23
nm	0.10	338	nm	952	99.20
nm	0.08	444	nm	762	98.93
nm	0.11	360	nm	1108	100.34
nm	0.12	bdl	nm	1184	99.35
nm	0.09	234	nm	919	100.36
nm	bdl	bdl	nm	bdl	100.97
nm	bdl	452	nm	bdl	101.30
nm	0.08	234	nm	842	98.87
nm	bdl	446	nm	bdl	99.34
nm	0.10	bdl	nm	994	99.35
nm	0.11	403	nm	1071	99.71
nm	0.07	594	nm	689	99.79
nm	0.10	650	nm	1020	98.64
nm	0.12	169	nm	1176	99.80
nm	bdl	297	nm	bdl	99.37
nm	0.09	504	nm	871	98.43
nm	0.08	421	nm	834	100.06
nm	0.11	462	nm	1135	98.87
nm	0.07	462	nm	682	98.51
nm	bdl	357	nm	bdl	99.51
nm	0.08	567	nm	832	98.94
nm	0.08	402	nm	838	99.71

	measured	ected for K
glass ppm S	440	224.6387
MI ppm S	3290	2990.909
degassed S		2766.27
magma SO2		5981.818

SiO2_host wt.%	TiO2_host wt.%	Al2O3_hos wt.%	FeO_host wt.%	MnO_host wt.%	MgO_host wt.%	CaO_host wt.%	Na2O_hos wt.%	K2O_host wt.%	P2O5_hos wt.%
38.94	nm	0.06	17.84	0.26	41.83	0.28	nm	nm	nm
39.10	nm	0.05	17.51	0.23	41.95	0.25	nm	nm	nm
38.27	nm	bdl	20.13	0.33	39.47	0.25	nm	nm	nm
39.30	0.06	0.03	18.80	0.26	41.63	0.27	0.01	bdl	bdl
39.41	0.00	0.02	18.76	0.22	41.83	0.29	0.02	bdl	0.06
39.41	0.00	0.02	18.76	0.22	41.83	0.29	0.02	bdl	0.06
39.41	0.00	0.02	18.76	0.22	41.83	0.29	0.02	bdl	0.06
39.40	0.05	0.05	18.65	0.27	41.62	0.25	0.00	bdl	0.02
39.41	0.03	0.02	18.92	0.25	41.74	0.24	0.02	bdl	0.00
39.50	0.07	0.04	19.14	0.25	41.35	0.25	bdl	0.02	0.03
39.51	0.05	0.03	18.26	0.30	41.77	0.22	0.00	bdl	bdl
38.95	0.03	0.02	19.30	0.27	41.08	0.27	0.01	0.02	bdl
39.04	bdl	0.02	16.62	0.22	43.23	0.25	bdl	0.01	0.01
38.54	0.02	0.04	20.20	0.31	39.90	0.32	0.05	0.02	bdl
39.31	0.05	0.10	17.43	0.25	42.33	0.29	0.03	0.02	0.03
39.37	0.01	0.02	17.13	0.25	42.74	0.24	0.01	bdl	0.04
39.35	bdl	0.04	18.13	0.26	41.82	0.25	0.01	0.03	0.04
38.90	0.06	0.02	19.53	0.28	41.12	0.32	0.03	bdl	0.06
38.90	0.06	0.02	19.53	0.28	41.12	0.32	0.03	bdl	0.06
38.90	0.06	0.02	19.53	0.28	41.12	0.32	0.03	bdl	0.06
39.59	0.03	0.03	17.52	0.26	42.99	0.21	0.05	0.00	0.01
39.66	bdl	0.03	17.18	0.28	42.88	0.27	0.03	0.01	0.02
39.30	0.01	0.06	19.51	0.32	40.99	0.23	0.03	0.02	0.02
38.51	0.04	0.05	20.40	0.30	40.26	0.30	0.01	bdl	0.05
38.51	0.04	0.05	20.40	0.30	40.26	0.30	0.01	bdl	0.05
39.06	bdl	0.06	19.29	0.26	41.21	0.25	0.03	bdl	0.05
39.52	bdl	0.03	18.16	0.27	41.92	0.27	0.02	bdl	0.01
39.15	0.05	0.07	18.86	0.24	41.94	0.24	bdl	bdl	0.01
38.85	bdl	0.04	18.57	0.27	41.74	0.30	bdl	0.00	0.09
39.42	0.01	0.01	17.04	0.26	42.71	0.36	bdl	bdl	0.04
38.30	0.04	0.02	19.83	0.28	40.24	0.31	0.02	0.01	0.03
39.28	0.02	0.04	17.13	0.24	42.58	0.30	0.03	bdl	0.02
39.28	0.02	0.04	17.13	0.24	42.58	0.30	0.03	bdl	0.02
39.45	0.04	0.03	18.08	0.21	41.79	0.27	0.02	0.02	0.02
0.28	bdl	bdl	0.21	0.05	0.30	55.33	bdl	bdl	41.06
0.28	bdl	bdl	0.21	0.05	0.30	55.33	bdl	bdl	41.06
0.28	bdl	bdl	0.21	0.05	0.30	55.33	bdl	bdl	41.06
38.91	0.03	0.07	18.79	0.27	41.97	0.26	bdl	0.03	0.03
39.40	0.05	0.05	18.65	0.27	41.62	0.25	0.00	bdl	0.02
39.50	0.07	0.04	19.14	0.25	41.35	0.25	bdl	0.02	0.03
39.25	0.03	0.07	19.11	0.22	41.29	0.24	0.01	0.01	bdl
39.59	0.05	0.07	15.30	0.24	44.34	0.27	bdl	0.01	0.02
39.12	0.01	0.01	17.70	0.26	42.39	0.28	bdl	0.02	0.04
40.29	bdl	0.08	14.13	0.20	45.24	0.27	bdl	0.03	0.01
39.38	0.02	0.04	17.55	0.24	42.16	0.24	0.04	0.01	0.02

38.88	0.04	0.03	17.27	0.26	43.02	0.24	0.06	0.01	bdl
39.03	0.02	0.09	18.78	0.26	41.68	0.29	0.01	bdl	0.09
39.03	0.02	0.09	18.78	0.26	41.68	0.29	0.01	bdl	0.09
39.24	bdl	0.02	16.42	0.22	43.06	0.24	0.02	0.01	0.03
39.24	bdl	0.02	16.42	0.22	43.06	0.24	0.02	0.01	0.03
38.87	0.03	0.06	20.35	0.30	40.00	0.30	0.00	0.02	0.03
39.35	bdl	0.04	18.13	0.26	41.82	0.25	0.01	0.03	0.04
39.41	bdl	0.04	18.68	0.24	41.90	0.28	0.03	bdl	0.02
39.20	0.05	0.07	19.34	0.29	41.10	0.27	0.08	bdl	0.05
38.51	0.04	0.05	20.40	0.30	40.26	0.30	0.01	bdl	0.05
39.06	bdl	0.06	19.29	0.26	41.21	0.25	0.03	bdl	0.05
39.80	0.03	0.03	16.52	0.21	43.30	0.27	0.03	0.01	0.01
39.80	0.03	0.03	16.52	0.21	43.30	0.27	0.03	0.01	0.01
39.15	0.05	0.07	18.86	0.24	41.94	0.24	bdl	bdl	0.01
38.85	bdl	0.04	18.57	0.27	41.74	0.30	bdl	0.00	0.09
38.30	0.04	0.02	19.83	0.28	40.24	0.31	0.02	0.01	0.03
38.30	0.04	0.02	19.83	0.28	40.24	0.31	0.02	0.01	0.03
38.30	0.04	0.02	19.83	0.28	40.24	0.31	0.02	0.01	0.03
38.92	0.02	0.04	17.88	0.26	42.47	0.30	0.05	bdl	0.03
38.92	0.02	0.04	17.88	0.26	42.47	0.30	0.05	bdl	0.03
38.45	0.03	0.10	20.53	0.34	39.96	0.26	bdl	0.01	0.03
39.08	0.03	0.02	18.41	0.26	41.31	0.27	bdl	0.01	0.02
39.28	0.02	0.04	17.13	0.24	42.58	0.30	0.03	bdl	0.02
39.30	0.02	0.05	18.35	0.32	41.75	0.30	0.02	0.01	0.04
39.59	0.06	0.05	16.56	0.27	43.26	0.31	0.01	bdl	0.00
39.59	0.06	0.05	16.56	0.27	43.26	0.31	0.01	bdl	0.00
39.37	0.06	0.01	18.38	0.27	41.55	0.28	bdl	0.00	0.01
0.28	bdl	bdl	0.21	0.05	0.30	55.33	bdl	bdl	41.06

Cr2O3_ho	NiO_host	TOTAL_ho	Fo	Kd-ol-calc	target(Fe2+/Mg)liq	PEC%
wt.%	wt.%		mol.%		target Kd=0.3	
nm	0.25	99.46	80.7	0.24	0.80	1.34
nm	0.22	99.33	81.0	0.23	0.78	1.48
nm	0.00	98.44	77.8	0.29	0.95	1.81
0.02	nm	100.38	79.8	0.25	0.84	0.66
bdl	nm	100.62	79.9	0.25	0.84	2.86
bdl	nm	100.62	79.9	0.25	0.84	1.92
bdl	nm	100.62	79.9	0.25	0.84	3.04
0.01	nm	100.32	79.9	0.25	0.84	1.84
bdl	nm	100.63	79.7	0.25	0.85	0.08
0.03	nm	100.66	79.4	0.26	0.87	0.45
0.04	nm	100.19	80.3	0.25	0.82	1.08
bdl	nm	99.94	79.1	0.26	0.88	-0.10
0.01	nm	99.41	82.3	0.22	0.72	1.55
0.02	nm	99.42	77.9	0.28	0.95	-0.24
0.02	nm	99.87	81.2	0.23	0.77	1.59
0.03	nm	99.84	81.6	0.23	0.75	3.86
0.02	nm	99.96	80.4	0.24	0.81	-4.63
bdl	nm	100.32	79.0	0.27	0.89	2.54
bdl	nm	100.32	79.0	0.27	0.89	-1.99
bdl	nm	100.32	79.0	0.27	0.89	0.91
0.06	nm	100.74	81.4	0.23	0.76	1.56
0.01	nm	100.36	81.7	0.22	0.75	1.96
bdl	nm	100.48	78.9	0.27	0.89	-0.38
0.01	nm	99.95	77.9	0.28	0.95	1.76
0.01	nm	99.95	77.9	0.28	0.95	-0.78
0.01	nm	100.22	79.2	0.26	0.88	-0.39
0.01	nm	100.20	80.5	0.24	0.81	1.43
bdl	nm	100.54	79.9	0.25	0.84	4.24
0.01	nm	99.87	80.0	0.25	0.83	0.78
0.04	nm	99.91	81.7	0.22	0.75	2.78
bdl	nm	99.08	78.3	0.28	0.92	2.05
0.02	nm	99.66	81.6	0.23	0.75	3.50
0.02	nm	99.66	81.6	0.23	0.75	4.86
0.01	nm	99.93	80.5	0.24	0.81	2.28
0.01	nm	97.23	na			
0.01	nm	97.23	na			
0.01	nm	97.23	na			
0.04	nm	100.40	79.9			
0.01	nm	100.32	79.9			
0.03	nm	100.66	79.4			
bdl	nm	100.24	79.4			
0.06	nm	99.96	83.8			
0.03	nm	99.87	81.0			
0.08	nm	100.32	85.1			
0.00	nm	99.71	81.1			

0.03	nm	99.82	81.6
bdl	nm	100.25	79.8
bdl	nm	100.25	79.8
0.02	nm	99.27	82.4
0.02	nm	99.27	82.4
bdl	nm	99.96	77.8
0.02	nm	99.96	80.4
0.02	nm	100.62	80.0
0.01	nm	100.47	79.1
0.01	nm	99.95	77.9
0.01	nm	100.22	79.2
bdl	nm	100.21	82.4
bdl	nm	100.21	82.4
bdl	nm	100.54	79.9
0.01	nm	99.87	80.0
bdl	nm	99.08	78.3
bdl	nm	99.08	78.3
bdl	nm	99.08	78.3
0.03	nm	99.99	80.9
0.03	nm	99.99	80.9
bdl	nm	99.70	77.6
0.02	nm	99.42	80.0
0.02	nm	99.66	81.6
0.03	nm	100.19	80.2
0.03	nm	100.14	82.3
0.03	nm	100.14	82.3
0.01	nm	99.95	80.1
0.01	nm	97.23	na

Inclusion-PEC	SiO2_pec wt.%	TiO2_pec wt.%	Al2O3_pec wt.%	Fe2O3_pec wt.%	FeO_pec wt.%	FeOT_pec wt.%	MnO_pec wt.%
	PEC-corrected compositions						
CAN-TLP-0037-ol3-mi1-PEC	41.84	4.18	15.31	2.83	7.56	10.11	0.18
CAN-TLP-0040-ol4-mi1-PEC	43.00	4.02	15.26	2.76	7.66	10.14	0.18
CAN-TLP-0052-ol2-mi1-PEC	42.27	3.64	15.03	3.08	8.58	11.36	0.16
CAN-TLP-0042-ol3-mi1-PEC	44.09	3.80	14.93	2.94	8.10	10.74	0.17
CAN-TLP-0042-ol8-mi1-PEC	43.72	3.79	14.96	2.92	8.15	10.78	0.18
CAN-TLP-0042-ol8-mi2-PEC	43.34	3.81	15.08	2.90	7.94	10.54	0.16
CAN-TLP-0042-ol8-mi3-PEC	43.09	4.07	14.40	3.05	8.73	11.47	0.16
CAN-TLP-0042-ol12-mi1-PEC	42.18	4.47	14.48	3.05	8.34	11.08	0.17
CAN-TLP-0042-ol22-mi2-PEC	44.04	3.65	14.51	2.95	7.79	10.44	0.16
CAN-TLP-0042-o29-mi2-PEC	42.87	3.42	14.60	3.03	8.26	10.99	0.17
CAN-TLP-0168-ol53-mi2-PEC	41.48	4.00	14.68	3.13	8.51	11.33	0.17
CAN-TLP-0168-ol66-mi1-PEC	46.35	2.76	16.25	2.79	7.26	9.77	0.18
CAN-TLP-0168-ol67-mi1-PEC	44.30	3.73	14.28	2.80	7.41	9.93	0.14
M8-A-ol35-mi1-PEC	43.29	3.97	14.99	3.00	7.99	10.69	0.18
M8-A-ol41-mi1-PEC	42.52	4.16	14.28	2.93	7.88	10.52	0.15
M8-A-ol45-mi1-PEC	41.70	4.05	14.09	2.99	8.42	11.12	0.19
M8-A-ol62-mi1-PEC	44.67	3.38	15.96	2.85	7.19	9.75	0.17
M8-A-ol69-mi1-PEC	42.39	4.09	14.56	3.05	8.22	10.96	0.17
M8-A-ol69-mi2-PEC	43.43	3.68	15.30	2.87	7.00	9.59	0.14
M8-A-ol69-mi3-PEC	43.88	3.64	14.64	2.86	7.22	9.80	0.15
M8-A-ol75-mi1-PEC	42.99	4.26	15.06	2.81	7.82	10.35	0.17
M8-A-ol76-mi1-PEC	42.42	4.12	14.09	2.89	7.99	10.59	0.17
M8-A-ol90a-mi1-PEC	43.56	3.50	16.89	2.74	7.38	9.85	0.16
M8-A-ol102-mi1-PEC	40.82	3.92	14.41	3.17	8.83	11.68	0.20
M8-A-ol102-mi1-PEC	42.04	4.08	14.66	3.18	8.41	11.27	0.19
M8-A-ol109-mi1-PEC	43.57	3.39	15.69	2.90	7.65	10.26	0.15
M8-C-ol4-mi1-PEC	42.36	3.85	14.56	2.95	7.92	10.58	0.15
M8-C-ol7-mi2-PEC	41.94	4.20	14.38	3.00	8.36	11.06	0.18
M8-C-ol13-mi1-PEC	42.59	3.97	14.62	3.01	8.00	10.71	0.16
M8-C-ol30-mi1-PEC	43.52	3.56	15.48	2.80	7.52	10.03	0.16
M8-C-ol39-mi1-PEC	43.17	3.54	15.22	3.20	8.60	11.48	0.23
M8-D-ol41-mi1-PEC	42.77	4.18	14.29	2.93	8.39	11.03	0.16
M8-D-ol41-mi2-PEC	43.80	3.20	14.89	2.75	7.47	9.95	0.15
M8-D-ol44-mi1-PEC	43.31	3.69	15.42	2.75	7.32	9.79	0.15

MgO_pec wt.%	CaO_pec wt.%	Na2O_pec wt.%	K2O_pec wt.%	P2O5_pec wt.%	Cr2O3_pe wt.%	NiO_pec wt.%	H2O_pec wt.%	CO2-wt_p wt.%	SO3_pec wt.%
5.32	11.67	4.12	1.70	0.95	nm	0.003	1.28	0.22	0.31
5.50	11.21	4.18	1.29	0.98	nm	0.003	2.18	0.50	0.29
5.05	10.20	4.54	1.77	1.31	nm	0.000	1.46	0.22	0.33
5.38	11.33	4.32	1.18	0.66	0.01	nm	nm	nm	0.80
5.45	11.87	4.07	1.37	0.92	0.01	nm	nm	nm	0.84
5.31	12.05	4.04	1.32	0.90	0.00	nm	nm	nm	0.86
5.84	11.72	3.95	1.23	0.92	0.00	nm	nm	nm	0.83
5.58	11.87	4.09	1.45	0.96	0.00	nm	nm	nm	0.93
5.15	12.22	3.87	1.51	0.87	0.05	nm	nm	nm	0.79
5.36	10.66	4.19	2.00	1.83	0.00	nm	nm	nm	0.86
5.84	12.13	4.26	1.23	1.85	0.01	nm	nm	nm	1.22
4.64	10.01	5.18	2.16	0.87	0.08	nm	nm	nm	0.60
5.78	13.52	3.57	1.24	0.83	0.03	nm	nm	nm	0.74
4.74	10.73	4.47	1.54	0.92	0.00	nm	nm	nm	0.87
5.74	12.59	3.63	1.54	0.89	0.01	nm	nm	nm	0.84
6.30	12.20	3.66	1.48	0.88	0.00	nm	nm	nm	0.87
4.97	12.33	4.14	1.14	0.74	0.17	nm	nm	nm	0.74
5.19	12.47	3.92	1.47	0.96	0.00	nm	nm	nm	0.92
4.42	12.83	3.95	1.66	0.90	0.11	nm	nm	nm	0.79
4.56	13.06	3.93	1.54	0.87	0.02	nm	nm	nm	0.79
5.75	11.71	3.98	1.33	0.89	0.00	nm	nm	nm	0.84
5.98	12.15	3.51	1.54	0.91	0.02	nm	nm	nm	0.86
4.65	9.47	4.99	2.03	1.49	0.01	nm	nm	nm	0.77
5.23	10.75	4.11	1.65	0.97	0.01	nm	nm	nm	0.93
4.98	12.09	3.84	1.53	0.95	0.00	nm	nm	nm	0.88
4.90	12.84	3.66	1.45	0.83	0.88	nm	nm	nm	0.75
5.49	11.80	4.18	1.35	0.85	0.01	nm	nm	nm	0.89
5.58	12.13	3.85	1.48	0.89	0.03	nm	nm	nm	0.86
5.39	12.27	3.89	1.67	0.93	0.00	nm	nm	nm	0.81
5.65	12.78	3.93	1.68	0.88	0.03	nm	nm	nm	0.79
5.24	9.99	5.36	2.04	1.11	0.01	nm	nm	nm	0.62
6.26	11.74	3.88	1.25	0.91	0.01	nm	nm	nm	0.80
5.57	12.74	3.95	1.47	0.88	0.06	nm	nm	nm	0.80
5.08	12.70	4.06	1.18	0.91	0.02	nm	nm	nm	0.86

F-wt_pec wt.%	Cl-wt_pec wt.%	S-ug/g_pe ug/g	F-ug/g_pe ug/g	Cl-ug/g_p ug/g	TOTAL_pec
0.00	0.07	3061	nm	709	97.53
0.00	0.00	2860	nm	bdl	99.01
0.00	0.08	3341	nm	780	97.73
0.13	0.05	3183	1289	481	97.87
0.15	0.05	3362	1511	489	98.44
0.12	0.05	3437	1214	521	97.89
0.15	0.05	3315	1498	498	98.17
0.15	0.06	3715	1538	592	97.79
0.11	0.06	3152	1100	649	97.72
0.12	0.09	3449	1163	887	97.46
0.11	0.11	4872	1130	1065	98.72
0.12	0.08	2396	1164	755	99.31
0.09	0.05	2946	948	548	98.52
0.15	0.05	3491	1451	532	96.89
0.11	0.06	3348	1052	648	97.34
0.12	0.06	3479	1187	601	97.03
0.12	0.05	2976	1167	472	98.62
0.14	0.06	3665	1397	645	97.62
0.11	0.07	3176	1106	663	97.26
0.13	0.07	3145	1284	740	97.36
0.14	0.05	3345	1391	497	97.79
0.12	0.06	3450	1208	596	96.84
0.15	0.09	3078	1544	852	97.90
0.13	0.07	3708	1330	703	95.21
0.11	0.07	3511	1056	665	97.01
0.10	0.06	3009	971	598	98.83
0.12	0.07	3578	1172	662	96.56
0.14	0.07	3449	1369	659	97.09
0.11	0.06	3241	1145	640	97.51
0.11	0.06	3167	1107	636	98.96
0.13	0.09	2499	1315	937	98.56
0.12	0.05	3193	1192	515	97.75
0.12	0.07	3211	1171	667	97.91
0.14	0.05	3448	1435	527	97.66

406.0451
3302

Extended Data Table 3 - Imput parameters of the degassing model runs. All ru
of gas removed at each pressure step. See Methods for details

Model run	Degassing mode	gas fraction lost	Initial Pressure (MPa)
(1)	closed		400
(2)	closed		400
(3)	closed		400
(4)	closed		400
(5)	closed		400
(6)	open	0.1	5
(7)	open	0.3	5
(8)	open	0.5	5
(9)	open	0.7	5
(10)	open	0.9	5
(11)	closed		400

ns with the Moretti et al., (2003) model. In the open system runs, gas is separated from melt during decompres

Final pressure	Temperature	Redox	Log fO_2	SiO_2	TiO_2	Al_2O_3	$(FeO)_T$	MnO
(MPa)	(°K)	(ΔNNO)	bar	(wt%)	(wt%)	(wt%)	(wt%)	(wt%)
0.1	1423	1	-9.3	44.3	4	14.8	12	0.19
0.1	“”	1	-9.3	“”	“”	“”	“”	“”
0.1	“”	1	-9.3	“”	“”	“”	“”	“”
0.1	“”	1	-9.3	“”	“”	“”	“”	“”
0.1	“”	0.5	-9.8	“”	“”	“”	“”	“”
0.1	“”	1	-9.3	“”	“”	“”	“”	“”
0.1	“”	1	-9.3	“”	“”	“”	“”	“”
0.1	“”	1	-9.3	“”	“”	“”	“”	“”
0.1	“”	1	-9.3	“”	“”	“”	“”	“”
0.1	“”	1	-9.3	“”	“”	“”	“”	“”
0.1	“”	2	-8.3	“”	“”	“”	“”	“”

ssion, and the variable "gas fraction lost" represents the quantity (mass fraction)

MgO	CaO	Na_2O	K_2O	H_2O	CO_2	S
(wt%)	(wt%)	(wt%)	(wt%)	(wt%)	(wt%)	(wt%)
6.6	10.9	4.3	1.9	2	5	0.33
“”	“”	“”	“”	“”	2	“”
“”	“”	“”	“”	“”	1	“”
“”	“”	“”	“”	“”	0.5	“”
“”	“”	“”	“”	“”	2	“”
“”	“”	“”	“”	“”	2	“”
“”	“”	“”	“”	“”	2	“”
“”	“”	“”	“”	“”	2	“”
“”	“”	“”	“”	“”	2	“”
“”	“”	“”	“”	“”	2	“”
“”	“”	“”	“”	“”	2	“”

Parameter	Value	Error	Unit	Comment
Lava effusion rate 3/10/21	43	15	m3/s	Plank et al.
Lava density	2618	179	kg/m3	Bonadonna
Lava MER	112574	40017	kg/s	Errors adde
Plume height 3/10/21	3.4	0.5	km	From VONA
Mastin MER	22596	3323	kg/s	Mastin, H=(
Total MER	135170	51999	kg/s	Errors adde
SO2 flux 3/10/21	860	106	kg/s	PlumeTraj a
SO2 wt%	0.64%	0.26%	wt%	Calculated
S wt%	0.32%	0.13%	wt%	S mass is 32
SO2 wt%	6362	2570	ppmw	
S wt%	3181	1285	ppmw	

explosive MER	17%
effusive MER	83%

parameter	Value	error	unit	comment
Tephra density	1200	120	kg/m3	Bonadonna
lava density	2618	179	kg/m3	Bonadonna
Time averaged eruption rates				
Tephra blanket MER	4.00E+03	6.00E+02	kg/s	Bonadonna
Tephra cone MER	6.00E+03	5.00E+03	kg/s	Bonadonna
Lava MER	6.30E+04	3.20E+04	kg/s	Bonadonna
total MER	7.30E+04	3.20E+04	kg/s	Bonadonna
Integrated erupted masses for eruption				
Tephra blanket total mass	2.70E+10	4.80E+09	kg	Bonadonna
Tephra cone total mass	4.20E+10	3.40E+08	kg	Bonadonna
Lava total mass	4.78E+11	2.35E+11	kg	Bonadonna
total Mass	5.47E+11	2.39E+11	kg	Bonadonna
eruption duration	86.00		days	Bonadonna
Erupted lava volume estimate	2.08E+08	1.10E+07	m3	Plank 2023
Erupted Lava mass from Bonadonna density	5.45E+11			
peak tephra blanket and cone MER	16000		kg/s	LU1 19-24 S
3 october tephra MER	9000		kg/s	LU2 Octobe
Average plume height	3.2		m	Bonadonna
Average plume height above vent	2.1		m	Civico 2022

Percentage of MER from tephra	13.70%			
Percentage of MER from lava	86.30%			
Lava eruption rate on 3 october	30	15	m3/s	Plank 2023
Plume hight on 3rd october (VONA)	4500		m	Bonadonna
Plume hight on 3rd october (PEVOLCA)	5000		m	Bonadonna
Eruptive cone height	1071		m asl	Civico 2022
Tropomi average peak fluxes	750	kg/s		
Tropomi average average fluxes	330	kg/s		

2023 (30 with error 15 m3) and Civico et al., 2022 (60 m3/s on 27/9)
ı et al., 2022
ed in quadrature
A, Bonadonna 2022, and vent height of 1100 m
0.3035M^0.241, note Bonadonna 2022 reports 9000 kg/s, suggests half the ash was airborne
ed in quadrature
and TropOMI

by dividing total MER by SO2 flux
2 g, SO2 molecular mass is 64 g

ı 2022
ı 2022 10 samples

ı 2022
ı 2022
ı 2022
ı 2022

ı 2022
ı 2022
ı 2022
ı 2022

ı 2022

Sep
er

ı 2022
!

Melt Inclusions		
Glass K2O	2.44	
MI K2O	1.37	
initical xtal	0%	

ı 2022
ı 2022

Submarine and edfice calculation

submarine base diameter	35	km		
submarine base area	961.625	km2		
ocean floor depth	4	km		
subaerial area of la palma	708	km2	(wiki)	
average area	834.8125	km2		
volume of submarine edifice	3339.25	km3		
				density
	Subaerial volume			subaerial mass
				CO2 wt%
Height of La Palma	2.423	km		CO2 mass
Estimated average height across island	0.8	km		CO2 mass
				CO2 mass
subaerial volume	566.4	km3		CO2 moles
total volume	3905.65	km3		density
				mass
Subaerial age	1.7	Ma		CO2 wt%
eruption rate	333.1765	km3/Ma		CO2 mass
eruption rate	333176.5	m3/year		CO2 mass
				CO2 mass
				CO2 moles
predicted age of edifice	11.72247	Ma		

	magma glass correction	0.561475			glass ppm S
					MI ppm SO2
					magma SO2

2700	kg/m3
1.53E+15	kg
4.50%	
6.88E+13	kg
6.88E+16	g
68818	Tg
1.56E+15	moles

2700	kg/m3
1.05453E+16	kg
4.50%	
4.74536E+14	kg
4.74536E+17	g
474536.475	Tg
1.07849E+16	moles

measured	corrected for K
440	247.0491803
3290	
6580	

3rd october with airborne ash emissions

Known parameters							
Total SO2 flux (kg/s)	Total MER (kg/s)	Effusive MER (kg/s)	Explosive MER (kg/s)	CO2 already exsolved at branch (%)	Explosive CO2/SO2 mass ratio	Initial magma SO2 content (ppmw)	Final magma SO2 content (ppmw)
860	135500	113000	22500	100%	24	6600	250

Intermediate calculations							
Dissolved SO2 of magma going into the branch (ppmw)	SO2 which exsolves above the branch (ppmw)	Total exsolved SO2 flux entering branch (kg/s)	Exsolved SO2 flux into explosive branch (kg/s)	SO2 exsolving within explosive branch (kg/s)	Exsolved SO2 flux into effusive branch (kg/s)	SO2 flux exsolving within effusive branch (kg/s)	Total exsolved CO2 flux into branch (kg/s)
5940	5690	89.43	80.49	128.03	8.94	642.97	5560.32

Outputs						
Initial CO2 wt%	**Explosive SO2 flux (kg/s)**	**Explosive CO2/SO2 mass ratio**	**Effusive SO2 flux (kg/s)**	**Effusive CO2/SO2 mass ratio**	**Total SO2 flux (kg/s)**	**Total CO2 flux (kg/s)**
4.10%	**208.51**	**24.00**	**651.91**	**0.85**	**860.43**	**5560.32**

Time averages with air

Variables	
SO2 already exsolved at branch (%)	% gas going to explosive vent at branch
10%	90%

Known parameters				
Total SO2 flux (kg/s)	Total MER (kg/s)	Effusive MER (kg/s)	Explosive MER (kg/s)	CO2 already exsolved at branch (%)
600	83000	63000	20000	100%

Exsolved CO2 flux into explosive branch (kg/s)	Exsolved CO2 flux into effusive branch (kg/s)
5004.29	556.03

Dissolved SO2 of magma going into the branch (ppmw)	SO2 which exsolves above the branch (ppmw)	Total exsolved SO2 flux entering branch (kg/s)	Exsolved SO2 flux into explosive branch (kg/s)
6336	6086	21.91	19.72

Initial CO2 wt%	Explosive SO2 flux (kg/s)	Explosive CO2/SO2 mass ratio
4.54%	141.44	24.00

borne ash emissions (tephra*2)

Explosive CO2/SO2 mass ratio	Initial magma SO2 content (ppmw)	Final magma SO2 content (ppmw)
24	6600	250

Variables	
SO2 already exsolved at branch (%)	**% gas going to explosive vent at branch**
4%	**90%**

Intermediate calculations					
SO2 exsolving within explosive branch (kg/s)	Exsolved SO2 flux into effusive branch (kg/s)	SO2 flux exsolving within effusive branch (kg/s)	Total exsolved CO2 flux into branch (kg/s)	Exsolved CO2 flux into explosive branch (kg/s)	Exsolved CO2 flux into effusive branch (kg/s)
121.72	2.19	383.42	3771.75	3394.58	377.18

Outputs			
Effusive SO2 flux (kg/s)	**Effusive CO2/SO2 mass ratio**	**Total SO2 flux (kg/s)**	**Total CO2 flux (kg/s)**
385.61	**0.98**	**527.05**	**3771.75**

Total CO2	2.77E+10
Total CO2	27.70
Total CO2 error	13.85
Daily CO2 Tg	0.33
Daily CO2 error	0.16

kg
Tg
Tg

Tg
Tg

Response to reviewers for the paper “Exceptional CO2 emissions from erupting alkaline mafic magma in the Canary volcanic archipelago”

We thank both reviewers for their comments, which are positive, constructive and help to strengthen the scientific value of this work. We accept all of these comments and address them as detailed below.

Response to Reviewer 1, Thor Hansteen:

We are grateful to Thor Hansteen for his positive summary and constructive comments, which we address as follows.

General comment A: “In the calculations of primary volatile contents of the magmas, the assumption used seems to be that only the erupted magmas are responsible for the CO2 mass emitted into the atmosphere. Because magmas that do not erupt also contribute to the degassing, the resulting estimates of original volatile contents are biased towards too high values.”

The quantification we have made is of the volatile loading in the magma which has ascended from depth, in this case from up to 30 km depth. Hansteen is correct in highlighting that there could have been extra CO_2 in the erupting magma sourced from material which did not erupt. However the evidence we have points to a weak role for such a process. We have clarified the text to reflect this as follows:

Original line 35: “implies an initial magmatic CO_2 content of 4.5 ± 1.5 wt%.”

Revised: “implies a magmatic CO_2 content of 4.5 ± 1.5 wt%.”

Original line 44: “Quantifying the original volatile content of magmas”

Revised: “Quantifying the volatile content of magmas”

Line 53 revised to: “CO_2-rich fluid inclusions trapped at high pressures[9,10] show that a co-existing fluid phase may be present even at mantle depths if CO_2 abundances are high enough[11,12]. In low viscosity magmatic systems CO_2 bubbles are able to migrate separately or/and accumulate as foams at structural discontinuities[13], thus degassing larger magma volumes than those eventually erupted. In our present study we propose a limited impact from such differential CO_2 degassing processes, as our measurements did not reveal large evolutions in CO_2 compositions during the course of the eruption.

Note that we have included reference 10 suggested by Hansteen.

Original lines 317-320 “Therefore, an important implication of our results is that about 3.9 wt% of CO_2 was already exsolved at these seismogenic depths, in agreement with the presence of CO_2 in fluid inclusions from depths shallower than 27 km[9,37]”

Revised to: “Therefore, an important implication of our results is that about 3.9 wt% of CO_2 were already exsolved at these seismogenic depths, in agreement with observations of dense CO_2-rich fluid inclusions[9,38]. Under these conditions at least 1 wt% of H_2O may have coexisted with CO_2 in the exsolved fluid phase[42]. Thus, the basanitic magma stored at depths <27 km likely coexisted with an abundant exsolved fluid phase, which not only enhanced the explosivity of the eruption but could also increase the magma compressibility, buffering volumetric changes during depressurization as the magma was erupted[49]. We cannot exclude the possibility that pre-eruptive segregation and accumulation of this CO_2-rich gas phase in a reservoir could have contributed to the eruptive gas

emissions, thereby producing higher CO_2 contents in ascending magmas than that of the original stored magma. However, the preservation of high CO_2/SO_2 ratios in FV gas during the eruption suggests that there was not a strong differentiation of CO_2 within the feeding magma reservoir, and that therefore our quantification of magmatic CO_2 contents reflects that of the magma reservoir . ″

General Comment B: "Concerning the cumulative degassing budgets, only the estimated edifice volume of the island in question has been considered, and not intrusive rocks emplaced into the crust beneath the main edifice, which certainly also degas during crystallisation."

We added this line to line 341: "This crude calculation likely provides an underestimate as it does not take into account the CO2 contribution from intrusive magma emplacement into the crust."

Further comments from Thor Hansteen:

"The *CO_2 budgets* presented are biassed by assuming that the total amount of volatiles released were dissolved in the erupted magmas only, which is most probably wrong. You nicely demonstrate that degassing must have commenced at upper mantle levels. As only a fraction of the magmas entering the crust actually reach the surface, but still degas to variable extents, the calculated volatile budgets for the primitive magmas are most likely overestimated. I know this is hard to quantify, but still has to be considered in such a high-profile paper."

We have addressed this point above by highlighting that we focus on the CO_2 content of erupting magmas, and that the lack of evolution in CO_2/SO_2 ratios points to a lack of differentiation in the magma reservoir. We are clearer now in saying that we have measured the magmatic CO_2 content, and at the end we conclude that its likely that the magma reservoir CO_2 content is largely the same as the measured magmatic CO_2 content, new lines 318-323.

"As you mention, magmatic CO_2-dominated fluid inclusions in the Tajogaite eruption (Dayton et al. 2023) gives CO_2 oversaturation pressures at about 1 GPa or less, overlapping with the results for very similar Gran Canaria basanites (Hansteen et al., 1998; CMP). Taken at face value, this would correspond to CO2 contents considerably less than those suggested in the present manuscript for the magmas involved. How does this fit with your results?"

We revised the sentence at line 317 as shown above, the presence of fluid inclusions shows that CO_2 fluid was present, but not its quantity.

"Degassing of intrusive rocks must contribute to the CO_2 budgets of ocean island volcanoes. Total degassing budgets presented in the manuscript consider only the estimated edifice volume, and thus excludes intrusive rocks in the middle to lower crust. The CO_2 exsolved from such intrusions may be released to the hydrosphere/atmosphere by diffuse degassing. Please comment on this problem."

We address this with the added line at line 341 as shown above.

Response to Reviewer 2:

We thank reviewer 2 for their positive comments and accurate summary of the key points from our work. We fully accept the comments from reviewer 2 in their annotations and have revised the manuscript to reflect reviewer 2's comments.

Addressing the comments from reviewer 2 in the annotated manuscript:

Line 90, reviewer comment: **"In reality, there were several fissures that opened throughout the afternoon of September 19."**

We revised the initial phrase "The initial eruptive fissure evolved rapidly into a single main cone (Tajogaite) that hosted multiple linearly-aligned and closely-spaced vents[32-34]"

to: "The 85-day long Tajogaite eruption began on 19th September 2021 along a NNW-ESE fracture system ~930 m above sea level, just above urbanized areas (Figure 1). The eruption rapidly built up a main volcanic cone (Tajogaite) that hosted several linearly-aligned and closely-spaced vents34-36

Line 94, reviewer comment: **"In reality, from September 19 to September 27, a tephritic magma rich in amphibole phenocrysts and poor in olivine was emitted, after the eruptive stoppage of the On September 27, the emitted magma was basanitic, very rich in olivine."**

We revised the initial phrase to the following "The initially erupted magma, an olivine-poor evolved basanite ascending from 10-16 km depth, was progressively replaced by more primary, olivine-rich and highly oxidized basanite ascending from 27-31 km depth[9,37,38].". This is in agreement with reported petrological measurements, the reviewer is referring to the glass composition when highlighting a tephritic composition, we report the overall whole rock composition.

Line 334: reviewer comment: **"Estimating the age of the entire insular edifice of La Palma at 12 million seems a bit excessive, taking into account that the age of the oldest submarine volcanic rocks that crop out on the Island (the submarine trachytic lobe-hyaloclastitic complex of La Caldera de Taburiente) of around 3.1 Ma, (Casillas et al., 2019)"**

Our initial phrase was "Assuming the same eruption rate throughout La Palma's history implies a total age of ~12 Ma and a total CO_2 production of 475,000 Mt ($1.1x10^{16}$ moles)"

We highlight that we attempt to estimate the age of both the submarine and subaerial edifice, the height of La Palma island from the sea floor is 6.4 km, so the majority of time would have been spent building the submarine edifice. We accept that the timing between subaerial growth and submarine growth was not clear and revise the text as follows:

"If the submarine growth of La Palma volcanic island occurred at the same eruption rate as during its subaerial history, we then estimate a total build-up age of ~12 Ma and a total CO_2 production of ~475,000 Mt ($1.1x10^{16}$ moles)."

14th Sep 23

Dear Professor Burton,

Your manuscript titled "Exceptional eruptive CO2 emissions from intra-plate alkaline magmatism in the Canary volcanic archipelago" has now been seen by our reviewers, whose comments appear below. In light of their advice we are delighted to say that we are happy, in principle, to publish a suitably revised version in Communications Earth & Environment under the open access CC BY license (Creative Commons Attribution v4.0 International License).

We therefore invite you to revise your paper one last time to address the remaining concerns of our reviewers. At the same time we ask that you edit your manuscript to comply with our format requirements and to maximise the accessibility and therefore the impact of your work.

EDITORIAL REQUESTS:

Please review our specific editorial comments and requests regarding your manuscript in the attached "Editorial Requests Table".

*****Please take care to match our formatting and policy requirements. We will check revised manuscript and return manuscripts that do not comply. Such requests will lead to delays. *****

Please outline your response to each request in the right hand column. Please upload the completed table with your manuscript files as a Related Manuscript file.

If you have any questions or concerns about any of our requests, please do not hesitate to contact me.

SUBMISSION INFORMATION:

In order to accept your paper, we require the files listed at the end of the Editorial Requests Table; the list of required files is also available at https://www.nature.com/documents/commsj-file-checklist.pdf .

OPEN ACCESS:

Communications Earth & Environment is a fully open access journal. Articles are made freely accessible on publication under a CC BY license (Creative Commons Attribution 4.0 International License). This license allows maximum dissemination and re-use of open access materials and is preferred by many research funding bodies.

For further information about article processing charges, open access funding, and advice and support from Nature Research, please visit https://www.nature.com/commsenv/article-processing-charges

At acceptance, you will be provided with instructions for completing this CC BY license on behalf of

all authors. This grants us the necessary permissions to publish your paper. Additionally, you will be asked to declare that all required third party permissions have been obtained, and to provide billing information in order to pay the article-processing charge (APC).

Please use the following link to submit the above items:
[link redacted]
** This url links to your confidential home page and associated information about manuscripts you may have submitted or be reviewing for us. If you wish to forward this email to co-authors, please delete the link to your homepage first **

We hope to hear from you within two weeks; please let us know if you need more time.

Best regards,

Joe Aslin

Senior Editor,
Communications Earth & Environment
https://www.nature.com/commsenv/
Twitter: @CommsEarth

REVIEWERS' COMMENTS:

Reviewer #1 (Remarks to the Author):

Second review of the manuscript “Exceptional CO2 emissions from erupting alkaline mafic magma in the Canary volcanic archipelago” by Burton et al.

The authors have taken all my comments into account, and revised the manuscript accordingly. The conclusions reached are valid interpretations which can be accounted for through assessment the presented data. I thus recommend that the paper should be accepted for publication following accurate proofreading.
Best wishes,
Thor H. Hansteen

Reviewer #2 (Remarks to the Author):

The modifications introduced in the article have substantially improved it.
Especially those modifications that refer to the CO2 content from the magma located in the crust in the form of intrusive rocks.
However, in relation to the comments expressed by me in the first review, I believe that the modifications proposed by the authors are not sufficiently adequate.
In particular, on Line 99, I continue to propose a change in wording by:
“The magma initially erupted, until the eruptive pause on September 27, was a tephrite poor in

olivine and very rich in amphibole that rose from 10 to 16 km deep; From the eruptive pause on September 27, it changed to a more primary basanite, rich in olivine, poor in amphibole and highly oxidized, which rose from 27 to 31 km deep."
The change in composition was not progressive, but occurred after the eruption stopped on September 27. The change from tephrite to basanite was carried out in the entire composition of the rock, not only in the glass. Furthermore, not only did the proportion of olivine change, but also, and very notably, the proportion of amphibole (with the consequent indication of the change in the H2O content of the magma).
On the other hand, in relation to line 337 “If the submarine growth of the volcanic island of La Palma occurred at the same eruption rate as during its subaerial history, then we estimate a total age of accumulation of ~12 Ma and a total production of CO2 of ~475,000 Mt (1.1x1016 moles). "I recommend changing the wording to the following:
“If the submarine growth of the volcanic island of La Palma (which took place, at least since 3.1 Ma, age of the oldest submarine volcanic rocks outcropping on the Island, the submarine trachytic lobe-hyaloclastitic complex of the interior of the Caldera de Taburiente, Casillas et al., 2019) occurred at the same eruption rate as during its subaerial history, then we estimate a total age of accumulation of ~12 Ma and a total production of CO2 of ~475,000 Mt (1.1x1016 moles).
In this way, the calculated age of the Island's submarine growth can be compared with the data obtained from the oldest submarine outcropping rocks.
For all these reasons, I consider that the article deserves to be published with these slight modifications.

Response to reviewers in final revision of manuscript COMMSENV-23-0693A “Exceptional eruptive CO2 emissions from intra-plate alkaline magmatism in the Canary volcanic archipelago”

Reviewer 1: Thor Hansteen: many thanks to this reviewer for they comments, there is nothing to add

Reviewer 2’s comments are in red below with edited text in quotes and my comments in black text

However, in relation to the comments expressed by me in the first review, I believe that the modifications proposed by the authors are not sufficiently adequate.

In particular, on Line 99, I continue to propose a change in wording by:

“The magma initially erupted, until the eruptive pause on September 27, was a tephrite poor in olivine and very rich in amphibole that rose from 10 to 16 km deep; From the eruptive pause on September 27, it changed to a more primary basanite, rich in olivine, poor in amphibole and highly oxidized, which rose from 27 to 31 km deep."

The change in composition was not progressive, but occurred after the eruption stopped on September 27. The change from tephrite to basanite was carried out in the entire composition of the rock, not only in the glass. Furthermore, not only did the proportion of olivine change, but also, and very notably, the proportion of amphibole (with the consequent indication of the change in the H2O content of the magma).

We have modified the text removing the word “progressively”, so the text now reads as follows:

“The initially erupted magma, an olivine-poor evolved basanite ascending from 10-16 km depth, was replaced by more primary, olivine-rich and highly oxidized basanite ascending from 27-31 km depth9,37,38”

In this way we address the reviewers’ point by not defining the timescale for the transition in composition.

On the other hand, in relation to line 337 “If the submarine growth of the volcanic island of La Palma occurred at the same eruption rate as during its subaerial history, then we estimate a total age of accumulation of ~12 Ma and a total production of CO2 of ~475,000 Mt (1.1x1016 moles). "I recommend changing the wording to the following:

“If the submarine growth of the volcanic island of La Palma (which took place, at least since 3.1 Ma, age of the oldest submarine volcanic rocks outcropping on the Island, the submarine trachytic lobe-hyaloclastitic complex of the interior of the Caldera de Taburiente, Casillas et al., 2019) occurred at the same eruption rate as during its subaerial history, then we estimate a total age of accumulation of ~12 Ma and a total production of CO2 of ~475,000 Mt (1.1x1016 moles).

In this way, the calculated age of the Island's submarine growth can be compared with the data obtained from the oldest submarine outcropping rocks.

This suggestion is not changing anything substantial in the meaning of the current text, and the main recommendation involves adding a data point which can be found in the suggested reference Casillas 2019. This reference is not easy to find and appears to be a book chapter, unclear if peer-reviewed. We therefore do not make a change, as the result would not improve clarity or change the reported volume or timing.

https://portalciencia.ull.es/documentos/6235615973242a6be97361f0